

NATIONAL CONTRACTOR REPORT



NASA CR-

c.1

NASA CR-2009

**LOAN COPY: RETURN TO
AFWL (DOUL)
KIRTLAND AFB, N. M.**

A METHOD FOR ANALYZING DYNAMIC STALL OF HELICOPTER ROTOR BLADES

by Peter Crimi and Barry L. Reeves

Prepared by

AVCO SYSTEMS DIVISION

Wilmington, N.C.

for Language Research Center

NATIONAL AERONAUTICS AND SPACE ADMINISTRATION • WASHINGTON, D. C. • MAY 1972



A standard linear barcode is positioned vertically on the left side of the page. To its right, the text "TECH LIBRARY KAFB, NM" is printed vertically, aligned with the barcode's orientation.



0061256

1. Report No. NASA CR-2009	2. Government Accession No.	3. Recipient's Catalog No.	
4. Title and Subtitle A METHOD FOR ANALYZING DYNAMIC STALL OF HELICOPTER ROTOR BLADES		5. Report Date May 1972	
		6. Performing Organization Code	
7. Author(s) Peter Crimi and Barry L. Reeves		8. Performing Organization Report No.	
		10. Work Unit No.	
9. Performing Organization Name and Address Avco Systems Division Wilmington, Mass.		11. Contract or Grant No. NAS1-10213	
		13. Type of Report and Period Covered Contractor Report	
12. Sponsoring Agency Name and Address National Aeronautics and Space Administration Washington, D.C. 20546		14. Sponsoring Agency Code	
15. Supplementary Notes			
16. Abstract The method developed employs a model for each of the basic flow elements involved in the unsteady stall of a two-dimensional airfoil in incompressible flow. The interaction of these elements is analyzed using a digital computer. Computations of the loading during transient and sinusoidal pitching motions are in good qualitative agreement with measured loads. The method was used to confirm that large torsional response of helicopter blades detected in flight tests can be attributed to dynamic stall.			
17. Key Words (Suggested by Author(s)) Dynamic stall Unsteady boundary layer Helicopter rotor Separated flow	18. Distribution Statement UNCLASSIFIED - UNLIMITED		
19. Security Classif. (of this report) UNCLASSIFIED	20. Security Classif. (of this page) UNCLASSIFIED	21. No. of Pages 108	22. Price* \$3.00



A METHOD FOR ANALYZING DYNAMIC STALL
OF HELICOPTER ROTOR BLADES

By Peter Crimi and Barry L. Reeves
Avco Systems Division

SUMMARY

A method has been developed for analyzing the dynamic stall of helicopter rotor blades. The method employs a model for each of the basic flow elements involved in the unsteady stall of a two-dimensional airfoil in incompressible flow. The interaction of these elements is analyzed using a digital computer.

Calculations of the loading on an airfoil during transient and sinusoidal pitching motions are in good qualitative agreement with measured loads. Dynamic overshoot, or lift in excess of the maximum static value, and unstable moment variation are in clear evidence in the computed results. Quantitative differences can be attributed in part to the use of a linearized representation of the potential flow and a quasi-steady model of the viscous mixing region.

Computations were also performed of the loading and pitch response which result from unsteady stall induced by a series of discrete vortices convected past an elastically restrained airfoil. The results were used to confirm that large torsional response of helicopter blades during a maneuver which had been detected in flight tests can be attributed to dynamic stall induced by previously formed tip vortices.



INTRODUCTION

Helicopter operation at high forward speed requires that the retreating blade develop a high lift coefficient because of the diminished dynamic pressure over that part of the rotor disc. As a result, under conditions of maximum performance, the flow periodically separates from and reattaches to each blade, giving rise to severe oscillatory control loads, increased vibration levels and, at times, a torsional aeroelastic instability. Consequently, unsteady blade stall seriously limits helicopter performance (Refs. 1 and 2).

Data from wind tunnel tests of oscillating airfoils have shown that stalling under unsteady conditions differs markedly from static airfoil stall (Ref. 3). Lift coefficients 20 to 30 percent in excess of the maximum static value have been measured. Also, there is a substantial loading hysteresis accompanied by large nose-down aerodynamic moments varying in time in such a way as to extract energy from the free stream.

There have been a number of analytical studies of the problem in recent years (Refs. 4, 5 and 6). The results are of limited applicability, however, because of the use of empirical methods.

The study reported here was directed toward developing a general method for analyzing dynamic stall and applying the method in the analysis of a type of wake-induced stall detected in helicopter flight-test data. The method developed utilizes mathematical representations of each of the flow elements involved in unsteady airfoil stall. The interactions of these elements are analyzed using a digital computer. Consideration has been limited to two-dimensional, incompressible flow. However, the method has been formulated to account for arbitrary prescribed airfoil motions and airfoil section characteristics. The method is, therefore, applicable to a number of aerodynamic and aeroelastic problems involving unsteady airfoil stall, such as stall flutter of propellers, rotors and compressor blading, rotating stall in axial-flow compressors and response of aircraft to severe gusts.



SYMBOLS

A_n	coefficients in series representation of γ
a	distance aft of midchord of pitch axis in semichords
a_{mn}, b_{mn}	coefficients in linear equations for A_n 's and B_n 's
$\hat{a}_{kn}, \hat{b}_{kn}$	
B_n	coefficients in representation of σ
b	airfoil semichord, m
C	section camber distribution, m
C_l	lift coefficient, $C_l = 1/(\rho U^2 b)$
C_m	moment coefficient, $C_m = M/(2 \rho U^2 b^2)$
C_n	normal-force coefficient, $C_n = N/(\rho U^2 b)$
C_p	pressure coefficient, $C_p = 2(p - p_\infty)/(\rho U^2)$
c	airfoil chord, m
c_n	coefficient in series representation of C
H	shear layer shape factor, $H = \theta/\delta^*$
\bar{H}	vertical separation of vortices, in semichords
\dot{h}	section plunging velocity, m/s
J	shear layer parameter, $J = \theta^*/\delta^*$
K_θ	reciprocal turbulent Reynolds number, $K_\theta = \epsilon_m / u_e \theta$
k	reduced frequency, $k = \omega b/U$
k_θ	dimensionless pitch natural frequency, $k_\theta = \omega_\theta b/U$
l	lift per unit span, N/m
l_s	length of dead-air region, m
M	Mach number
m	moment per unit span about pitch axis, positive to increase θ_p

N_f	number of terms in series representations of T and C
N_w	number of wake elements
N_γ	number of coefficients in series representation of γ
N_η	number of grid points in the η -direction
N_s	number of source elements
N	force component normal to chord line per unit span, N/m
P	pressure, N/m ² or psi
\bar{P}	dimensionless pressure, $\bar{P} = P/\rho U_0^2$
q_e	magnitude of flow external to boundary layer, m/s
q_s	ratio of streamwise boundary-layer flow component to U_0
q_η	ratio of normal boundary-layer flow component to $U_0/\sqrt{Re_b}$
$Re()$	Reynolds number based on length indicated by subscript
\bar{R}	integral over shear layer,
	$\bar{R} = (2 U_0 / K_\theta H u_e) \int_0^\delta (\tau / \rho u_e^2) (\partial q_s / \partial y) dy$
r_m, \hat{r}_k	inhomogeneous terms of equations for A_n 's and B_n 's
r_o	leading-edge radius, m
\bar{s}	streamwise vortex spacing, in semichords
s	streamwise boundary-layer coordinate
s_m	m^{th} streamwise boundary-layer grid point
T	section thickness distribution, m
TM	rotor blade torsional moment, lb-in
t	time, s
\bar{t}	dimensionless time, $\bar{t} = U_0 t/b$
t_n	coefficient in series representation of T
U	instantaneous free-stream speed, m/s

U_0	reference velocity, m/s
u	flow perturbation in x-direction, m/s
u_e	flow external to viscous mixing region
u'	root-mean-square fluctuation of free-stream due to turbulence
v	flow perturbation in y-direction, m/s
w	downwash due to airfoil incidence, motions and camber, m/s
(x, y)	coordinate system with origin at midchord of mean position of airfoil
(x_1, y_1)	coordinate system with origin at leading edge of mean position of airfoil
x_o	value of x at the terminus of the vortex wake
x_{w_n}	coordinate of n^{th} vortex wake element
x_{γ_n}	coordinate of n^{th} point at which flow-tangency condition is imposed
x_{σ_i}	coordinate of i^{th} source element
\bar{x}_{σ_i}	location of midpoint of i^{th} source element
Y	ordinate of airfoil surface with respect to chordline
α	angle of attack, rad or deg
γ	bound vortex strength, m/s
γ_w	wake vortex strength, m/s
γ_{w_n}	wake vortex strength at n^{th} wake point, m/s
ΔC_p	$C_{pL} - C_{pU}$
Δp	$p_L - p_U$
Δt	increment for integration in time, s
$\Delta \theta$	half amplitude of sinusoidal pitching, rad or deg
δ	boundary layer thickness defined as distance from surface at which $U_0 q_s = 0.995 q_e$, m

δ^*	boundary layer or shear layer displacement thickness, m
$\bar{\delta}$	$\delta \sqrt{Re_b} / b$
$\bar{\delta}^*$	$\delta^* \sqrt{Re_b} / b$
ϵ	eddy viscosity, m^2/s
η	dimensionless boundary layer coordinate, ratio of distance from the surface to $b/\sqrt{Re_b}$
η_n	n^{th} normal boundary-layer grid point
θ	boundary layer or shear layer displacement thickness, m
θ_p	pitch angle, rad or deg
θ_0	mean pitch angle or pitch angle of zero restoring moment, deg
θ^*	shear layer energy thickness
Λ	pressure gradient parameter, $\Lambda = -(\delta^2 \partial p / \partial x) / (\mu q_e)$
μ	viscosity, $N \cdot s/m^2$
ν	kinematic viscosity, m^2/s
$\bar{\nu}_e$	$1 + \epsilon / \nu$
ρ	density, kg/m^3
σ	strength of source distribution representing dead-air region, m/s
σ_0	total source strength representing airfoil thickness and dead-air region, m/s
τ	shear stress, N/m^2
ϕ	perturbation velocity potential, m^2/s
ψ	rotor blade azimuth angle, measured from downwind direction, deg
ω	angular frequency of oscillation, rad/s
ω_θ	pitch natural frequency, rad/s

Subscripts:

b	point at which pressure recovery begins in viscous mixing region
d	dead-air region
L	lower surface of airfoil
lam	laminar
R	point of reattachment of turbulent shear layer
s	separation point
t	transition point
turb	turbulent
U	upper surface of airfoil
∞	free stream



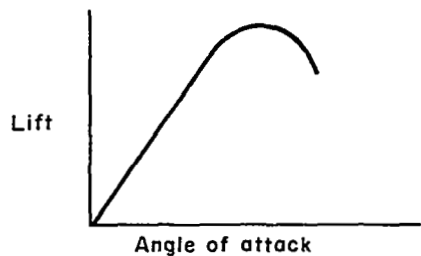
STALL MECHANISMS AND FLOW ELEMENTS

The mechanisms of stall onset are extremely complex and depend on many parameters, including Reynolds number, Mach number, leading-edge radius, thickness, camber, sweep, and the pressures imposed by unsteady motion. It is generally accepted that a given airfoil in steady flow stalls in one of three ways (Ref. 7). The three types of stall are trailing-edge stall, leading-edge stall and thin airfoil stall. Examples of each of these types are documented, with measured pressure distributions and boundary-layer profiles, and discussed in detail in Ref. 7.

Trailing-edge stall is the most easily identified of the three types, being due to the separation of the turbulent boundary layer near the trailing edge. Increasing incidence moves the point of separation progressively forward along the airfoil, resulting in a gradual decrease in lift and increase in drag, as indicated in Figure 1a. This type of stall generally occurs on relatively thick airfoils at high Reynolds numbers.

Leading-edge stall is related to the formation of a small separation bubble near the leading edge. At a fairly low incidence, laminar separation occurs near the point of minimum pressure at the leading edge. The flow reattaches a short distance downstream of the separation point because of transition from laminar to turbulent flow in the free shear layer with subsequent turbulent mixing and reattachment. As the angle of attack increases, the bubble moves closer to the leading edge, grows slightly shorter and somewhat thicker. The bubble has almost no effect on integrated loads, because it is never more than a few percent of the chord in length. At some angle of attack, the bubble bursts and the flow separates from the entire upper surface of the airfoil, resulting in a sudden loss in lift, as indicated in Figure 1b. The precise reason for the bursting of the laminar bubble has been the subject of considerable controversy. There have been correlations attempted with bubble length and with boundary-layer momentum thickness at the point of laminar separation, with little success. There is a strong indication, though, that there is some maximum amount of pressure recovery which can occur in the turbulent mixing zone and still allow reattachment, and at some incidence the required recovery exceeds this maximum, causing sudden separation. A thorough and well-ordered discussion of the various theories and evidence related to leading-edge stall is given in Ref. 8.

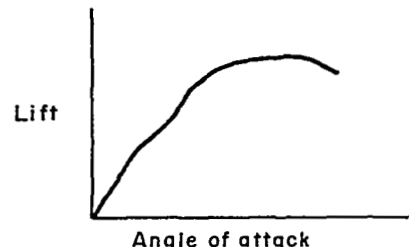
Thin-airfoil stall, which occurs at relatively low Reynolds numbers on thin airfoils, is characterized by the appearance of a laminar bubble springing from the leading edge at a relatively low incidence. Unlike the bubble formed prior to leading-edge stall, its point of separation remains fixed with increasing incidence while the bubble grows progressively larger. The processes of bubble formation and reattachment are not well understood (Ref. 8). The resulting lift curve is as sketched in Figure 1c. Because of the uncertainty as to the precise mechanism of thin-airfoil stall and its relatively infrequent occurrence, it was decided not to attempt to model the thin-airfoil stall mechanism. Elements necessary to account for both leading-edge and trailing-edge stall have been represented in the method, however.



a Trailing-edge stall



b Leading-edge stall



c Thin-airfoil stall

Figure 1 THE THREE TYPES OF AIRFOIL STALL

The primary flow elements of unsteady leading-edge or trailing-edge stall of a two-dimensional airfoil can be specifically identified, as indicated in Figure 2. When the flow is attached (Figure 2a), the flow elements are: (1) a laminar boundary layer extending from the stagnation point over the leading edge; (2) a leading-edge separation bubble (if separation occurs prior to transition); (3) a turbulent boundary layer from the reattachment point of the leading-edge bubble (or the transition point) to the trailing edge; and (4) a potential flow over the airfoil, including the effects of a vortical wake generated by the variation in time of the circulation about the airfoil. If the airfoil undergoes leading-edge stall (Figure 2b), the flow elements are: (1) a laminar boundary layer to the point of separation; (2) a laminar constant-pressure shear layer to the point of transition; (3) a turbulent constant-pressure shear layer; (4) a turbulent pressure-recovery region; and (5) a potential flow over the airfoil and external to the viscous mixing region, again including a vortical wake. If trailing-edge stall occurs (Figure 2c), the flow elements are: (1) the laminar boundary layer; (2) the leading-edge bubble (if laminar separation occurs prior to transition); (3) the turbulent boundary layer; (4) a turbulent constant-pressure shear layer; (5) a turbulent pressure-recovery region; and (6) a potential flow with vortical wake.

It was felt that, with the analytical tools at hand, a practical method could not be developed which precisely modeled each of these flow elements. Therefore, quantitative capability was sacrificed where approximations could be made while still retaining essential qualitative features of the flow. Specifically, approximations were employed in modeling the potential flow, the viscous mixing regions and the leading-edge bubble. The potential flow is derived from linearized boundary conditions. The viscous mixing regions and the leading-edge bubble are analyzed assuming quasi-steady flow. Also, interactions of the dead-air region with the inviscid flow are only indirectly taken into account. On the other hand, it could not be determined a priori what approximations would be permissible in computing the flow in the boundary layers, so a complete second-order, unsteady finite-difference method has been developed to analyze the boundary layers. The formulations used to represent the flow elements are given in the next section.

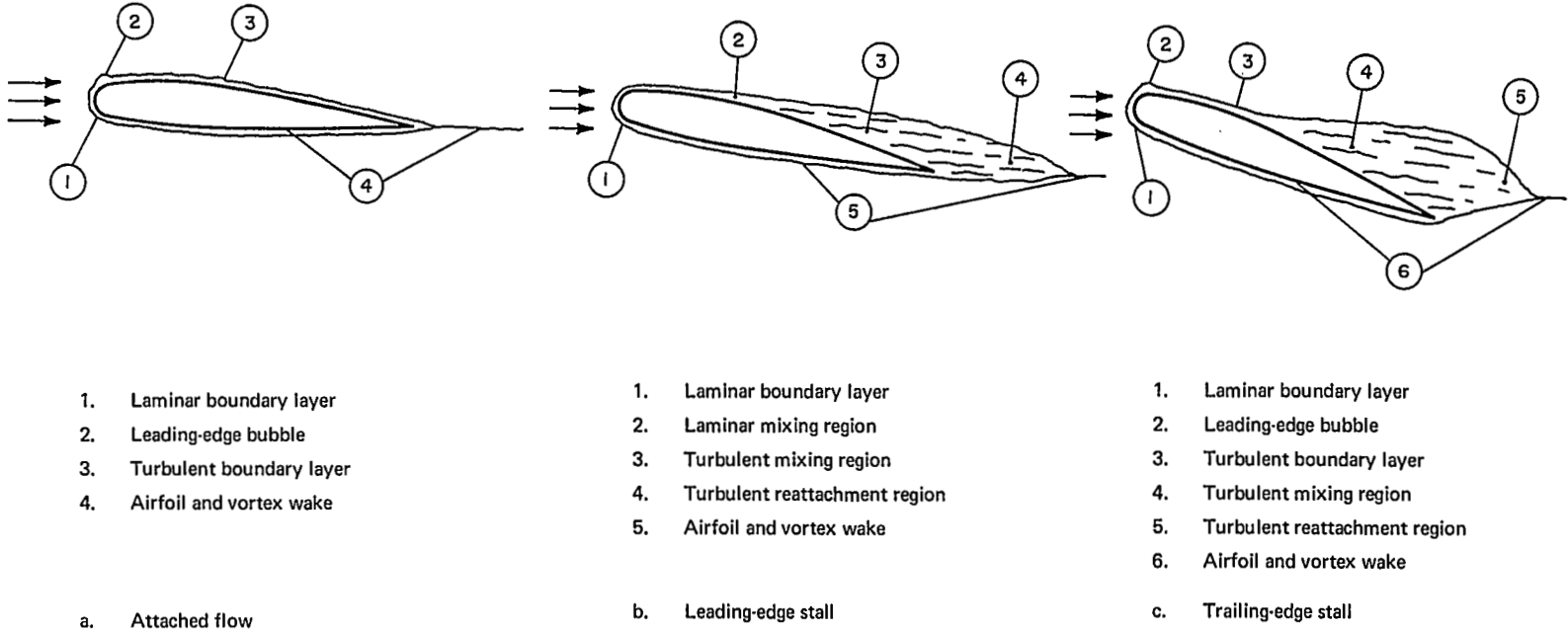


Figure 2 FLOW ELEMENTS

REPRESENTATIONS OF FLOW ELEMENTS

Potential Flow

Given the airfoil section characteristics and motions, together with the distribution of pressure in the dead-air region if the airfoil is stalled, the flow and pressure over the airfoil must be determined in order to compute the integrated load and analyze the boundary layer. The problem is formulated as follows.

Consider an airfoil of infinite span and chord $2b$ subjected to a uniform, incompressible free stream of magnitude $U(t)$, as indicated in Figure 3. Let $\theta(t)$ and $h(t)$ denote the pitch angle and plunging rate of the airfoil, as shown in Figure 3. Further, let camber and thickness distributions $C(x)$ and $T(x)$, respectively, be defined by

$$C(x) = \frac{1}{2} [Y_U(x) + Y_L(x)]$$

$$T(x) = \frac{1}{2} [Y_U(x) - Y_L(x)]$$

where Y_U and Y_L are the ordinates of the upper and lower airfoil surfaces, respectively, measured from the chord line.

Only the problem of a stalled airfoil need be considered, because the solution for attached flow is readily recovered as a special case. The coordinates of the separation and reattachment points and the prescribed pressure between those points are denoted x_s , x_R and p_d , respectively.

It is assumed at this point that perturbations to the flow caused by the airfoil are small compared to the free-stream speed, so that second-order quantities are negligible and boundary conditions can be imposed on the x -axis. This assumption, which forms the basis of classical thin-airfoil theory (Ref. 9), is clearly questionable at angles of attack sufficient to cause stall. However, the solution so obtained will still retain the essential qualitative features of the physical flow. That is, the computed pressure distribution will depend on the imposed boundary conditions, as derived from the foil motions, in approximately the same way as does the actual pressure distribution. At the same time, the solution of the linearized problem is much more readily incorporated in a large digital-computer program than would be the solution of the exact nonlinear problem.

Thus, let $u(x, y, t)$ and $v(x, y, t)$ denote components of the flow perturbation in the x and y directions, respectively, and let $p(x, y, t)$ denote the pressure. The boundary conditions which must be satisfied, for $x_R > b$, are then given by:

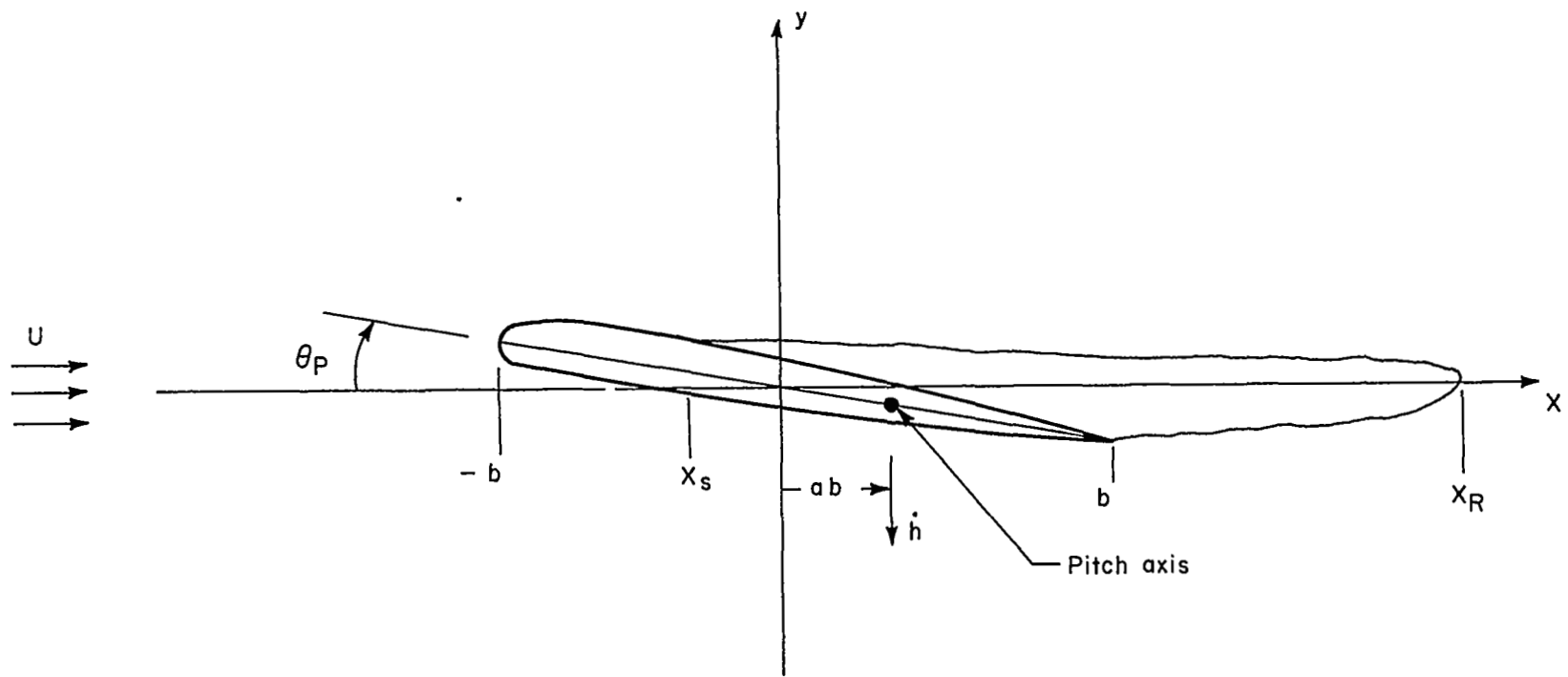


Figure 3 COORDINATE SYSTEM FOR POTENTIAL FLOW

$$v(x, 0^\pm, t) = \pm UT' - w, \quad -b \leq x \leq x_s;$$

$$v(x, 0^-, t) = -UT' - w, \quad x_s \leq x \leq b;$$

$$p(x, 0^+, t) = p_d(x, t), \quad x_s \leq x \leq b;$$

$$p(x, 0^\pm, t) = p_d(x, t), \quad b \leq x \leq x_R.$$

where

$$w = U(\theta_p - C') + h + (x - ab)\dot{\theta_p}$$

and similarly for the case with $x_R < b$.

The (+) and (-) signs affixed to the zero arguments designate the sign of y in the limit $y \rightarrow 0$. It is further required that the flow be continuous at the trailing edge (the Kutta condition) and at the separation point.

Assuming the flow is irrotational, a perturbation velocity potential ϕ can be formulated by distributing source and vortex singularities on the x -axis:

$$\phi = -\frac{1}{2\pi} \int_{-b}^{x_0} \left[\gamma(\xi, t) \tan^{-1} \left(\frac{y}{x-\xi} \right) - \sigma_0(\xi, t) \ln \sqrt{(x-\xi)^2 + y^2} \right] d\xi$$

where x_0 marks the location of the starting vortex. It is convenient to separate out thickness effects. Thus, let

$$\begin{aligned} \sigma_0(x, t) &= 2UT', \quad -b \leq x \leq x_s \\ &= 2UT' + \sigma(x, t), \quad x_s < x \leq b; \\ &= \sigma(x, t), \quad b < x \leq x_R; \\ &\equiv 0, \quad x_R < x \leq x_0. \end{aligned}$$

Also, the vortex strength for $x > b$ is known in terms of the strength on the airfoil, through conservation of circulation:

$$\gamma(b, t) = -\frac{1}{U} \frac{d}{dt} \int_{-b}^b \gamma(x, t) dx \quad (I)$$

and the vorticity downstream of the trailing edge is convected at the instantaneous free-stream speed (to first order), retaining the strength it had upon formation at the trailing edge, as prescribed by Eq. (1).

With the potential formulated in this way, the two unknown functions are the vortex strength γ on the interval $(-b, b)$ and the source strength σ over the interval (x_s, x_R) . The boundary conditions, written in terms of these two functions, are found to be (for $x_R > b$).

$$\frac{1}{\pi} \int_{-b}^b \frac{\gamma(\xi, t) d\xi}{x - \xi} = 2w - \frac{1}{\pi} \int_b^{x_0} \frac{\gamma_w(\xi, t) d\xi}{x - \xi}, \quad -b \leq x \leq x_s; \quad (2)$$

$$\sigma(x, t) + \frac{1}{\pi} \int_{-b}^b \frac{\gamma(\xi, t) d\xi}{x - \xi} = 2w - \frac{1}{\pi} \int_b^{x_0} \frac{\gamma_w(\xi, t) d\xi}{x - \xi}, \quad x_s \leq x \leq b; \quad (3)$$

$$\begin{aligned} \gamma(x, t) + \frac{1}{\pi} \int_{x_s}^{x_R} \frac{\sigma(\xi, t) d\xi}{x - \xi} &= \frac{2(p_\infty - p_d)}{\rho U} - \frac{2U}{\pi} \int_{-b}^b \frac{T'(\xi) d\xi}{x - \xi} \\ &- \frac{1}{U} \frac{\partial}{\partial t} \left\{ \int_{-b}^x \gamma(\xi, t) d\xi + \frac{1}{\pi} \int_{x_s}^{x_R} \sigma(\xi, t) \ln|x - \xi| d\xi \right. \\ &\left. + 2 \frac{U}{\pi} \int_{-b}^b T'(\xi) \ln|x - \xi| d\xi \right\}, \end{aligned} \quad (4)$$

$$x_s \leq x \leq b;$$

$$\begin{aligned}
\frac{1}{\pi} \int_{x_s}^{x_R} \frac{\sigma(\xi, t) d\xi}{x - \xi} &= \frac{2(p_\infty - p_d)}{\rho U} - \frac{2U}{\pi} \int_{-b}^b \frac{T'(\xi) d\xi}{x - \xi} \\
&- \frac{1}{U} \frac{\partial}{\partial t} \left\{ \frac{1}{\pi} \int_{x_s}^{x_R} \sigma(\xi, t) \ln|x - \xi| d\xi \right\} \\
&+ \frac{U}{\pi} \int_{-b}^b T'(\xi) \ln|x - \xi| d\xi \}, \quad b \leq x \leq x_R. \tag{5}
\end{aligned}$$

The Cauchy principal value is taken for the singular integrals. A subscript w has been affixed to γ for $x > b$ to indicate that it is known in terms of γ for $x < b$.

Equations (2) through (5) were solved by first casting γ in series form, with unknown coefficients, and taking σ (with a singular term subtracted) to vary linearly between prescribed points on the x -axis, the value of σ at each of those points being unknown. Equations (2) through (5) provided the relations needed to solve for the unknown coefficients and the values of σ .

This procedure required that the functional form of γ and σ , i.e., the locations and types of singularities, first be determined. For that purpose, an analytical solution was derived for the case of steady flow about a stalled flat plate with constant pressure in the dead-air region. The derivation is outlined in Appendix A.

The solution for steady flow, as given in Appendix A, shows, first, that if x_R is greater than b , γ has the same functional form as for attached flow, i.e., γ has a square-root singularity at the leading edge and is continuous at both $x = x_s$ and $x = b$. If x_R is less than b , however, γ has a square-root singularity on the downstream side of $x = x_R$. Furthermore, regardless of the value of x_R , σ is zero at $x = x_s$ and has a square-root singularity at $x = x_R$ (necessarily on the upstream side).

Thus, γ was taken to be of the form

$$\begin{aligned} \frac{\gamma(x, t)}{U_0} &= A_0 \sqrt{\frac{b-x/b}{b+x/b}} + \sum_{n=1}^{N_\gamma} A_n \sin n \theta \\ &+ \frac{\pi b}{4U} \left(1 + \frac{x}{b} \right) \left(1 - \frac{3x}{b} \right) \left(A_0 + \frac{A_1}{2} \right) \\ &+ A_R \left(1 + \frac{3x_R}{b} - \frac{4x}{b} \right) \sqrt{\frac{b-x}{x-x_R}} \end{aligned} \quad (6)$$

where $\cos \theta = x/b$, U_0 is a reference velocity and the coefficients A_0 through A_{N_γ} and A_R are functions of time. The term with the factor A_R is dropped if either $x_R > b$ or $x < x_R$. The factors involving x in the last two terms make Eq. (6) satisfy Eq. (1) identically, as can be verified by direct substitution.

The form of σ was defined by first dividing the interval (x_s, x_R) into N_σ segments with end points x_{σ_i} given by

$$x_{\sigma_i} = \frac{1}{2} (x_R + x_s) - \frac{1}{2} (x_R - x_s) \cos \left[\frac{(i-1)\pi}{N_\sigma} \right], \quad i = 1, 2, \dots, N_\sigma + 1;$$

whereupon

$$\begin{aligned} \frac{\sigma(x, t)}{U_0} &= B_0 \sqrt{\frac{x-x_s}{x_R-x}} + \frac{(x_{\sigma_{i+1}} - x) B_i + (x - x_{\sigma_i}) B_{i+1}}{x_{\sigma_{i+1}} - x_{\sigma_i}}, \\ x_{\sigma_i} &\leq x \leq x_{\sigma_{i+1}} \end{aligned} \quad (7)$$

$$(B_1 = B_{N_\sigma + 1} = 0)$$

where the B_i 's are unknown functions of time.

The coefficient A_R in γ , which is one of the unknowns when $x_R < b$, is in fact proportional to B_0 . If Eqs. (6) and (7) are substituted in Eq. (3) and the limit $x \rightarrow x_R$ is taken, it is found that the result can only be finite at $x = x_R$ (which it clearly must be) if

$$A_R = \left(1 - \frac{x_R}{b} \right)^{-3/2} \left(\frac{x_R - x_s}{b} \right)^{1/2} B_0$$

Thus, there are just $N_\sigma + N_\gamma + 1$ quantities to be determined at a given instant to completely define the flow and loading on the airfoil.

A set of linear algebraic equations was derived, using Eqs. (2) through (5), to provide the relations needed to solve for the unknowns. Specifically, after substituting Eqs. (6) and (7) for γ and σ , respectively, the flow-tangency boundary condition (Eqs. (2) and (3)) was imposed at points x_{γ_n} , where

$$x_{\gamma_n} = b \cos \left[\frac{(n-1)\pi}{N_\gamma} \right], \quad n = 1, 2, \dots, N_\gamma + 1;$$

and the pressure boundary condition (Eqs. (4) and (5)) was imposed at points \bar{x}_{σ_n} , where

$$\bar{x}_{\sigma_n} = \frac{1}{2} (x_{\sigma_n} + x_{\sigma_{n+1}}), \quad n = 1, 2, \dots, N_\sigma.$$

The resulting linear algebraic equations are of the form

$$\sum_{n=0}^{N_\gamma} a_{mn} A_n + \sum_{\substack{n=0 \\ n \neq 1}}^{N_\sigma} b_{mn} B_n = r_m, \quad m = 1, 2, \dots, N_\gamma + 1; \quad (8a)$$

$$\sum_{n=0}^{N_\gamma} \hat{a}_{kn} A_n + \sum_{\substack{n=0 \\ n \neq 1}}^{N_\sigma} \hat{b}_{kn} B_n = \hat{r}_k, \quad k = 1, 2, \dots, N_\sigma \quad (8b)$$

Equations (8a) were derived from Eqs. (2) and (3), and Eqs. (8b) from Eqs. (4) and (5). The expressions obtained for the coefficients and inhomogeneous terms of Eqs. (8a) and (8b) are given in Appendix B. In the development of those relations, a number of assumptions and approximations were required.

Derivatives with respect to time in Eqs. (2) through (5) were approximated by second-order finite differences. Given the value of, say, A_0 at times t , $t - \Delta t$ and $t - 2 \Delta t$, the relation

$$\dot{A}_0(t) = \frac{3 A_0(t) - 4 A_0(t - \Delta t) + A_0(t - 2 \Delta t)}{2 \Delta t} + O((\Delta t)^2)$$

was utilized, and similarly for the other required time derivatives.

Thickness and camber distributions were represented by trigonometric series so the integrals in which those functions appear could be evaluated analytically. Specifically, T and C were written in the form

$$\frac{T}{T_{\max}} = (1 - \cos \theta) \sum_{n=1}^{N_f} t_n \sin n \theta \quad (9)$$

$$\frac{C}{C_{\max}} = \sin \theta \sum_{n=1}^{N_f} c_n \sin n \theta \quad (10)$$

where $\cos \theta = x/b$ and T_{\max} and C_{\max} are the maximums of T and C, respectively. It was found that, using 24 terms, these series approximated the actual offsets of conventional NACA sections to within one percent (about .1 percent of chord) over the whole chord. The coefficients t_n and c_n are computed from

$$t_n = \frac{2}{\pi T_{\max}} \int_0^{\pi} \frac{T(\theta) \sin n \theta}{1 - \cos \theta} d\theta$$

$$c_n = \frac{2}{\pi C_{\max}} \int_0^{\pi} \frac{C(\theta) \sin n \theta}{\sin \theta} d\theta$$

The wake downwash integrals appearing on the right-hand side of Eqs. (2) and (3) were evaluated by first specifying that the value of γ_w be known at discrete points along the x-axis, with the points spaced at a distance corresponding to the time increment Δt used for integration in time. The strength at each point is obtained as follows. Numbering the wake points from 1 to N_w (N_w increases by one after each time step), with point 1 at the trailing edge and point N_w at $x = x_0$, then $\gamma_{w1}(t)$ is computed from Eq. (1), using a second-order finite-difference approximation for the time derivative, while $\gamma_{wn}(t) = \gamma_{wn-1}(t - \Delta t)$ for $n = 2, 3, \dots, N_w$. The vortex strength is assumed to vary linearly between the designated points at which γ_w is known. Note that the wake downwash integral contains a term involving unknown coefficients $A_o(t)$ and $A_1(t)$ which must be taken into account in the expressions for a_{mo} and a_{m1} .

The solution of Eqs. (8a) and (8b), which is obtained by a simple elimination scheme, provides the quantities needed to evaluate the pressure and flow at the airfoil surface. To first order, the flow at the surface is equal to $U + u$, and

$$u(x, o^{\pm}, t) = \pm \frac{\gamma(x, t)}{2} + \frac{1}{2\pi} \int_{x_s}^{x_R} \frac{\sigma(\xi, t) d\xi}{x - \xi} + \frac{U}{\pi} \int_{-b}^b \frac{T'(\xi) d\xi}{x - \xi}$$

This expression clearly cannot be used to define the flow external to the boundary layer, because γ is infinite at the leading edge. This difficulty was resolved by employing a correction factor derived by Lighthill (Ref. 10) which makes the first-order solution uniformly valid over the whole airfoil surface. Specifically, if q_e denotes the flow at the surface, defined positive in the clockwise sense as viewed in Figure 3, the Lighthill result gives, in the notation of this report,

$$q_e(x, t) = \pm \left(\frac{b+x}{b+x+r_o/2} \right)^{1/2} [U + u(x, o^{\pm}, t)] \quad (11)$$

where r_o is the leading-edge radius and the (+) and (-) signs apply to the upper and lower surfaces, respectively. Note that since r_o is of order T_{\max}^2 , q_e differs from $\pm(U+u)$ by an amount which is of second order except in the immediate vicinity of the leading edge, and that q_e is finite at the leading edge. The corresponding expression for the pressure coefficient, obtained from the linearized Bernoulli equation and Eq. (11), is

$$\begin{aligned} C_p(x, o^{\pm}, t) &= -2 \left[\pm \frac{q_e(x, t)}{U} - 1 \right] \\ &= \frac{1}{U^2} \frac{\partial}{\partial t} \left[\pm \int_{-b}^x \gamma(\xi, t) d\xi + \frac{1}{\pi} \int_{x_s}^{x_R} \sigma(\xi, t) \ln|x - \xi| d\xi \right. \\ &\quad \left. + \frac{2U}{\pi} \int_{-b}^b T'(\xi) \ln|x - \xi| d\xi \right] \end{aligned} \quad (12)$$

Explicit relations for q_e and C_p , obtained by substituting Eqs. (6), (7) and (9) in Eqs. (11) and (12), are given in Appendix B. Similar expressions for lift and moment coefficients can be developed. However, those coefficients are more readily evaluated by numerically integrating C_p , so explicit expressions were not derived.

Boundary Layer

Because the relative importance of the individual elements of the boundary-layer flow as they affect dynamic stall could not be established in advance, the representation of the boundary layer was made as general as possible to ensure that the effects of all essential elements were taken into account. The method of finite differences, rather than an integral method, was selected for the analysis of both laminar and turbulent boundary layers because accuracy and computer requirements are readily controlled and the simpler formulation allowed rapid initial check-out of computer coding. The Smith-Cebeci eddy-viscosity model (Ref. 11), which has given good results for a wide range of Reynolds numbers and various types of pressure distribution, was chosen to represent the turbulent shear.

The boundary-layer equations were cast in the following dimensionless form for the cases of both laminar and turbulent flow:

$$\frac{\partial q_s}{\partial \bar{t}} + q_s \frac{\partial q_s}{\partial s} + q_\eta \frac{\partial q_s}{\partial \eta} = - \frac{\partial \bar{p}}{\partial s} + \frac{\partial}{\partial \eta} \left(\bar{\nu}_e \frac{\partial q_s}{\partial \eta} \right) \quad (13)$$

$$\frac{\partial q_s}{\partial s} + \frac{\partial q_\eta}{\partial \eta} = 0 \quad (14)$$

Physical quantities relate to the variables in the above equations as follows. The flow component parallel to the surface is $U_0 q_s$, the flow component normal to the surface is $U_0 q_\eta / \sqrt{Re_b}$, where Re_b is Reynolds number based on semichord, time is \bar{t}/U_0 , distance along the surface is bs , distance normal to the surface is $b\eta/\sqrt{Re_b}$ and pressure is $\rho U_0^2 \bar{p}$. For laminar flow, $\bar{\nu}_e = 1$ and for turbulent flow

$$\bar{\nu}_e = 1 + \frac{\epsilon}{\nu}$$

where ν is kinematic viscosity and ϵ is eddy viscosity. In terms of the variables defined above (see Ref. 11)

$$\frac{\epsilon}{\nu} = .16 \eta^2 \sqrt{Re_b} (1 - e^{-K})^2 \left| \frac{\partial q_s}{\partial \eta} \right| \equiv \bar{\epsilon}_i, \quad \eta < \eta_o;$$

where

$$K = \frac{\eta}{26} (Re_b)^{1/4} \left[\left(\frac{\partial q_s}{\partial \eta} \right)_{\eta=0} + \frac{\eta \partial \bar{p}}{\partial s} \right]^{1/2}$$

and

$$\frac{\epsilon}{\nu} = \frac{.0168 (q_e/U_o) \bar{\delta}^*}{\sqrt{Re_b} [1 + 5.5 (\eta/\bar{\delta})^6]} \equiv \bar{\epsilon}_o, \quad \eta > \eta_o$$

where

$$\bar{\delta}^* = \int_0^\infty (1 - q_s U_o / q_e) d\eta$$

while δ is the value of η at which $q_s = .995 q_e / U_o$ and η_o is the value of η at which $\bar{\epsilon}_i = \bar{\epsilon}_o$.

The method employs variable step size in both the s and η directions. Finite-difference approximations for the derivatives appearing in Eq. (13) were derived from Taylor series. The error in each approximation is of the order of the square of the step size. The differences were formulated to allow computation of the flow at time t and streamwise coordinate s_{m+1} , given the flow at times $t - \Delta t$ and $t - 2\Delta t$ at all streamwise coordinates and the flow at streamwise coordinates s_m and s_{m-1} for time t . The finite-difference approximations used for $\partial q_s / \partial t$, $\partial q_s / \partial s$, $\partial q_s / \partial \eta$, $\partial^2 q_s / \partial \eta^2$ and $\partial \bar{p} / \partial s$ are given in Appendix C.

The solution for the flow at s_{m+1} is obtained by iteration. For the first iteration, the difference equations are linearized by employing the following approximate relations:

$$q_{s_{m+1}, n} = g_m q_{s_{mn}} - h_m q_{s_{m-1}, n}$$

$$q_{\eta_{m+1}, n} = g_m q_{\eta_{mn}} - h_m q_{\eta_{m-1}, n}$$

$$\bar{\nu}_{e_{m+1}, n} = g_m \bar{\nu}_{e_{mn}} - h_m \bar{\nu}_{e_{m-1}, n}$$

$$\begin{aligned} \left(\frac{\partial \bar{\nu}_e}{\partial \eta} \right)_{m+1, n} &= g_m [d_n \bar{\nu}_{e_{m, n+1}} + e_n \bar{\nu}_{e_{mn}} - f_n \bar{\nu}_{e_{m, n-1}}] \\ &\quad - h_m [d_n \bar{\nu}_{e_{m-1, n+1}} + e_n \bar{\nu}_{e_{m-1, n}} - f_n \bar{\nu}_{e_{m-1, n-1}}] \end{aligned}$$

where d_n , e_n and f_n are defined in Appendix C and

$$g_m = \frac{s_{m+1} - s_{m-1}}{s_m - s_{m-1}}, \quad h_m = \frac{s_{m+1} - s_m}{s_m - s_{m-1}}$$

For the second and succeeding iterations, the values computed in the previous iteration are employed in place of the above extrapolations.

Substitution of the finite-difference approximations in Eq. (13) then yields a set of linear algebraic equations of the form

$$\tilde{A}_n q_{s_{m+1}, n-1} + \tilde{B}_n q_{s_{m+1}, n} + \tilde{C}_n q_{s_{m+1}, n+1} + \tilde{D}_n q_{s_{m+1}, n+2} = \tilde{F}_n \quad (15)$$

$$n = 2, 3, \dots, N_\eta - 1$$

where the coefficients \tilde{A}_n through \tilde{D}_n and \tilde{F}_n only involve flow quantitatives computed at s_m and s_{m-1} at time t and at s_{m+1} at previous time steps. After setting $q_{s_{m+1}, 1}$ equal to zero and q_{s_{m+1}, N_η} and $q_{s_{m+1}, N_\eta + 1}$ equal to $q_{e_{m+1}}/U_o$, Eqs. (15) are readily solved by successive elimination. Equation (14) can then be used to compute q_η , from

$$q_\eta = - \int_0^\eta \left(\frac{\partial q_s}{\partial s} \right) d\eta$$

using a trapezoidal approximation.

The aforementioned iteration uses wall shear as the criterion for convergence, the allowable error being .1 percent. A maximum of five iterations is allowed at each s station. Some difficulty with convergence was encountered under extreme conditions. This problem was resolved by smoothing the eddy viscosity variation with η , as was done in Ref. 11. After $\bar{\epsilon}$ is computed, its value is replaced by the mean of the values at three adjacent points.

The grid in the η direction is computed from a geometric progression similar in form to the one used in Ref. 11. Given values of r_η and η_2 ($\eta_1 \equiv 0$), η_n is computed from

$$\eta_n = (1 + r_\eta) \eta_{n-1} - r_\eta \eta_{n-2}, \quad n = 3, 4, \dots, N_\eta + 1$$

At a given instant, the boundary layer thickness at the trailing edge can be an order of magnitude larger than at the stagnation point. To accurately compute the flow at these extremes with a single grid in the η direction would require several hundred mesh points in that coordinate. About two hundred points are needed in the s -direction for a typical airfoil. Thus, an inordinate amount of computer storage would then be required, because the

value of q_s at every mesh point for two time steps must be stored. Therefore, it was decided to make the η -scale variable. If, upon completion of the flow computation, the boundary-layer thickness $\bar{\delta}$ exceeds $\eta_{N_\eta - 2}$, η is increased by a set amount, a new, expanded η -scale is computed and the flow quantities at the new mesh points are assigned by interpolation. The variation of the interpolated quantities is smoothed by three-point averaging, and computations proceed as before. The value of η is stored with the flow quantities so the boundary-layer profile can be reconstructed when needed. It should be noted that the value of η_2 is not changed when the η -scale is expanded. This is necessary to avoid numerical instability. Using the variable η -scale, only about 75 points are needed in the η -direction.

Separation is taken to occur at the point at which the wall shear vanishes. This point must be located by extrapolation rather than interpolation, because the iteration usually fails to converge downstream of the separation point.

The computation is initiated at each instant using the Hiemenz stagnation-point profile (Ref. 12). The turbulent boundary layer downstream of reattachment of a leading-edge bubble is started from an equilibrium profile with a small but finite shear, taken from Ref. 13, matching the computed displacement thickness with that of the equilibrium profile.

In the analysis of the laminar boundary layer, the solution at each s_m is used to determine whether transition occurs, accounting for the effects of free-stream turbulence and pressure gradient. The following formula, which is a modification of a result given in Ref. 14, is used to compute transition Reynolds number $Re_{\delta_{tr}}$:

$$3.6 \left(\frac{u'}{q_e} \right)^2 Re_{\delta_{tr}}^2 + f_p(\Lambda) Re_{\delta_{tr}} - 9860 = 0 \quad (16)$$

where u' is the root-mean-square fluctuation of the free stream due to turbulence, Λ is the Karman-Pohlhausen pressure-gradient parameter, $\Lambda = -(\delta^2 \partial p / \partial x) / \mu q_e$, and $Re_{\delta_{tr}}$ is the maximum Reynolds number, based on boundary layer thickness and local external flow, for which the flow remains laminar. The function $f_p(\Lambda)$, plotted in Figure 4, was derived from data given in Ref. 12 pertaining to the effects of pressure gradient on transition, starting from the plot of Re_{δ_i} vs. Λ (Figure 17.3 of Ref. 12), where $Re_{\delta_i}^*$ is Reynolds number based on displacement thickness at the point of instability. Using the Karman-Pohlhausen integral method and the plot of $Re_{\theta_{tr}} - Re_{\theta_i}$ vs. mean pressure gradient parameter K (Figure 17.9 of Ref. 12), where $Re_{\theta_{tr}}$ and Re_{θ_i} are Reynolds numbers based on momentum thickness θ at the points of transition and instability, respectively, and K is the integral average of $-(\theta^2 \partial p / \partial x) / \mu q_e$, $Re_{\delta_{tr}}$ was computed as a function of Λ and the curve of Figure 4 was constructed. The terms of Eq. (16) which account for free-stream turbulence (i.e., Eq. (16) with $f_p = 1$) were taken directly from Ref. 14. The form of the terms was derived in Ref. 14 from arguments concerning the relation of viscous shear to transition. The

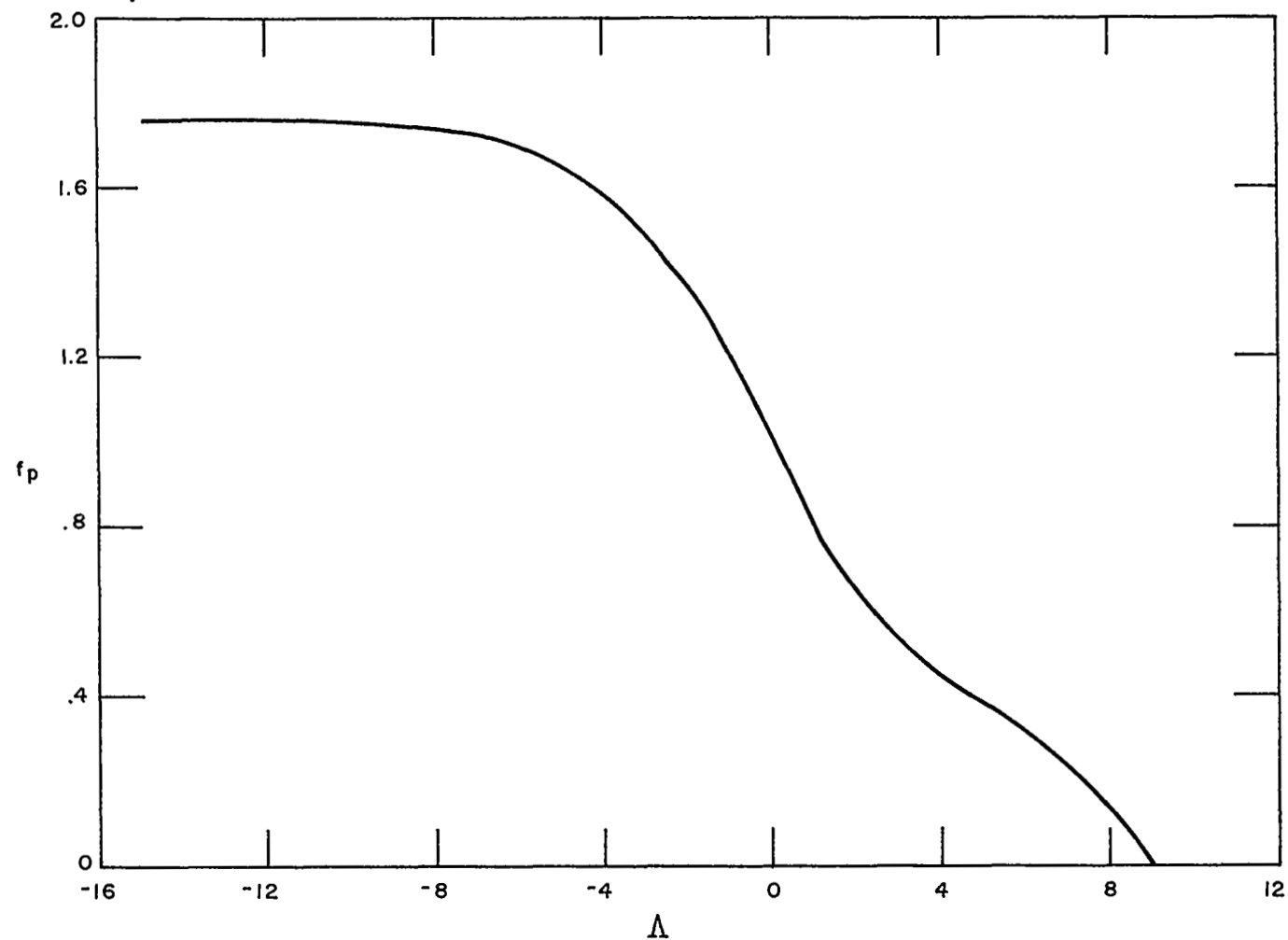


Figure 4 FUNCTION TO ACCOUNT FOR PRESSURE-GRADIENT EFFECT ON TRANSITION

relation agrees well with measured transition Reynolds number for a flat plate. Similar arguments were used in Ref. 14 to derive the effects of pressure gradient on transition. The result is an equation of the same form as Eq. (16), but with f_p simply varying linearly with Λ . It was felt that the relation so obtained was not suitable for the problem at hand, in that it did not give good correlation with experiment and does not properly reflect the stabilizing influence of a favorable pressure gradient. The term accounting for effects of pressure gradient was therefore derived by the procedure previously described.

Viscous Mixing and Reattachment Regions

For three of the commonly observed types of separated flow on airfoils, namely short (leading-edge) separation bubbles, leading edge stall (burst short bubble) and trailing edge stall experiments have demonstrated that the separated shear layer is turbulent at the point where the layer begins recompressing near reattachment. In the latter case the entire separated flow is turbulent because transition occurs upstream of the separation point. In the first two cases the shear layer is laminar for a short distance downstream of separation, but experiments seem to indicate that transition occurs over a distance which is much smaller than either the length of the constant pressure mixing region or the length of the fully turbulent reattaching shear layer. In these cases then, the assumption of a discontinuous change from laminar to turbulent flow in the shear layer seems justified. In the case of thin airfoil stall (long bubbles), on the other hand, the transition process in the shear layer appears to require a length scale which is not small compared to the bubble length. In this case reattachment may begin with the layer still in a transitional state. A meaningful flow model for reattachment of a transitional shear layer would be exceedingly difficult to construct, at least with presently available experimental data, and, therefore, thin-airfoil stall will not be considered.

Reattachment of a turbulent shear layer.— In the reattachment region in which the bubble thickness shrinks to zero and the streamwise pressure gradient is positive, the separated shear layer may reattach onto the airfoil (short bubble) or attach onto the layer shed from the lower surface at a stagnation point in the wake (leading-edge and trailing-edge stalls). In these flows it is assumed that the separated turbulent flow has a wake-like behavior and that the equilibrium wall layer usually present in attached turbulent boundary layers can be ignored. The wall shear stress is also assumed negligible compared with the properly normalized rate of change of momentum thickness of the layer and the streamwise pressure gradient. These assumptions and the analytical model which will be employed here have been used by Todisco and Reeves (Ref. 15) and Hunter and Reeves (Ref. 16) to treat supersonic separated and reattaching turbulent flows.

For negligible wall stress and zero lateral pressure gradient normal to the dividing streamline of the bubble the momentum integral and first moment of momentum equations are (Ref. 15)

$$H \frac{d\delta^*}{dx} + \delta^* \frac{dH}{dx} + (2H+1) \frac{\delta^*}{U_e} \frac{du_e}{dx} \approx 0$$

$$J \frac{d\delta^*}{dx} + \delta^* \frac{dJ}{dH} \frac{dH}{dx} + \frac{3J\delta^*}{U_e} \frac{du_e}{dx} = K_\theta H \bar{R}$$

Because $J = J(H)$, $\bar{R} = \bar{R}(H)$, $K_\theta = K_\theta(H)$ are known profile functions obtained from a one-parameter family of equilibrium or self-similar solutions the dependent variables are the velocity profile shape parameter $H = \theta/\delta^*$, displacement thickness δ^* and the local inviscid velocity at the edge of the turbulent layer u_e . For supersonic separation and reattachment a third differential equation involving these three dependent variables is obtained by coupling the integral continuity equation with the Prandtl-Meyer relationship and this third equation completes the set. In the case of subsonic separation bubbles, the interaction of the separated flow with the outer inviscid stream is much more complicated because of the absence of a local relationship between turning angle and pressure. In general, a complicated solution procedure is required in which the entire bubble shape must be iterated upon until the mixing rate in the shear layer and the subsequent rate of pressure rise at reattachment are compatible with the induced inviscid flow over the bubble. Such a point by point matching is beyond the scope of this study. Instead, approximate relationships between certain quantities appearing in the integral equations are obtained from the well developed theory of supersonic interactions, and the matching is performed in terms of only a few parameters.

The momentum integral and first moment can be rearranged and combined to give the following explicit relations for the derivatives of displacement thickness and inviscid velocity

$$d(\ln \delta^*) = \left[\frac{-3J + (2H+1)dJ/dH}{J(H-1)} \right] dH - \frac{(2H+1)K_\theta H \bar{R}}{J(H-1)} \frac{dx}{\delta^*}$$

$$d(\ln u_e) = - \left[\frac{H \frac{dJ}{dH} - J}{J(H-1)} \right] dH + \frac{K_\theta H^2 \bar{R}}{J(H-1)} \frac{dx}{\delta^*}$$

These equations are solved using the method of successive approximations. By first assuming that reattachment occurs over a sufficiently short streamwise distance (compared with the local displacement thickness), so the second term on the RHS of the first of these equations is negligible, one obtains

$$\delta^* / \delta_{b^*} = \exp \int_{H_b}^H f(H) dH$$

where

$$f(H) = \frac{-3J + (2H + 1) dJ/dH}{J(H-1)}$$

and subscript b denotes conditions at the beginning of the reattachment pressure rise. Substituting this first approximation for δ^* into the differential equations for δ^* and u_e and integrating gives

$$\ln(\delta^* / \delta_{b^*}) = \int_{H_b}^H f(H) dH - \exp \left[\int_{H_b}^{H_R} f(H) dH \right] \int_{H_b}^H \frac{(2H+1) K_\theta H \bar{R}}{J(H-1) \exp \int_{H_b}^H f(H') dH'} \frac{d \left(\frac{x - x_R}{\delta_{R^*}} \right)}{\frac{d(H/H_R)}{H_R}} \quad (17)$$

and

$$\begin{aligned} \ln(u_e / u_{eb}) = & - \int_{H_b}^H \left[\frac{H dJ/dH - J}{J(H-1)} \right] dH \\ & + \exp \left[\int_{H_b}^{H_R} f(H) dH \right] \int_{H_b}^H \frac{K_\theta H^2 \bar{R}}{J(H-1) \exp \int_{H_b}^H f(H') dH'} \frac{d \left(\frac{x - x_R}{\delta_{R^*}} \right)}{\frac{d(H/H_R)}{H_R}} \frac{dH}{H_R} \end{aligned} \quad (18)$$

where subscript R denotes conditions at the reattachment point (or wake stagnation point if bubble closure occurs in the wake). It is now assumed that the streamwise rate of change of the turbulent shear layer velocity profile (or rather the inverse, $d(x/\delta_{R^*})/dH$) is a universal function for all incompressible turbulent reattachment processes. This function was evaluated from several solutions of supersonic reattaching shear layers with the results shown in Figure 5. The variables x and δ_i^* are the "stretched" values after having been transformed by a modified Stewartson compressibility transformation. Three curves for $(x - x_R)/\delta_{i,R}^*$ versus H/H_R for Mach numbers varying between 1.3 and 2.2 are given and it is evident that the curves collapse into a single curve as the Mach number is reduced. Thus, it is assumed that the curve shown for $M_e = 1.3$ defines the streamwise rate of change of the profile shape in all turbulent reattachment processes. Values of the derivative $d(x/\delta_{R^*})/d(H/H_R)$ obtained from this curve and values of the profile function obtained from equilibrium turbulent boundary layer solutions are given in Table I.

TABLE I
PROFILE FUNCTIONS FOR TURBULENT SEPARATED FLOWS^a

H/H_R	$d\left(\frac{x-x_R}{\delta_{R^*}}\right)/d\left(\frac{H}{H_R}\right)$	J/J_R	$d\left(\frac{J}{J_S}\right)/d\left(\frac{H}{H_S}\right)$	\bar{R}/R_R	$\left(\frac{\bar{R}_H}{\bar{R}_R H_R}\right)$
0	--	0	--	--	0
.1	83	.18	1.08	2.98	.298
.2	46	.28	.95	2.53	.506
.3	33	.37	.91	2.23	.669
.4	26	.46	.90	1.98	.792
.5	22	.54	.90	1.78	.890
.6	20	.62	.91	1.60	.960
.7	20	.70	.93	1.45	1.015
.8	20	.79	.96	1.30	1.04
.9	21	.89	1.00	1.15	1.035
1.0	23	1.0	1.04	1.00	1.00
1.1	25	1.12	1.11	.86	.946
1.2	29	1.24	1.18	.72	.864

^aNOTE: $H_R = H_S = .429$, $J_R = J_S = .654$, $R_R = .463$, and $K_\theta = .05 - .0132(H/H_R)$. Also, it is convenient to use the product $\bar{R}H$ as $H \rightarrow 0$ rather than \bar{R} because in this limit $\bar{R} \rightarrow \infty$ but $\bar{R}H \rightarrow 0$.

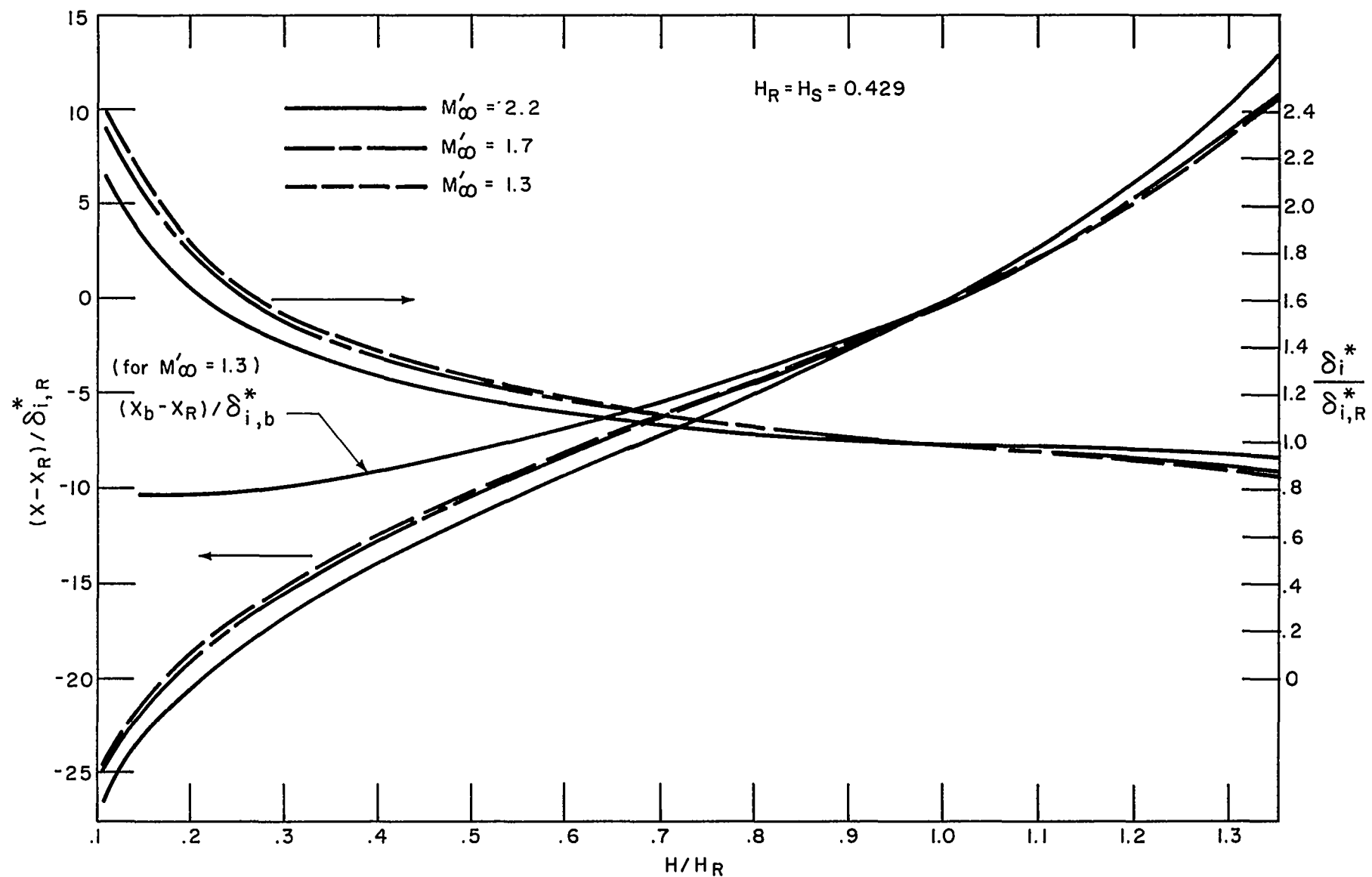


Figure 5 CORRELATIONS FOR TURBULENT REATTACHMENT

Figure 5 also shows the variation of $(x_b - x_R) / \delta_b^*$, b with H/H_R , that is, the reattachment length normalized by displacement thickness at the beginning of reattachment (only the curve for $M = 1.3$ is shown). This curve can be represented quite well by the parabola:

$$(x_R - x_b) / \delta_b^* = 10.5 [1 - (H_b / H_R)^2] \quad (19)$$

Because H_b and δ_b^* are determined by the solution of the constant pressure mixing region this relationship can be used to find the length of the reattachment region without having to first compute the velocity and displacement thickness distributions through the reattachment region.

The turbulent mixing region. — For the region between separation and the beginning of reattachment in the case of trailing-edge stall, and for the region between transition and the beginning of reattachment in the case of leading-edge stall, it is assumed that the pressure is constant and that the momentum integral and first moment equations reduce to the following:

$$H \frac{d\delta^*}{dx} + \delta^* \frac{dH}{dx} = 0$$

$$J \frac{d\delta^*}{dx} + \delta^* \frac{dJ}{dx} = K_\theta H \bar{R}$$

Now, let the subscript t denote conditions at the transition point in the shear layer. If the layer is turbulent at the separation point then $H_t = H_s$, $\delta_t^* = \delta_s^*$, etc.

The solution of the first of these equations is

$$\delta^* H = \delta_t^* H_t = \text{constant}$$

and substitution of the first equation into the second gives

$$\frac{\delta_t^* H_t}{H} \left\{ \frac{dJ}{dH} - \frac{J}{H} \right\} \frac{dH}{dx} = K_\theta H \bar{R}$$

Rearranging this expression and integrating from the transition point (or separation point for trailing-edge stall) to the beginning of reattachment gives

$$\frac{x_b - x_t}{\delta_t^*} = J_s \frac{H_t}{H_s} \int_{H_t/H_s}^{H_b/H_s} \frac{1}{K_\theta \bar{R} H(H/H_s)} \left[\frac{d(J/J_s)}{d(H/H_s)} - \frac{(J/J_s)}{(H/H_s)} \right] d\left(\frac{H}{H_s}\right) \quad (20)$$

and from the solution $\delta^* H = \text{constant}$

$$\frac{\delta_b^*}{\delta_t^*} = \frac{(H_t/H_s)}{(H_b/H_s)}$$

At the transition point we assume that the velocity along the dividing streamline of the separation bubble and the momentum thickness are continuous so that*

$$(\theta_t)_{\text{lam}} = (\theta_t)_{\text{turb}}$$

and

$$\left(\frac{H_t}{H_s} \right)_{\text{lam}} = \left(\frac{H_t}{H_s} \right)_{\text{turb}}$$

Consequently, since $H \equiv \theta / \delta^*$

$$(\delta_t^*)_{\text{turb}} = (\delta_t^*)_{\text{lam}} (H_s)_{\text{lam}} / (H_s)_{\text{turb}} = .58 (\delta_t^*)_{\text{lam}}$$

Because $x_t, (H_t/H_s)_{\text{lam}}$ and $(\delta_t^*)_{\text{lam}}$ are known from the solution of the laminar shear layer, the above expressions are sufficient to determine the length of turbulent mixing region and the displacement thickness at the beginning of reattachment in terms of the unknown profile shape parameter H_b at this point.

The laminar mixing region. — For the laminar shear layer extending from the separation point to the transition "point" inside the separation bubble the momentum integral and first moment equations are (for zero pressure gradient)

$$H \frac{d\delta^*}{dx} + \delta^* \frac{dH}{dx} = \left(\frac{\nu}{u_e \delta^*} \right) P$$

$$J \frac{d\delta^*}{dx} + \delta^* \frac{dJ}{dx} = \left(\frac{\nu}{u_e \delta^*} \right) R$$

$$\text{where } P = \frac{\delta^*}{U_e} \left(\frac{\partial u}{\partial y} \right)_{y=0}, \quad R = \frac{2\delta^*}{U_e^2} \int_0^\delta \left(\frac{\partial u}{\partial y} \right)^2 dy$$

Solution of this pair of equations has been given in Ref. 17. The solution presented in that paper was for the variation of the displacement thickness and dividing streamline velocity as functions of the non-dimensional length scale downstream of separation $x^2/\theta_s^2 R_{ex}$. Since at a laminar separation point $H_s = \theta_s/\delta_s^* = .25$ the above length scale can be cast into the form

* This procedure for finding the turbulent momentum thickness, displacement thickness and profile shape downstream of transition is analogous to the method used by Truckenbrodt for attached boundary layers (Ref. 12).

$$Re_x / (Re_{\delta_s^*})^2 = .062 x^2 / \theta_s^2 Re_x$$

Also, H/H_s is a function of u^* (the ratio of the velocity along the dividing streamline to u_e), so that the solution given in Ref. 17 can be used here with only slight modification. The variation of H/H_s and δ^*/δ_s^* with distance downstream of separation is shown in Figure 6. Here x is the distance downstream of the separation point.

Tentatively, we assume that the length of the laminar shear layer is determined by Von Doenhoff's criterion, namely that $(Re_x)_t = 50\,000$.* Thus, $(H_t/H_s)_{\text{lam.}}$ and $(\delta_t^*/\delta_s^*)_{\text{lam.}}$ are known functions of $Re_{\delta_s^*}$, as indicated in Figure 6. The characteristic velocity in each of these Reynolds numbers is the local inviscid velocity at the separation point.

Pressure calculation procedure. — For this part of the analysis, the location of the separation and reattachment points and the pressure at reattachment are specified, and it is required to compute the distribution of pressure between x_s and x_R . The basic problem is to determine H_b and x_b . With H_b known, the rise in pressure from x_b to x_R can be computed directly from Eq. (18). Since the pressure at x_R is specified and the pressure is constant from x_s to x_b , the pressure distribution is then completely determined.

The two relations used to determine x_b and H_b are Eqs. (19) and (20). Equation (20) relates $x_b - x_t$ (or $x_b - x_s$, in the case of trailing-edge stall) to H_b , while Eq. (19) relates $x_R - x_b$ to H_b . A simple iterative calculation is performed whereby successive values of H_b are assumed and x_b is computed from Eqs. (19) and (20). A solution is obtained when the two results for x_b agree within a prescribed amount.

Leading-Edge Bubble

In the analysis of the leading-edge bubble, it is assumed that the beginning of the reattachment region and the point of transition are coincident. The formulations of the viscous mixing and reattachment regions can then be employed, as follows.

From the curves of Figure 6, the conditions at transition, and hence at x_b , can be obtained, given δ^* and θ at separation from the boundary-layer analysis. Since x_b , which is assumed equal to x_t , is known from Von Doenhoff's criterion ($(x_t - x_s) q_e / \nu = 50\,000$), x_R can be computed directly from Eq. (19).

* Gault (Ref. 18) has performed a large number of experiments in which $(Re_x)_t$ ranged between 25 000 and 75 000 for over 80 percent of the data. Consequently, as Gault points out, a unique value for this transition Reynolds number is only a rough approximation and is influenced by the turbulence level, pressure gradient, etc.

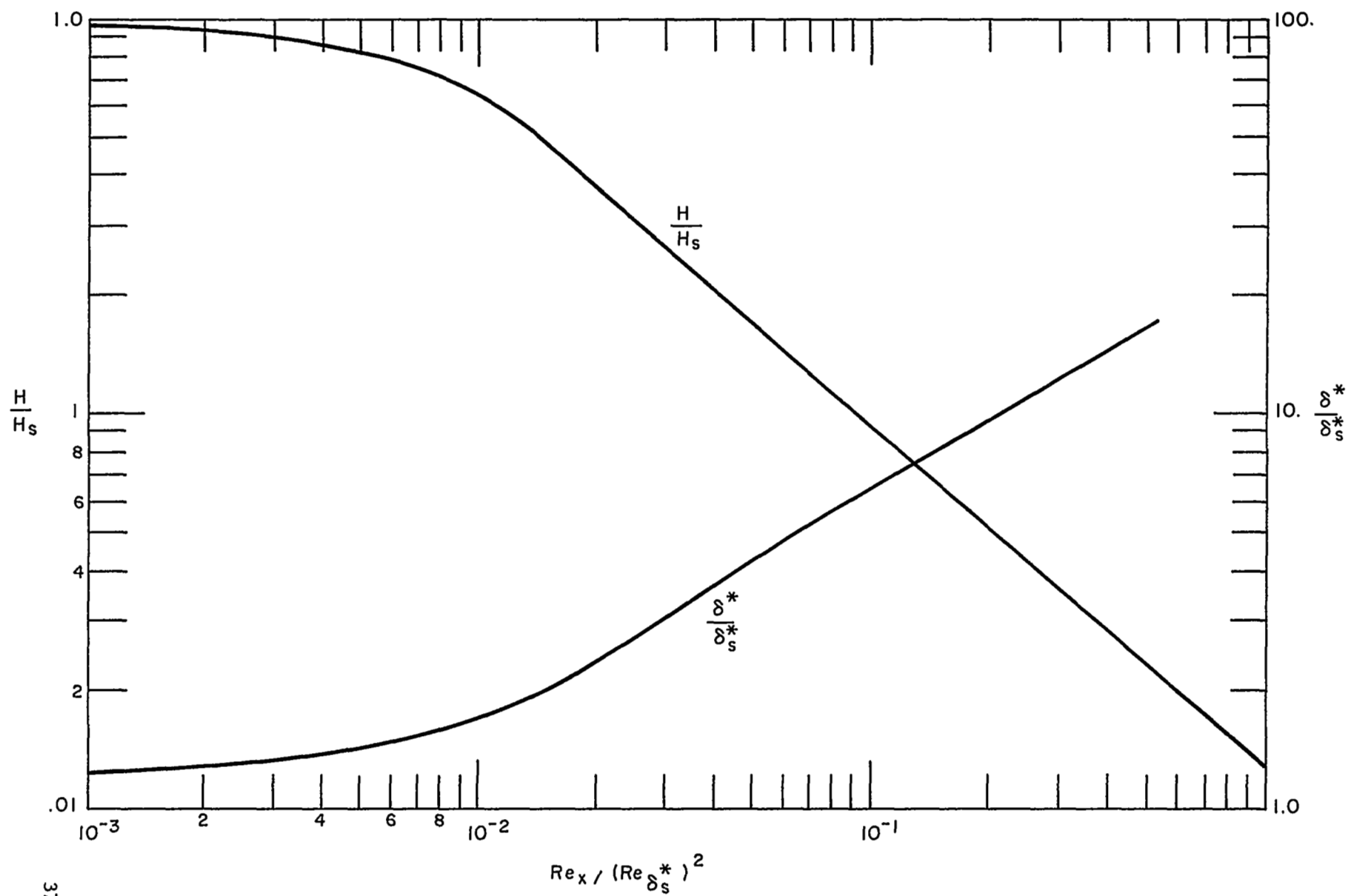


Figure 6 H AND δ^* VARIATIONS DOWNSTREAM OF SEPARATION FOR A LAMINAR SHEAR LAYER

Also, the pressure rise possible in the reattachment region can be obtained from Eq. (18).

It is assumed that the pressure rise across the bubble, from x_s to x_R , is not affected by the presence of the bubble. Given x_s and x_R , the potential-flow solution is then used to compute that increase in pressure. If the pressure rise computed from Eq. (18) exceeds the required pressure rise computed from the potential-flow solution, it is assumed that the mixing process accommodates to the lower required pressure rise and that the flow reattaches. If the required pressure rise exceeds the pressure rise computed from Eq. (18), it is assumed the leading-edge bubble has burst and the airfoil is undergoing leading-edge stall.

COMPUTATION PROCEDURE

The procedure used in analyzing the interactions of the flow elements is indicated schematically in Figure 7. The computations are carried out by forward integration in time, starting from steady, attached flow. At each time step, when the flow is attached, prescribed airfoil motions are used to derive the potential flow. The flow external to the boundary layer is then computed. The boundary layer and leading-edge bubble are then analyzed to determine whether the leading-edge bubble has burst (leading-edge stall) or the turbulent boundary layer has separated (trailing-edge stall). If the flow remains attached, time is incremented, the foil motions are again prescribed and the procedure repeated.

If the airfoil stalls, the location of the separation point is assumed, the point of reattachment and pressure at reattachment are computed by a method to be described subsequently, the pressure in the dead-air region is computed and the potential-flow solution is derived from the prescribed airfoil motions and dead-air pressure distribution. The boundary layer is then analyzed and the computed separation point location is compared with the assumed location. If the assumed location differs by more than a prescribed amount from the computed one, a new estimate of the separation point location is made and the potential flow and boundary layer are again analyzed. When the assumed and computed separation point locations are in satisfactory agreement or when four iterations have been performed, time is incremented.

The length of the dead-air region when the airfoil is stalled is computed by deriving a bubble growth rate from the potential solution and integrating in time. The growth rate is computed as follows. The rate of increase of mass of the dead-air region is given, to first order, by

$$\dot{m} = \rho \int_{x_s}^{x_R} \sigma dx$$

The total mass of the dead-air region is roughly proportional to $\rho l_s \bar{Y}_{\max}$, where $l_s = x_R - x_s$ and \bar{Y}_{\max} is the maximum of $\bar{Y}(x)$,

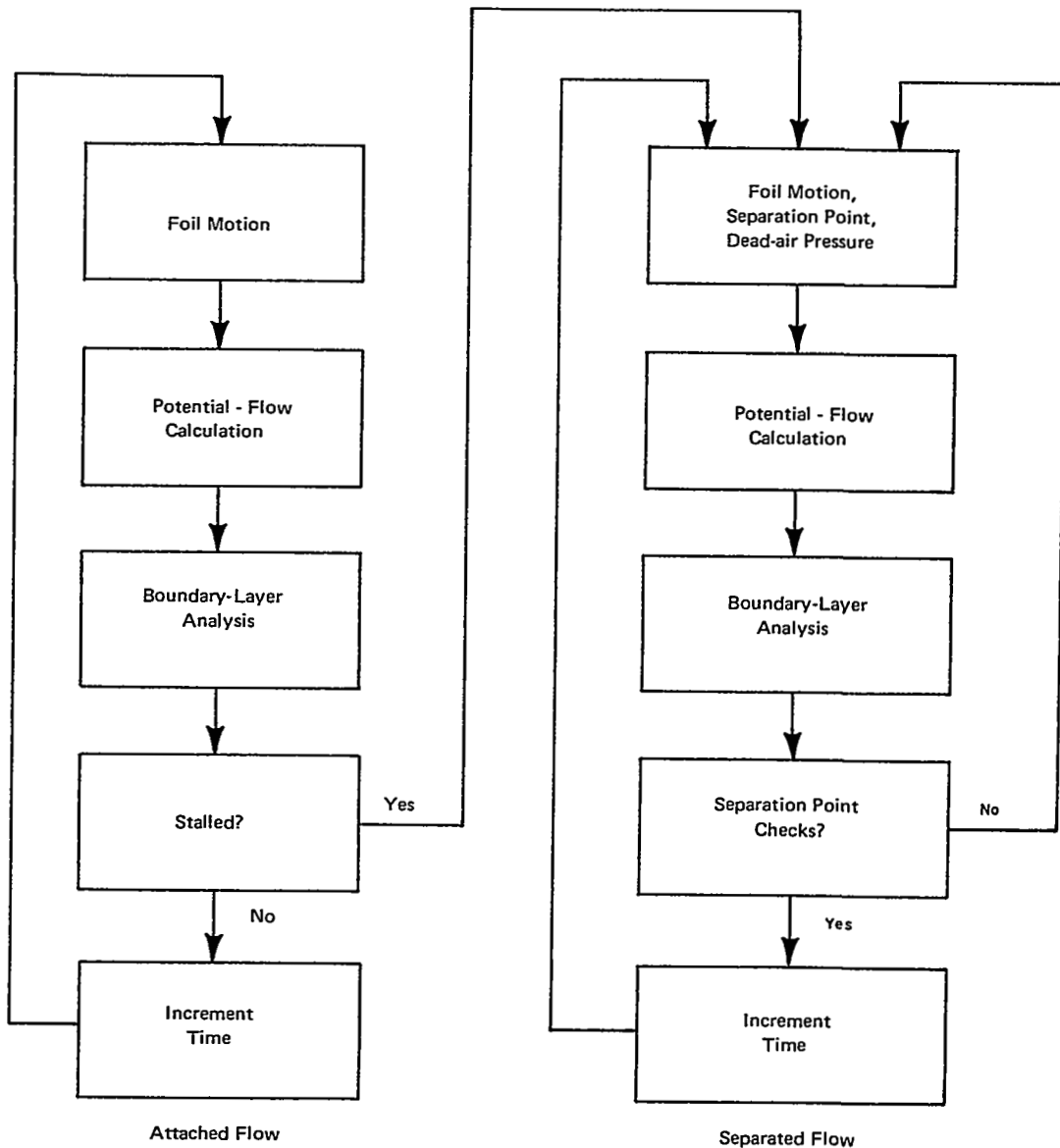


Figure 7 COMPUTATION PROCEDURE

$$\bar{Y}(x) = \int_0^x \frac{v_\sigma(\xi) d\xi}{U}$$

$$= \int_0^x \frac{\sigma(\xi) d\xi}{U}$$

If added mass is all accountable as additional length, then

$$\frac{\dot{l}_s}{l_s} = \frac{\dot{m}}{m} = \frac{\int_{x_s}^{x_R} \sigma dx}{l_s \bar{Y}_{\max}}$$

The primary justification for computing x_R in this way is that it gives a closed bubble in the limit of steady separated flow. At the onset of stall, when there is no potential-flow solution from which to derive a growth rate, i_s is assumed to equal U .

When the dead-air region terminates downstream of the trailing edge, the pressure at x_R is taken to be the free-stream pressure. If x_R is less than b , as occurs at the onset of leading-edge stall, the pressure at x_R is taken to be the pressure at that point if the airfoil were not stalled.

When the airfoil has undergone leading-edge stall, there must be some means of determining when the airfoil regains attached flow. Closely connected with this determination is the process by which reattachment occurs. It was assumed that when an airfoil regains attached flow after having undergone leading-edge stall, the dead-air region is washed off the airfoil from leading edge to trailing edge at the free-stream speed. To determine whether this process should be initiated, the following procedure was first attempted. It was postulated that during the previous time step, the airfoil had unstalled and the dead-air region was partially washed off the airfoil. After computing the potential flow with x_s so positioned, the boundary layer and leading-edge bubble were analyzed. If the leading-edge bubble burst, the postulated unstall could not have occurred and the analysis would proceed with the separation point restored to a position near the leading-edge. Unfortunately, this procedure caused difficulty with the boundary-layer analysis, because at large angles of attack the displaced dead-air region generated a local area of unfavorable pressure gradient near the stangation point, probably because of the inaccuracy of the linear potential-flow model used. The procedure was

therefore altered somewhat by removing the dead-air region entirely from the flow prior to analyzing the boundary layer and the leading-edge bubble. Of course, if it is found that the leading-edge bubble does not burst and unstall should be initiated, the washing off of the dead-air region is still carried out.

RESULTS OF COMPUTATIONS

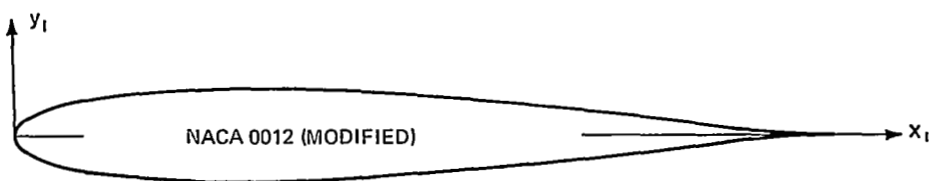
Calculations have been carried out of the loading on an airfoil during transient and sinusoidal pitching motions and during unsteady stall induced by a series of discrete vortices convected past the airfoil at the free-stream speed. Two different airfoil sections were analyzed. These sections, which are sketched with their offsets in Figure 8, were the ones used in the tests reported in Ref. 3. The symmetric section is an NACA 0012 section modified by a small trailing-edge extension. The cambered section, designated V-23010 in Ref. 3, was formed from a 0012 section by cambering the leading-edge portion.

All calculations were performed for a chordal Reynolds number of two million ($Re_b = 10^6$). The measured static variation of lift and moment, from Ref. 19, indicate that the sections analyzed undergo leading-edge stall at that Reynolds number. Preliminary calculations of the loading during transient pitching through stall confirmed this. Therefore, in order to conserve computer running time, the occurrence of trailing-edge stall was precluded by omitting the analysis of the turbulent boundary layer downstream of the leading-edge bubble. Thus, the possibility of unsteady effects suppressing leading-edge stall to the extent that trailing-edge stall dominates were not taken into account in the computations. However, there is no indication in the data of Ref. 19 that trailing-edge stall occurs under the conditions analyzed.

Transient Pitching Motion and Static Stall Characteristics

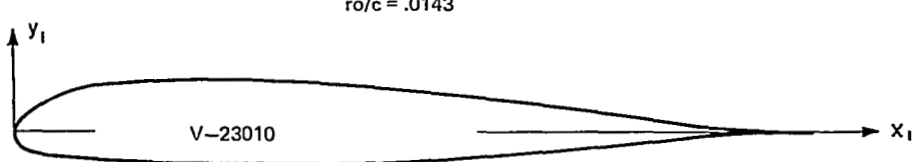
Computations of the loading resulting from transient pitching motions have been carried out for both airfoil sections. Pitch angle was increased linearly with time up to a selected value and then held constant until steady loading on the airfoil was established. The variation of pitch angle, normal-force coefficient, moment coefficient and length of the dead-air region with time, for a typical case, are shown in Figure 9.

Of particular note in Figure 9 is that the instantaneous normal force exceeds the maximum static value computed by a considerable margin at stall. There are two effects contributing to the overshoot. One of these is a redistribution of loading over the chord, caused by the pitch rate, which reduces the suction peak and pressure gradient near the leading edge. This can be seen from a comparison of various flow quantities for static and dynamic loading below stall as listed in Table II. The quantities for unsteady



x_1/c	Y_u/c
0	0
.0110	.0170
.0220	.0230
.0330	.0270
.0540	.0340
.0760	.0390
.1087	.0445
.1521	.0493
.2065	.0527
.2500	.0542
.3043	.0547
.3478	.0541
.4130	.0520

x_1/c	Y_u/c
0	0
.4564	.0499
.5000	.0472
.5434	.0439
.6086	.0383
.6521	.0343
.6955	.0300
.7607	.0230
.8042	.0181
.8477	.0127
.8911	.0070
.9346	.0011
1.000	.0011



x_1/c	Y_u/c	Y_L/c
0	0	0
.0056	.0144	-.0122
.0096	.0185	-.0148
.0135	.0220	-.0162
.0254	.0307	-.0184
.0333	.0353	-.0193
.0571	.0456	-.0216
.0967	.0563	-.0249
.1462	.0635	-.0287
.1957	.0662	-.0324
.2452	.0661	-.0355

x_1/c	Y_u/c	Y_L/c
.2848	.0653	-.0369
.3937	.0609	-.0373
.4729	.0557	-.0351
.5521	.0492	-.0316
.6313	.0414	-.0267
.7502	.0277	-.0174
.8293	.0174	-.0102
.9086	.0066	-.0027
.9440	.0022	.0001
1.0	0	0

$r_0/c = .0158$

Figure 8 AIRFOIL SECTIONS

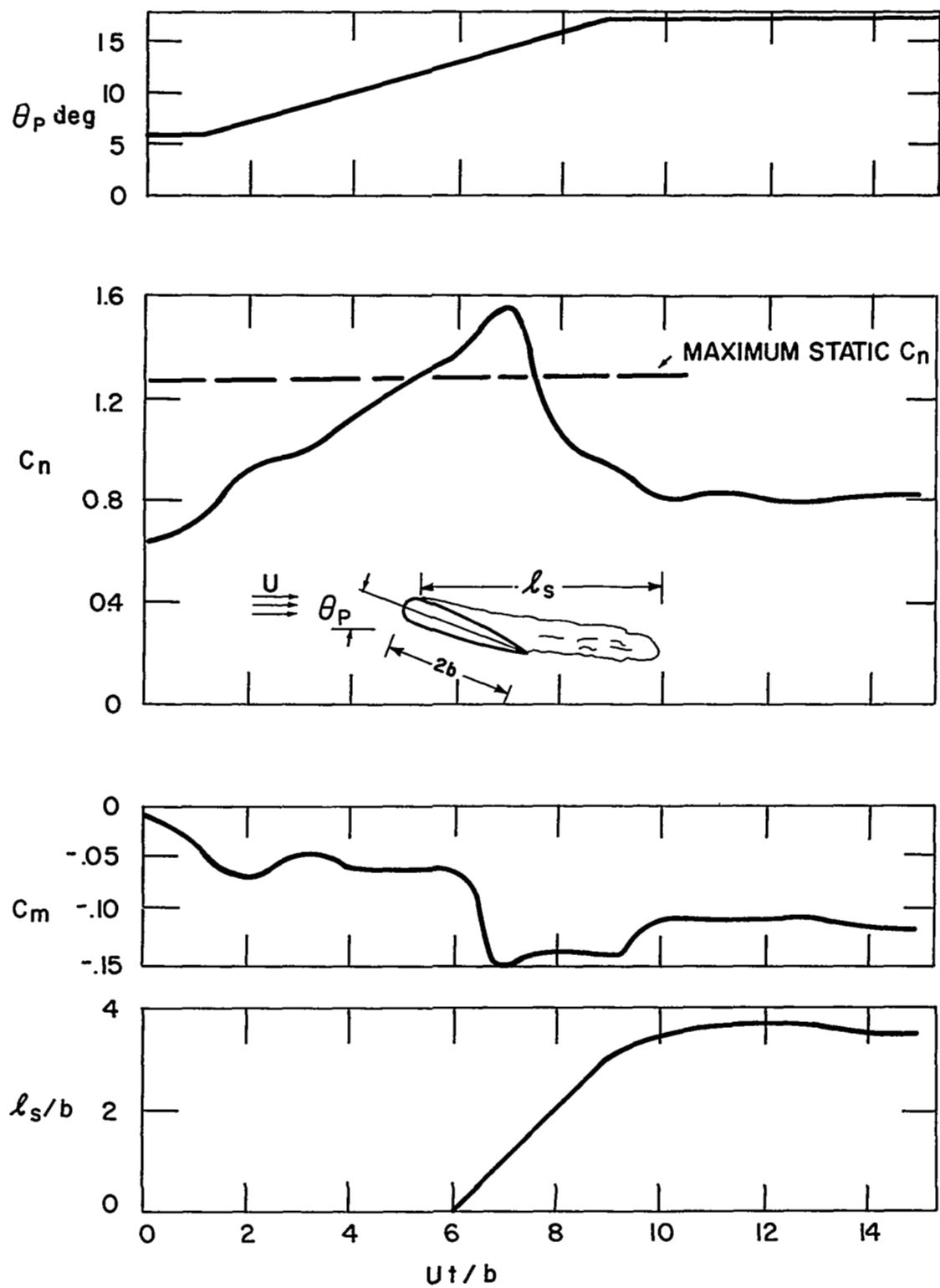


Figure 9 TRANSIENT LOADING ON SYMMETRIC AIRFOIL

TABLE II
COMPARISON OF STATIC AND DYNAMIC LOADING BELOW STALL

Quantity	Static	Dynamic ($b\dot{\theta}_p/U = .025$)
θ_p -deg.	11.5	12.9
C_n	1.252	1.354
q_e_{max}/U	2.985	2.892
q_e_s/U	2.832	2.742
Length of leading edge bubble-semichords	.0256	.0265
Increase in C_p possible	2.095	1.964
Increase in C_p required	2.093	1.949

loading were taken from the run plotted in Figure 9 at the instant when $\theta_p = 12.9$ deg. The normal force in the unsteady case is seen to exceed the static normal force, even though the maximum flow at the surface, and hence the suction peak, is considerably less for the dynamic than for the static loading. As can be seen from the comparison of the pressure distributions for the two cases shown in Figure 10, the additional normal force is generated over the aft 90 percent of the chord on the pitching airfoil, the loading near the leading edge being slightly less than on the static airfoil. This is caused by the pressure distribution associated with the pitch rate, the boundary condition for which is equivalent to parabolic camber on an airfoil in steady flow. The effective camber shifts the center of pressure rearward, reducing the suction peak. As can be seen from Table II, the reduced flow magnitude at separation in the dynamic case makes the separation bubble longer and decreases the amount of pressure rise in the bubble which is possible, but this is more than offset by the reduction in pressure gradient, which lowers the required pressure rise even more. The reduction in pressure gradient in unsteady flow was in fact postulated by Carta in Ref. 20 as a mechanism for dynamic overshoot, without considering the direct effect on the leading-edge bubble.

The other effect contributing to the increased normal force derives from the flow which results when the dead-air region terminates on the airfoil. When the reattachment point is in the vicinity of midchord, the presence of the bubble induces a substantial increase in loading over the aft portion of

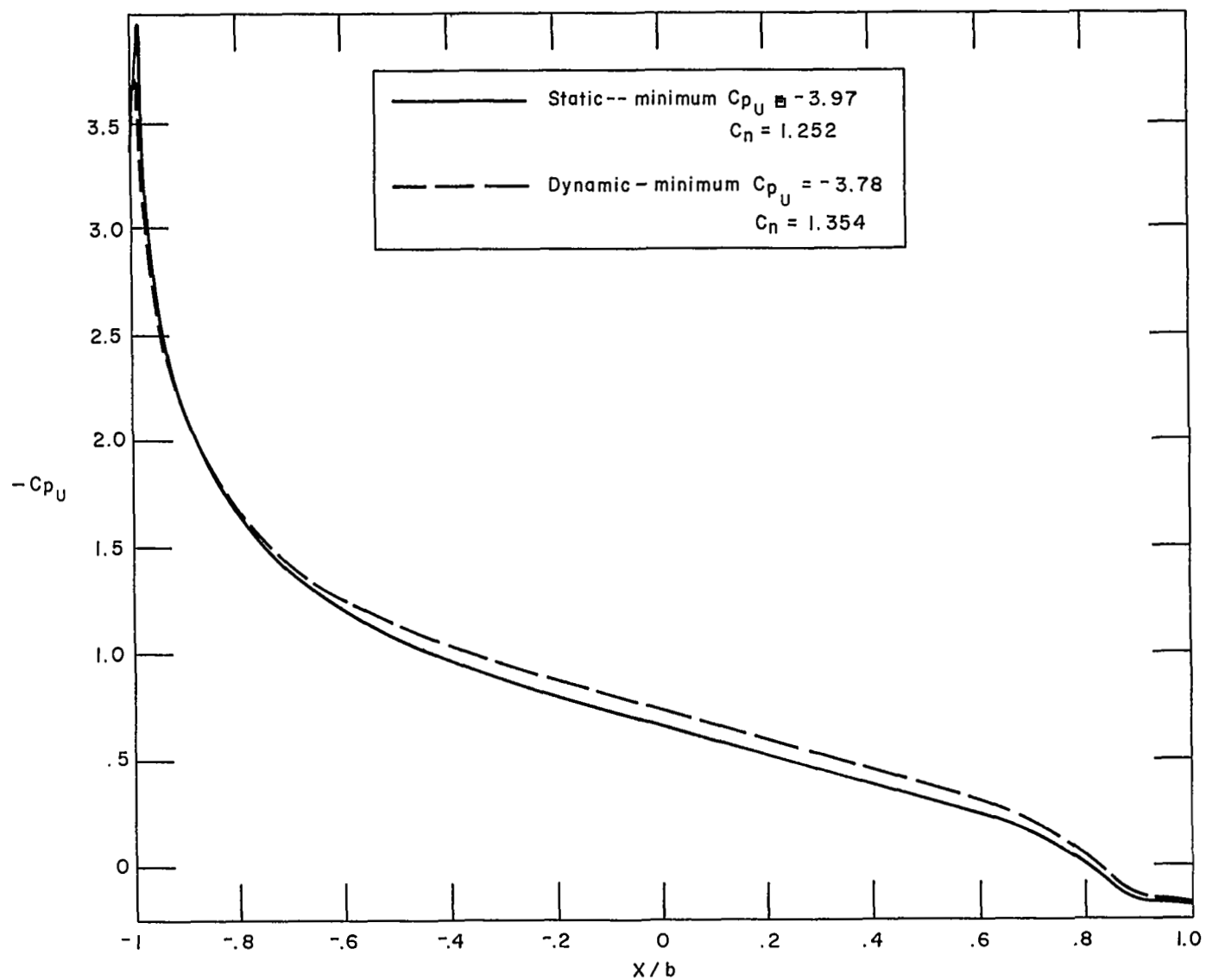


Figure 10 COMPARISON OF PRESSURE DISTRIBUTIONS BELOW STALL

the airfoil which more than compensates for any loss in lift over the dead-air region, resulting in a net increase in normal force. This can be seen from the variation of pressure coefficient over the chord plotted in Figure 11 for three different pitch angles, taken from the run plotted in Figure 9. For $\theta_p = 14.3$ deg., the dead-air region extends from very close to the leading edge to approximately midchord. The loading is seen to exceed that for $\theta_p = 12.9$ deg (just prior to bursting) over the whole aft portion of the airfoil, resulting in a normal-force coefficient of 1.59, compared to 1.35 at $\theta_p = 12.9$ deg. When the reattachment point reaches the trailing edge and beyond, the loading rapidly drops to near the static variation during stall, as can be seen from the variation of C_{pU} for $\theta_p = 17.2$ deg in Figure 11.

Of further note in Figure 11 is the similarity of the pressure distribution for $\theta_p = 14.3$ deg to that which would be induced by a strong vortex. Vorticity which is shed from the leading edge has been postulated (Ref. 4) as a primary potential-flow element of dynamic stall. Shed vorticity emanating from the leading edge is not a part of the model employed, per se, so a different explanation is required. From a mathematical standpoint, the cause of the sharp rise in suction downstream of reattachment is the square-root singularity* in y required there to satisfy the flow-tangency condition. A physical interpretation could be that fluid, upon passing from a region of nearly constant pressure to one of attached flow, must accelerate in a manner analogous to passage over a leading edge, causing a sharp suction peak.

The variation of static normal-force and moment coefficients with angle of attack were developed from the transient pitch computations by parametrically varying the maximum pitch angle. The curves for the symmetric and cambered sections, and the corresponding measured coefficients from Ref. 19, are shown in Figures 12 and 13. The computed and measured static coefficients are seen to agree quite well, qualitatively. That the method so accurately predicts the maximum normal force on the symmetric section was fortuitous, in light of the approximations made in the calculations, and should not be regarded as a measure of the quantitative capabilities of the method. The differences between measured and calculated coefficients for the cambered section (Figure 13) can be attributed in part to a larger camber effect in the computed result, there being a considerably larger predicted normal force at $\alpha = 0$ than was measured. Also, the center of pressure is quite a bit aft of the quarter-chord in the predicted load, as reflected in the moment variation. Apparently the linearized model introduces a relatively large error when used to represent camber of this type.

Sinusoidal Pitch Oscillations

Computations were carried out of the load on both symmetric and cambered sections resulting from sinusoidal pitching about the quarter-chord. Because the calculations were initiated from steady flow, it was necessary to carry out the computations until periodic loading was established. It was found that

*The singularity results from the linearized boundary condition. A uniformly valid solution which is finite at the reattachment point could be derived using Lighthill's approach, but it was not needed, because the boundary layer is not analyzed in the vicinity of that point.

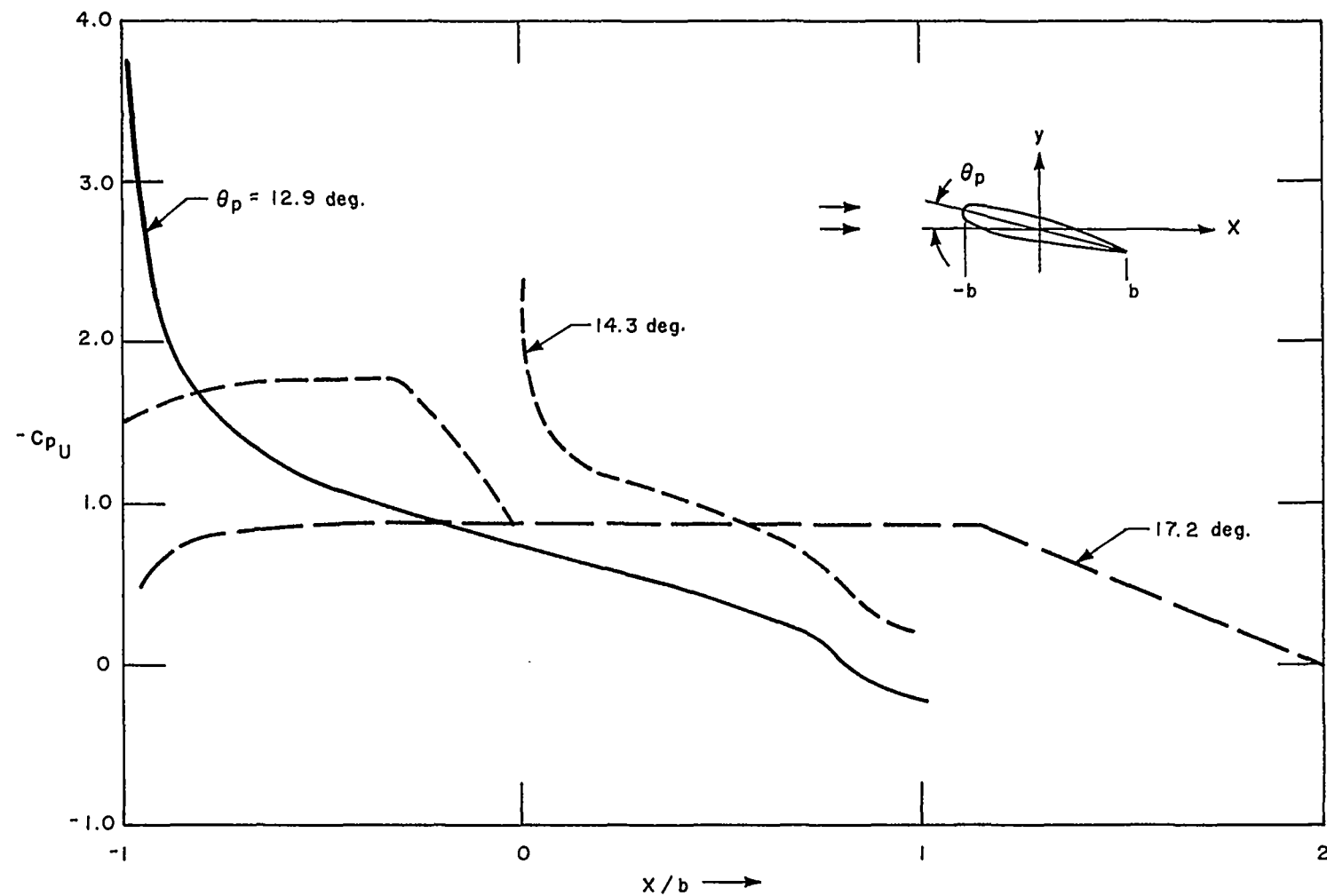


Figure 11 PRESSURE DISTRIBUTIONS DURING UNSTEADY STALL

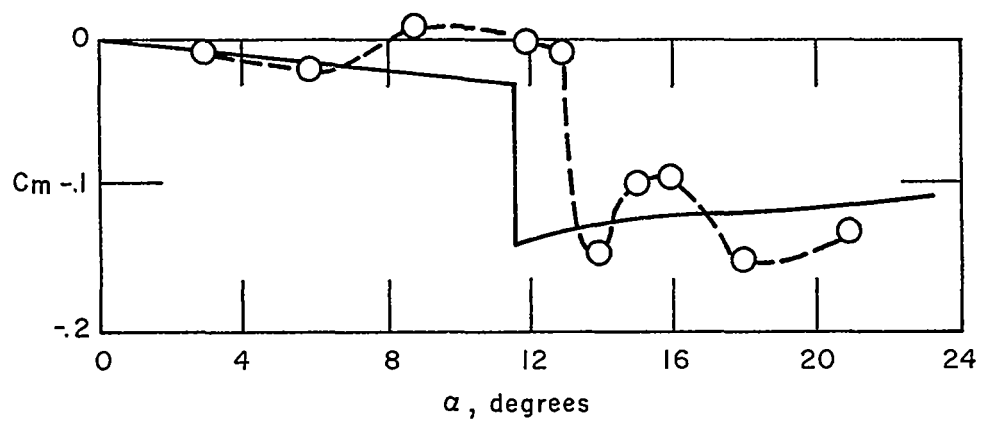
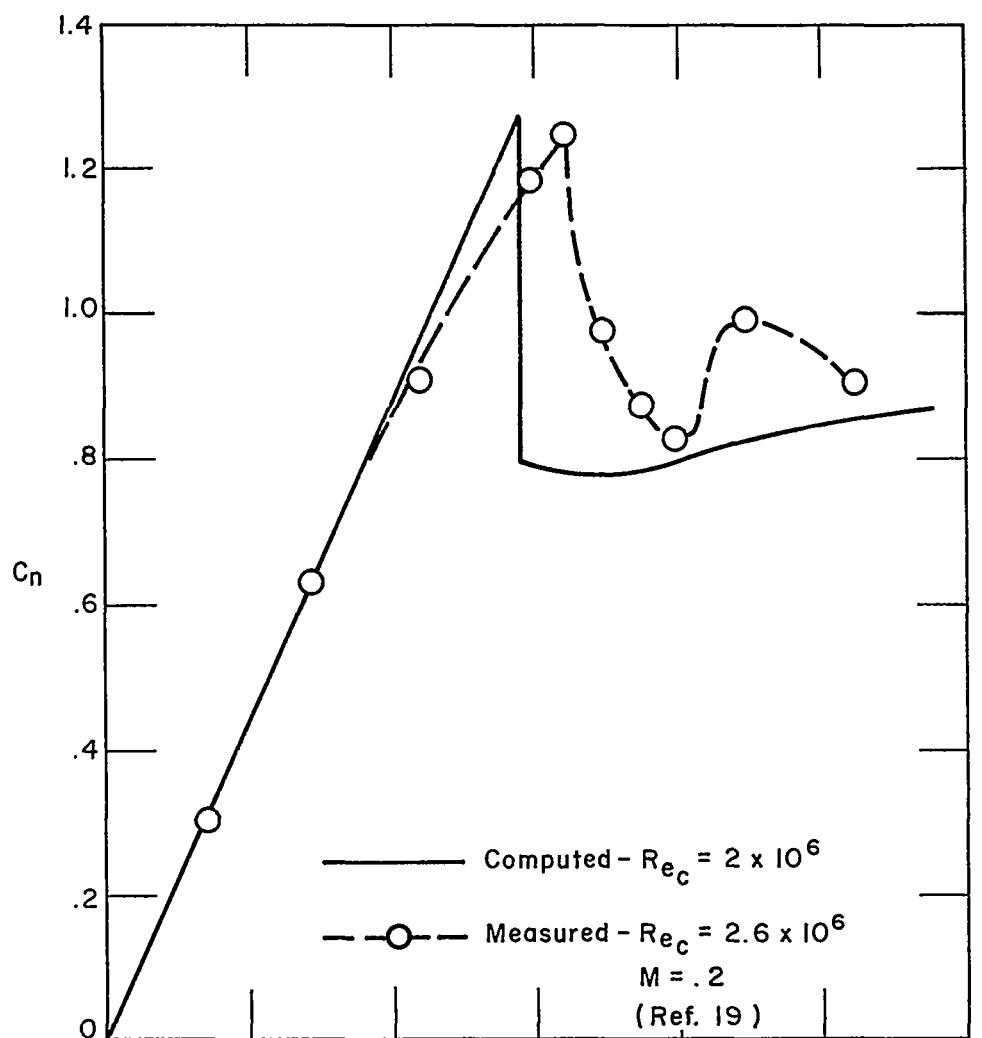


Figure 12 STATIC NORMAL-FORCE AND MOMENT COEFFICIENTS

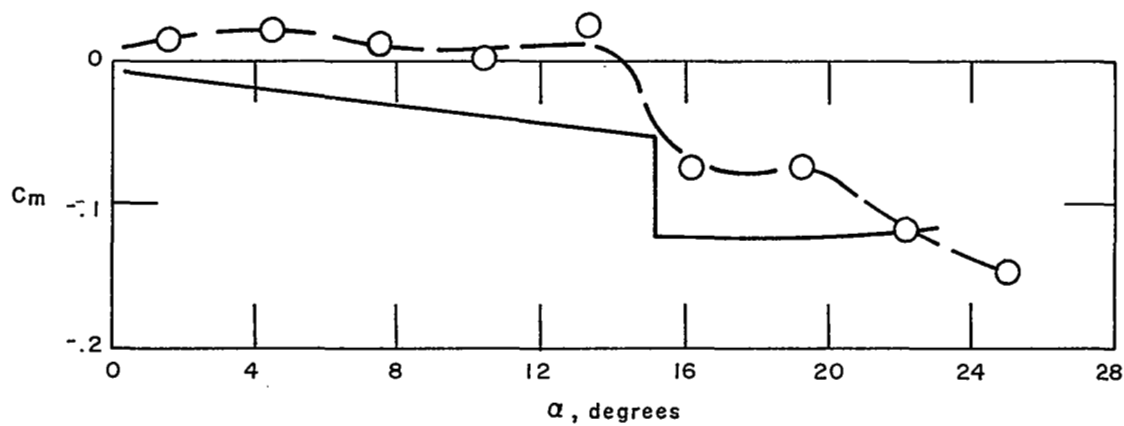
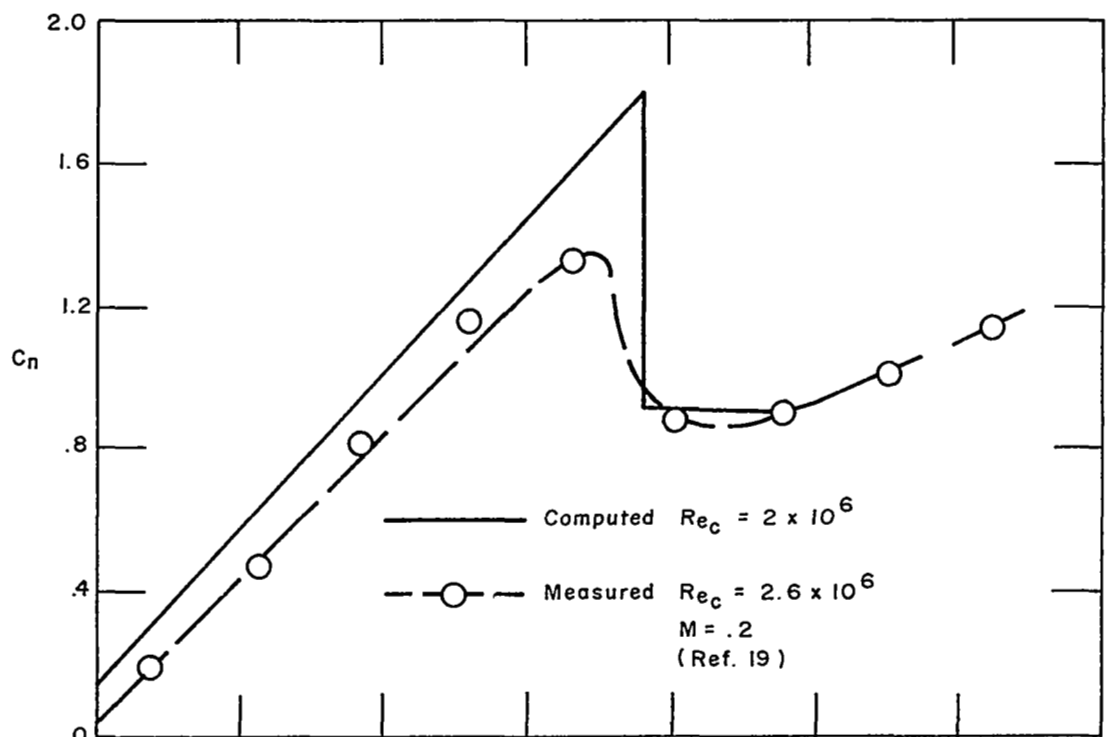


Figure 13 STATIC NORMAL-FORCE AND MOMENT COEFFICIENTS FOR CAMBERED AIRFOIL

just two cycles of oscillation were sufficient to obtain periodicity. The time increment was selected to give 36 time-steps per cycle of oscillation. A typical run required about 40 minutes of central processor time, using an IBM 360/75 computer.

Symmetric section. — The results of the computations for the symmetric section are shown in Figures 14 through 19 as plots of normal-force and moment coefficient vs. pitch angle. The static variation of those coefficients is shown as dashed curves on the figures. The loading for a reduced frequency k ($k = \omega b/U$, where ω is circular frequency) of .13 is given in Figures 14, 15, and 16 and $k = .26$ for Figures 17, 18 and 19. The amplitude of oscillation for all cases is 4.5 deg. The three mean pitch angles for each reduced frequency are 9, 13.5, and 15.5 degrees, as indicated on the figures.

For purposes of comparison, the measured loadings shown plotted in Figures 20 through 25 were obtained from the data given in Ref. 19. The parameters for those plots correspond nominally to those of Figures 14 through 19, respectively. The measured coefficients were computed from the harmonic analyses given in Ref. 19 of data taken from tests at a free-stream Mach number of .2.

It is noted, first, that the measured loads for $k = .13$ (Figures 20, 21, and 22) exhibit considerable dynamic overshoot of C_n , while none is evident in the computed results at that frequency (Figures 14, 15, and 16). The computed moment coefficient is in good agreement, qualitatively, with the measured coefficient, however. The unstable moment variation (loops traversed clockwise in a plot of C_m vs. θ_p) are in clear evidence, particularly at a mean pitch angle of 9 deg (Figure 14). Further, the variation of normal force during the process of flow reattachment exhibited in the measured loading is well reproduced in the computed result, there being an initial sharp rise in C_n as the dead-air region is being washed off, followed by a slight drop in C_n after the airfoil regains attached flow.

At the higher reduced frequency, the computed moment coefficients (Figures 17, 18, and 19) continue to exhibit the unstable variation in evidence in the experimental result (Figures 23, 24, and 25). Also, the computed normal-force coefficients for mean pitch angles of 9 and 13.5 degrees (Figures 17 and 18) are seen to exceed the maximum static value by a considerable margin. It would appear that overshoot is only detected at the higher frequency at least partly because of the substantial errors introduced by the linear model in computing the flow near the leading edge, because it was found in the analysis of transient pitching that bubble bursting is very sensitive to changes in the flow there.

In further comparison of the results at $k = .26$, it is noted that the measured C_n does not decrease as rapidly as the computed load at the onset of stall, making the experimental C_n loops considerably narrower than the computed ones. Because the decrease in computed normal force does not occur until the reattachment point has progressed to the vicinity of the trailing edge, it would appear that the rate of growth of the dead-air region, assumed to be equal to the free-stream speed in the analysis, is in fact a good deal less than the free-stream speed.

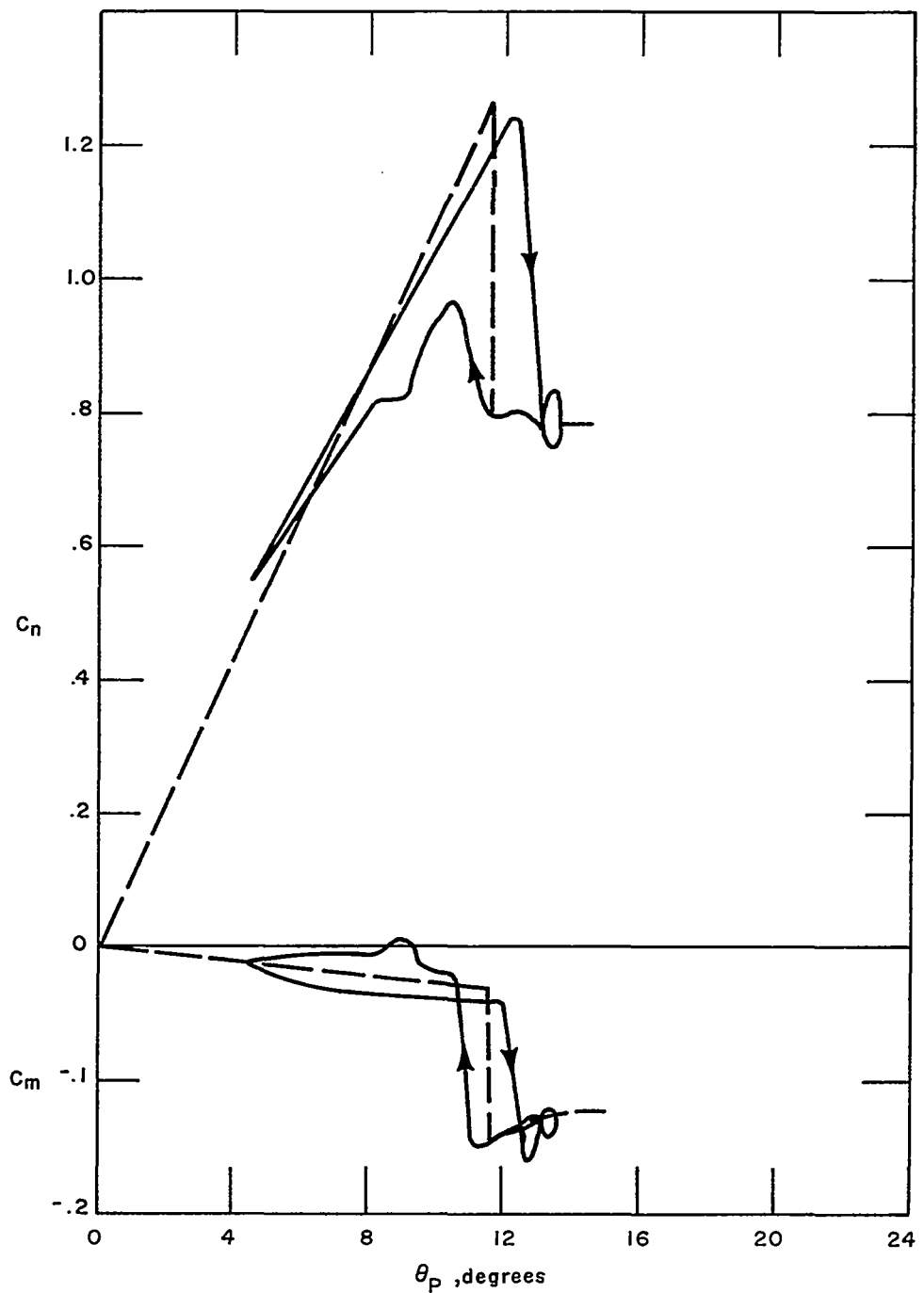


Figure 14 COMPUTED LOADING ON SYMMETRIC SECTION WITH $k = .13$ AND $\theta_0 = 9$ DEG.

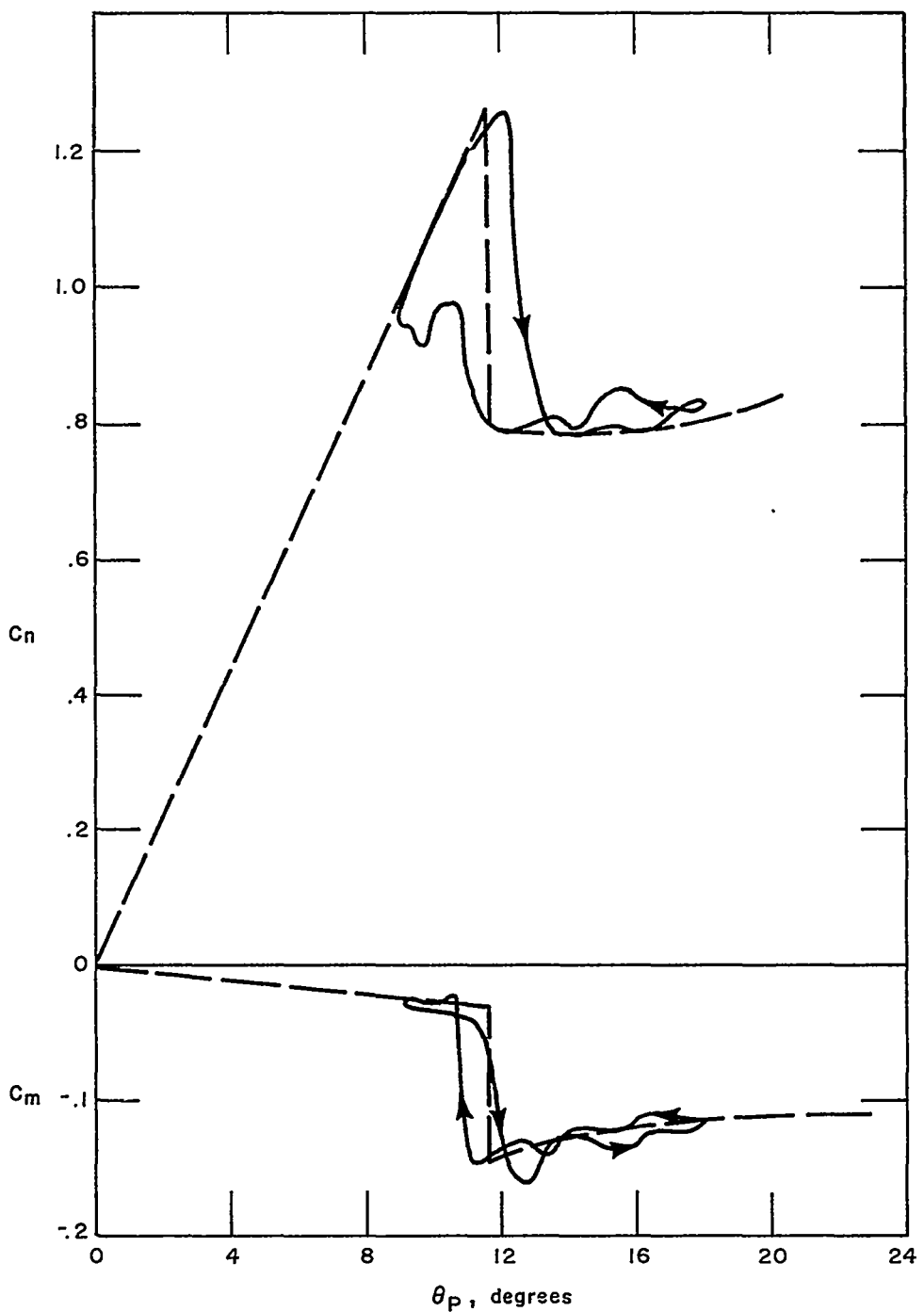


Figure 15 COMPUTED LOADING ON SYMMETRIC SECTION WITH $k = .13$ and $\theta_0 = 13.5$ DEG.

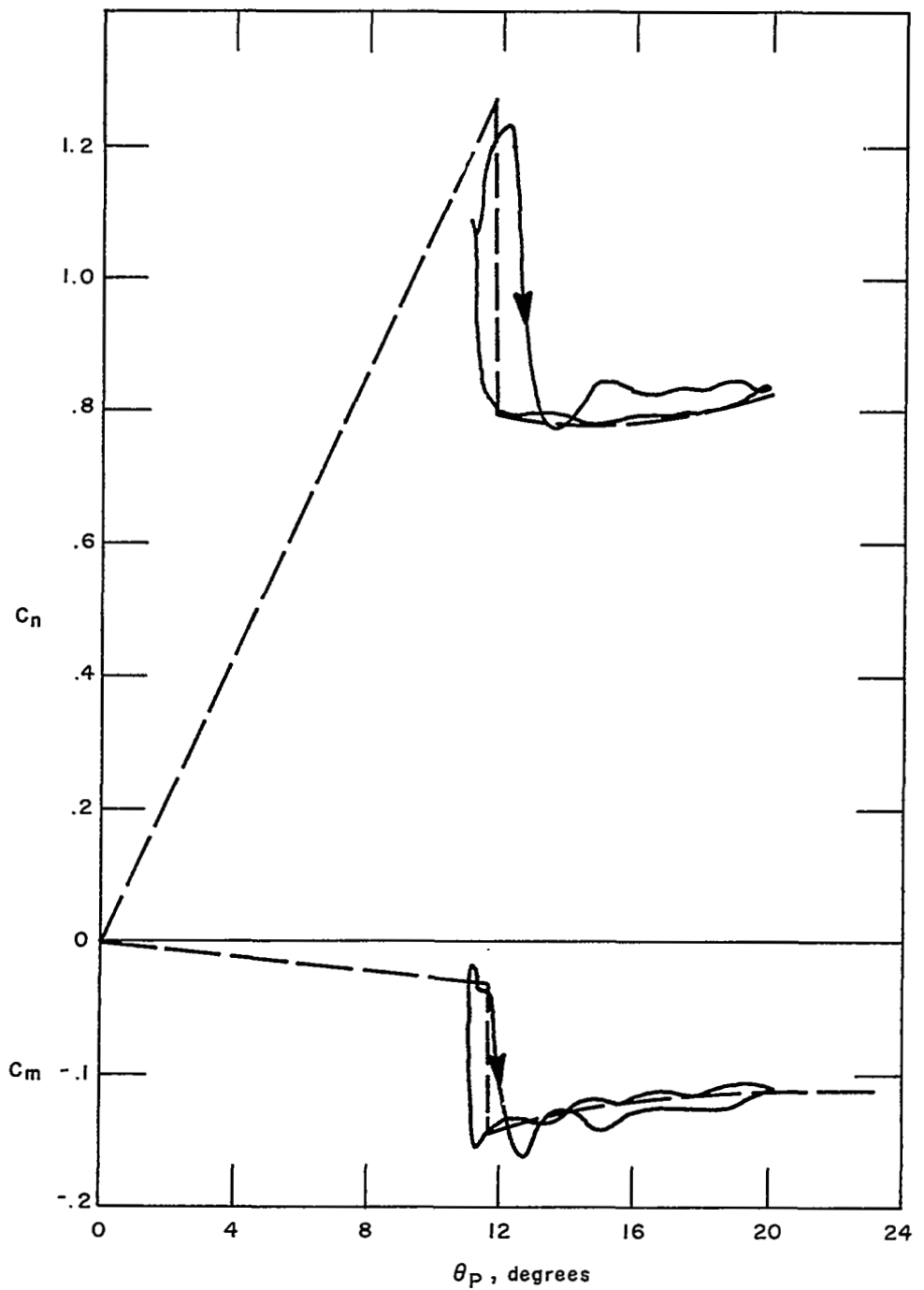


Figure 16 COMPUTED LOADING ON SYMMETRIC SECTION WITH $k = 0.13$ AND $\theta_0 = 15.5$ DEG.

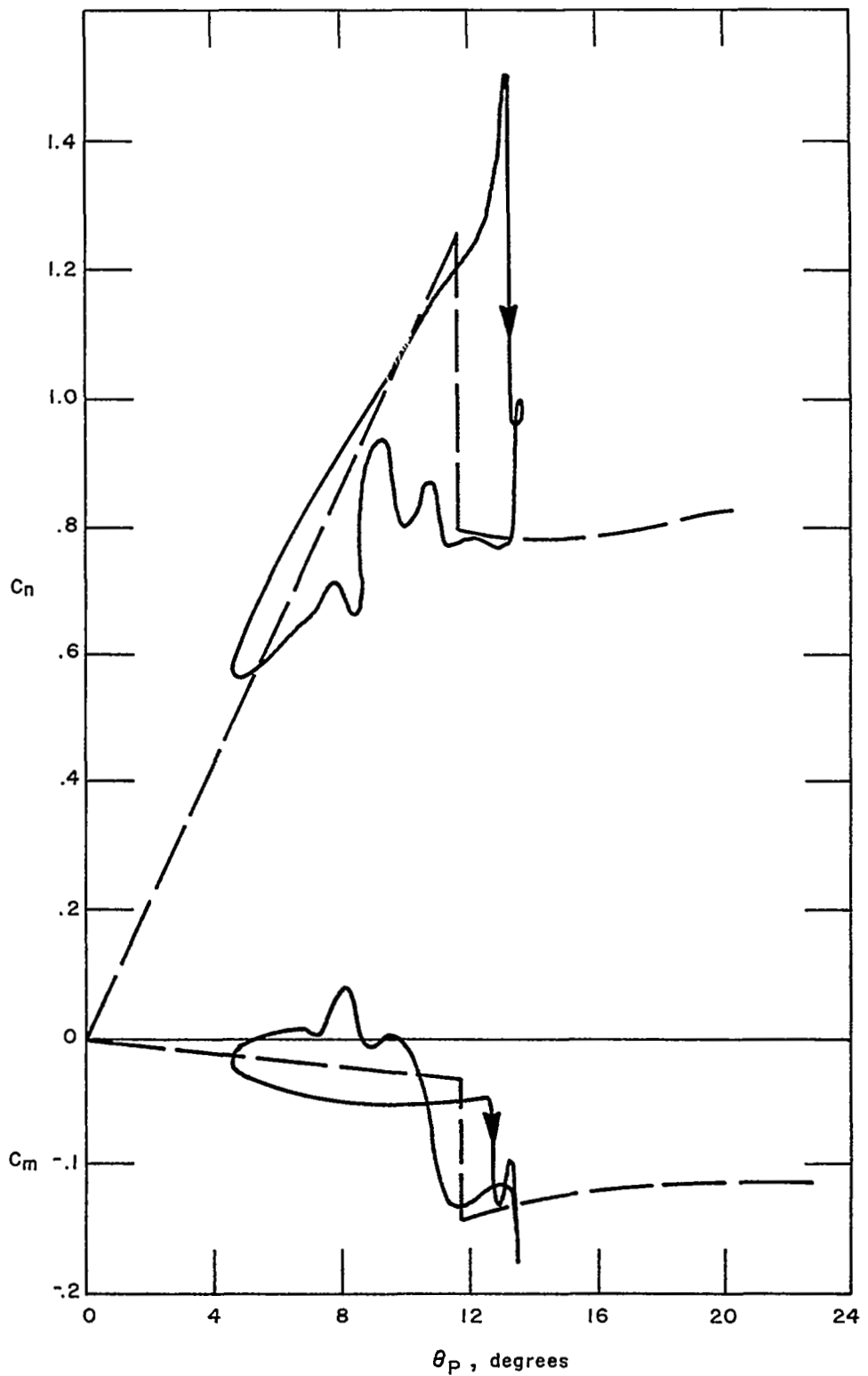


Figure 17 COMPUTED LOADING ON SYMMETRIC SECTION WITH $k = .26$ AND $\theta_0 = 9$ DEG.

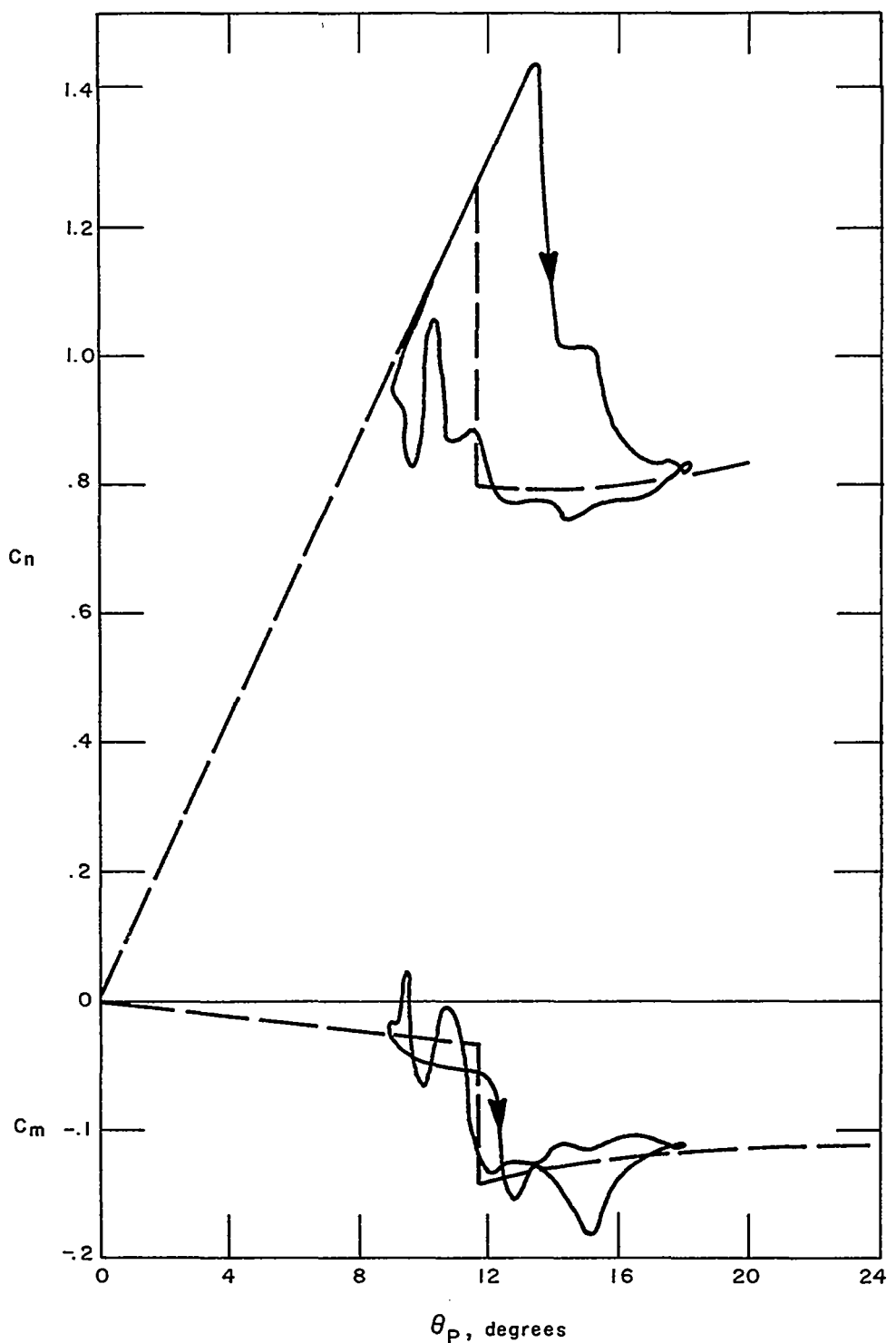


Figure 18 COMPUTED LOADING FOR SYMMETRIC SECTION WITH $k = .26$ AND $\theta_o = 13.5$ DEG.

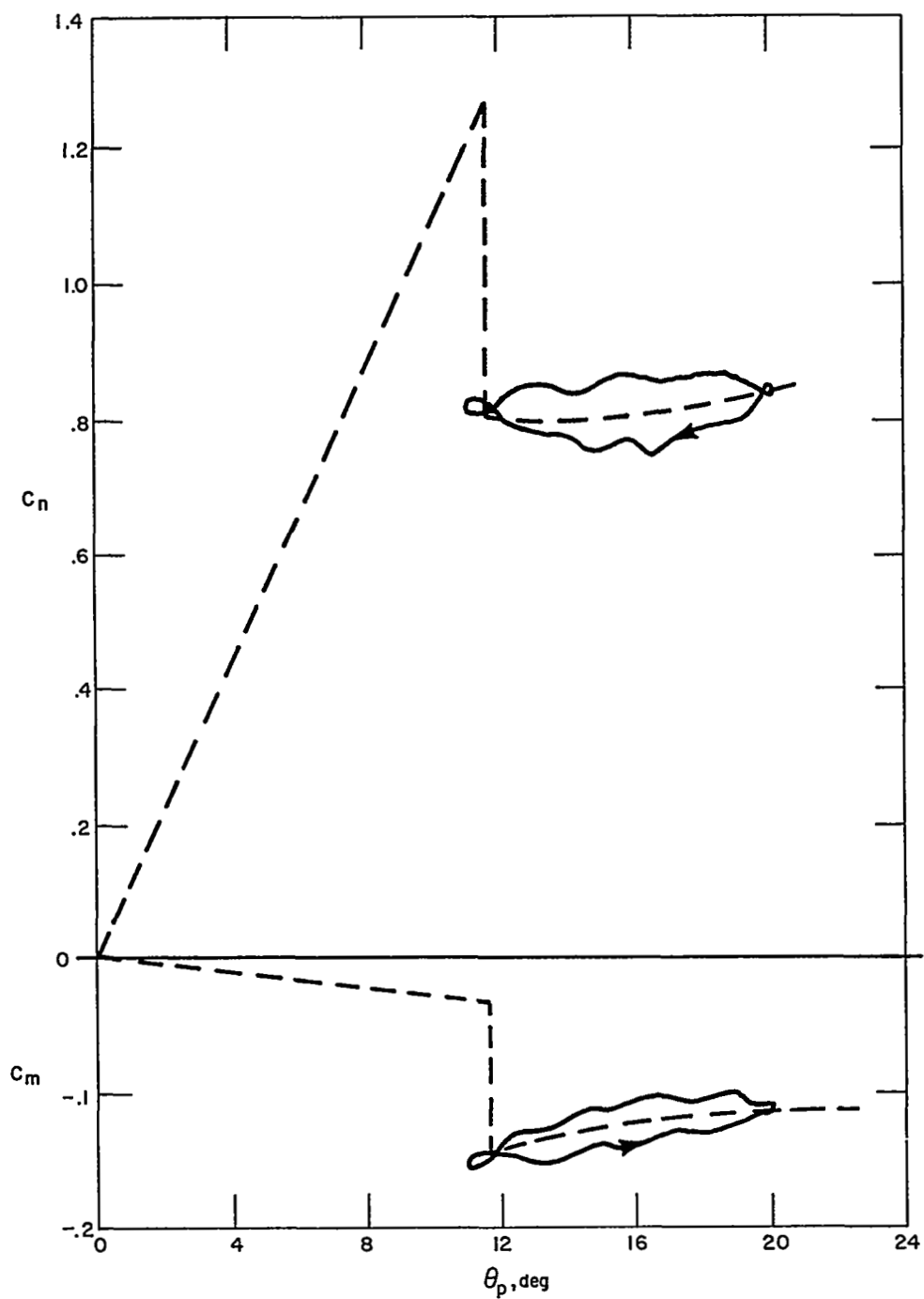


Figure 19 COMPUTED LOADING ON SYMMETRIC SECTION WITH $k = .26$ AND $\theta_0 = 15.5$ DEG.

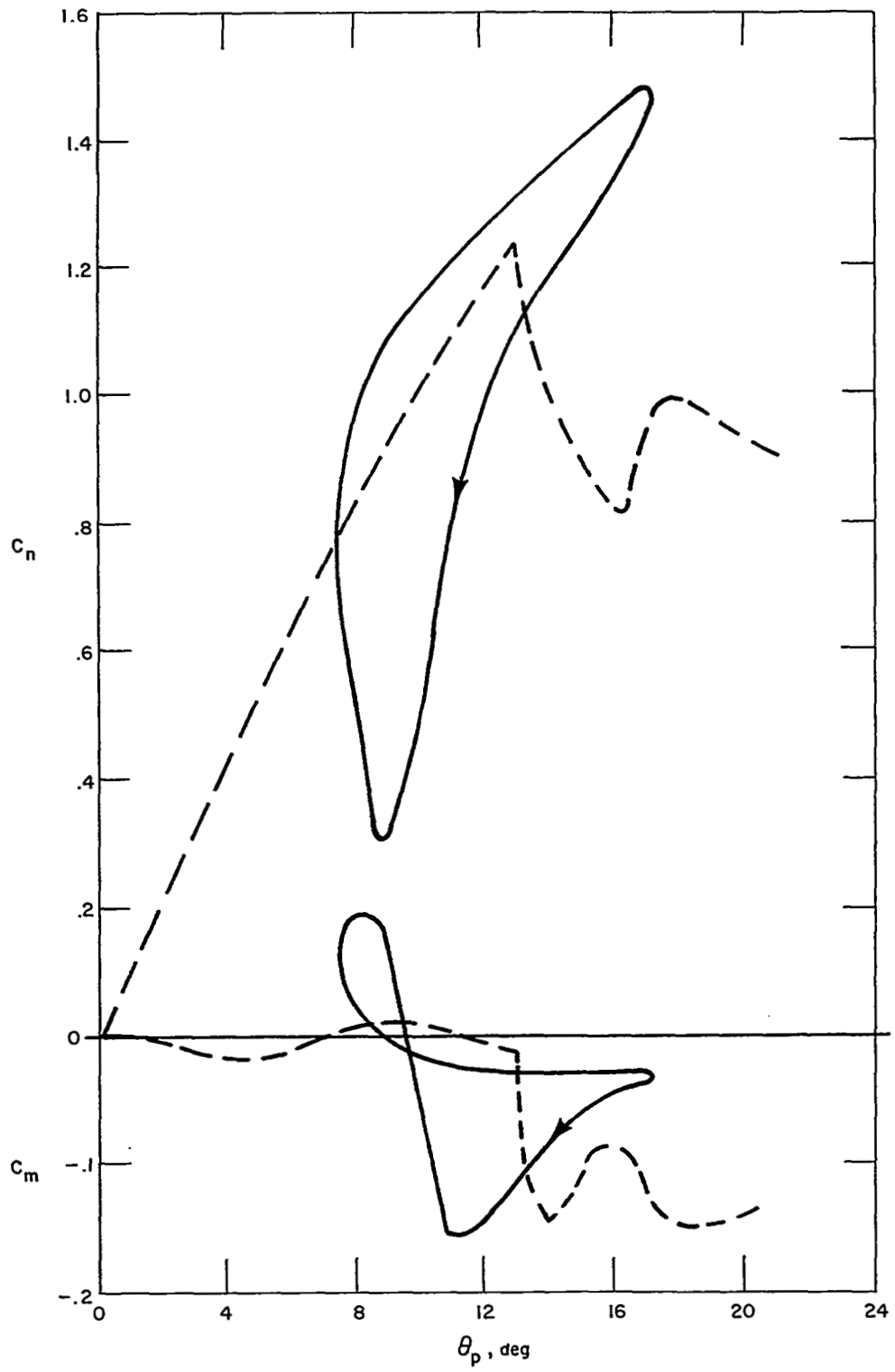


Figure 20 MEASURED LOADING ON SYMMETRIC SECTION WITH $k = .128$, $\theta_0 = 12.24^\circ$,
 $\Delta\theta = 4.84^\circ$ (from Ref. 19)

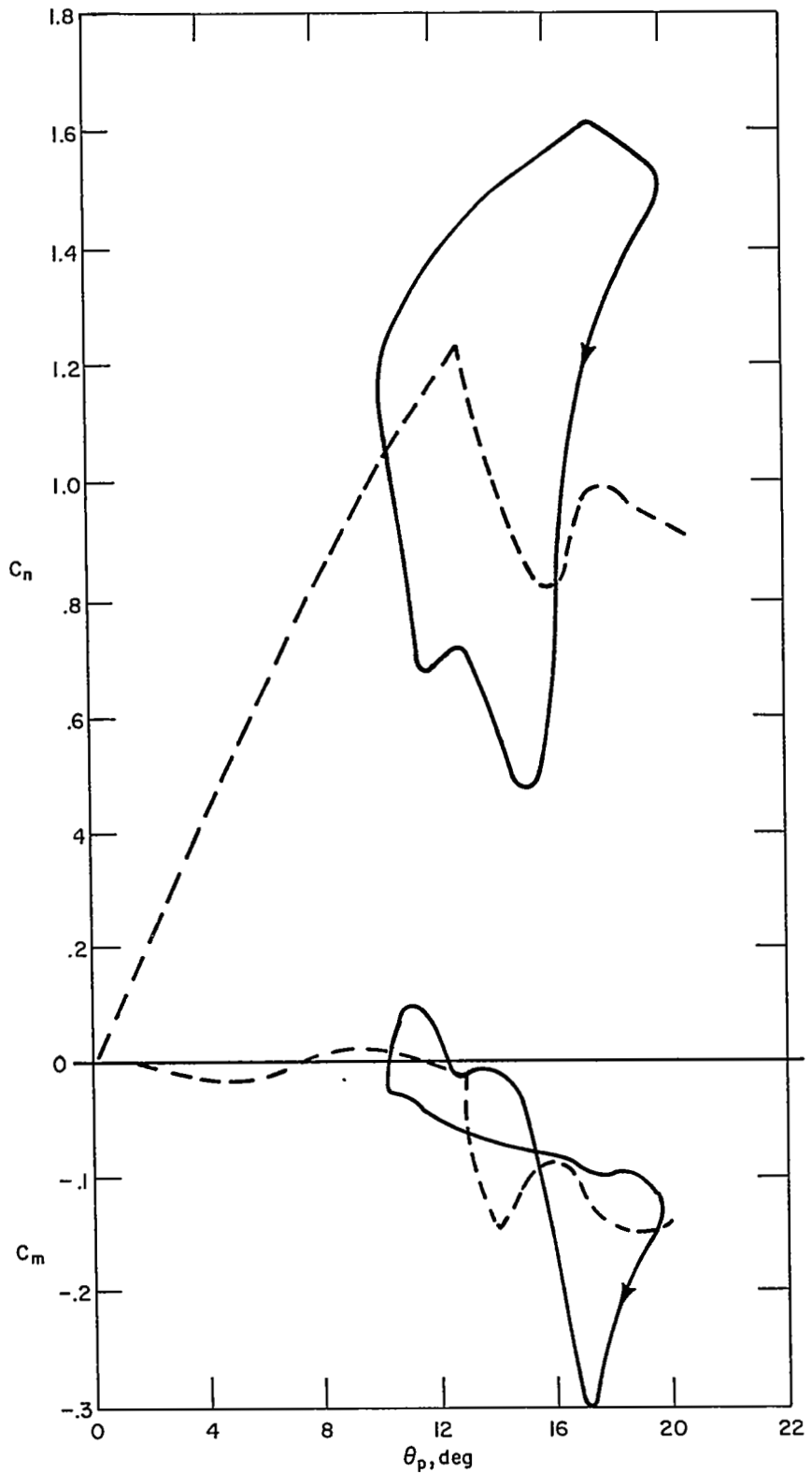


Figure 21 MEASURED LOADING ON SYMMETRIC SECTION WITH $k = .126$, $\theta_0 = 14.85^\circ$,
 $\Delta\theta = 4.75^\circ$ (from Ref. 19)

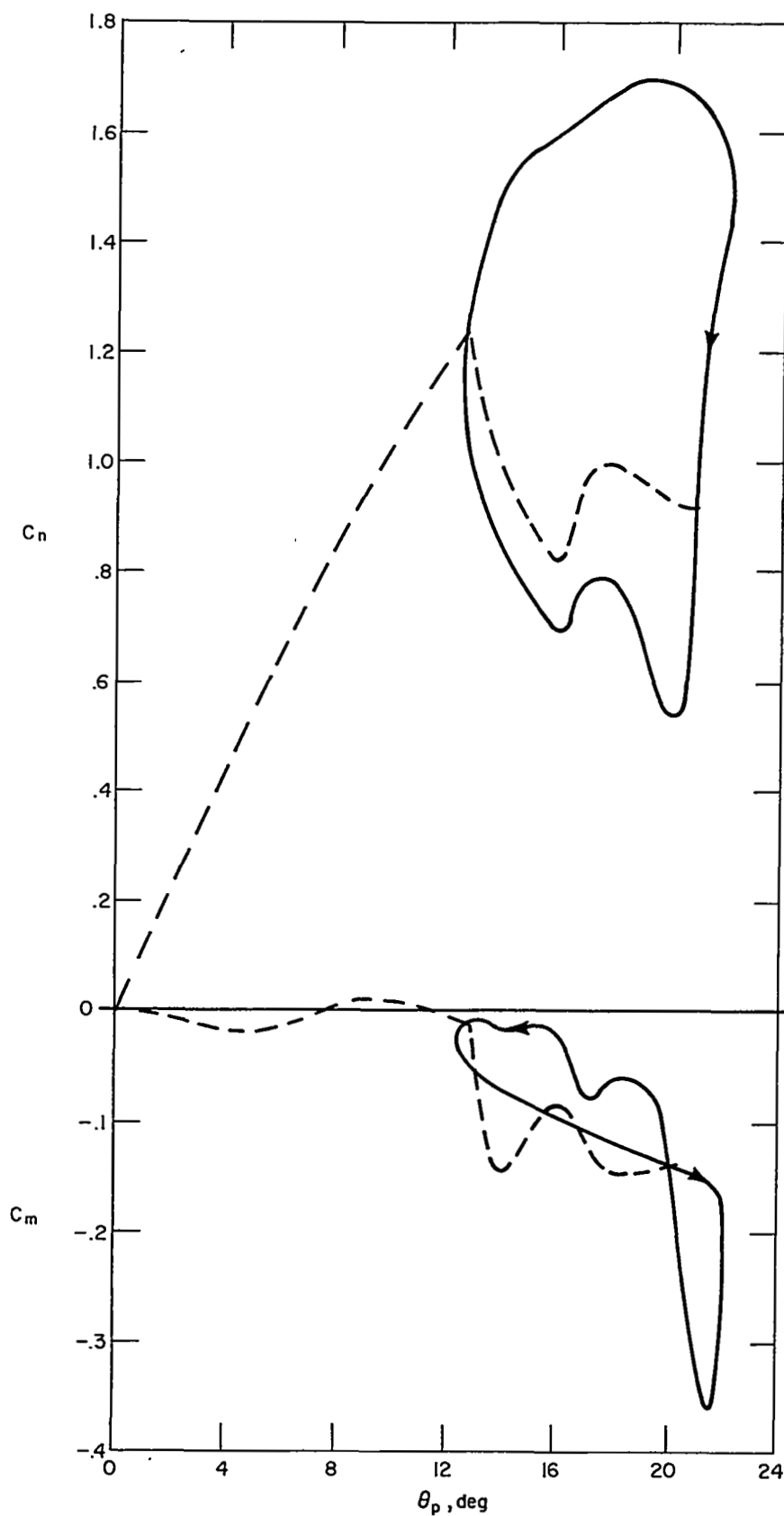


Figure 22 MEASURED LOADING ON SYMMETRIC SECTION WITH $k = .131$, $\theta_0 = 17.36^\circ$,
 $\Delta\theta = 4.88^\circ$ (from Ref. 19)

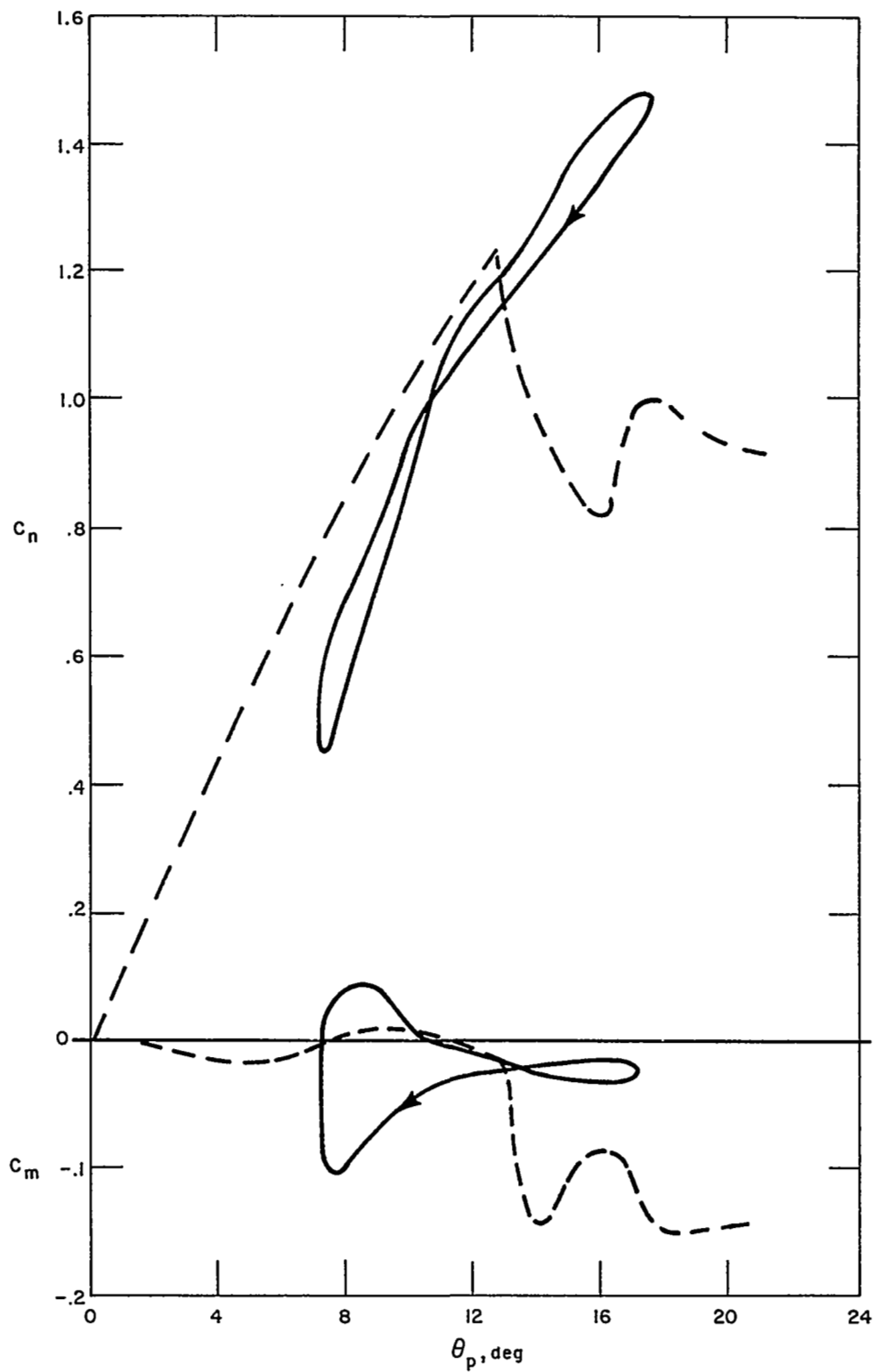


Figure 23 MEASURED LOADING ON SYMMETRIC SECTION WITH $k = .253$, $\theta_0 = 12.47^\circ$,
 $\Delta\theta = 5.13^\circ$ (from Ref. 19)

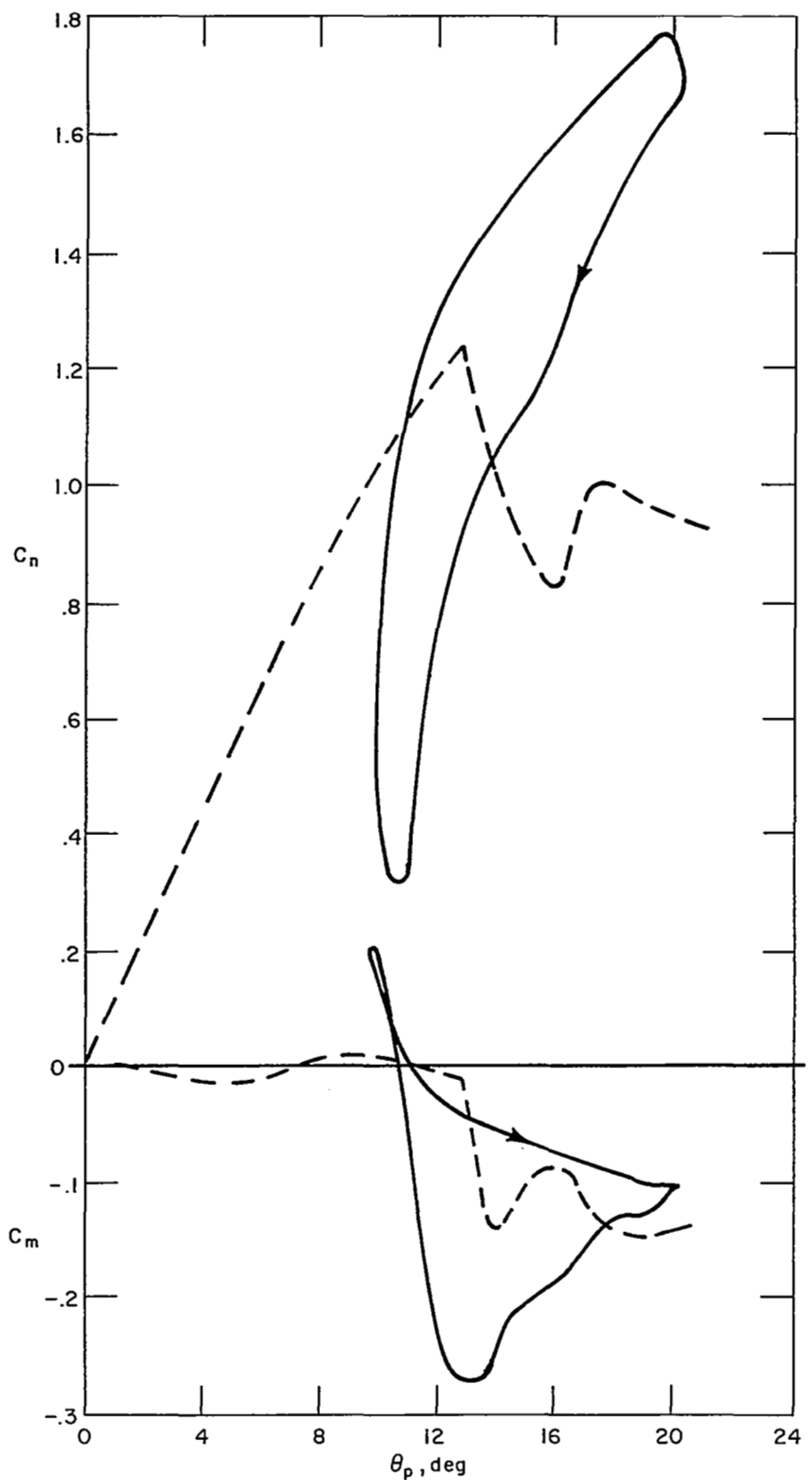


Figure 24 MEASURED LOADING ON SYMMETRIC SECTION WITH $k = .252$,
 $\theta_0 = 14.94^\circ$, $\Delta\theta = 5.14^\circ$ (from Ref. 19) .

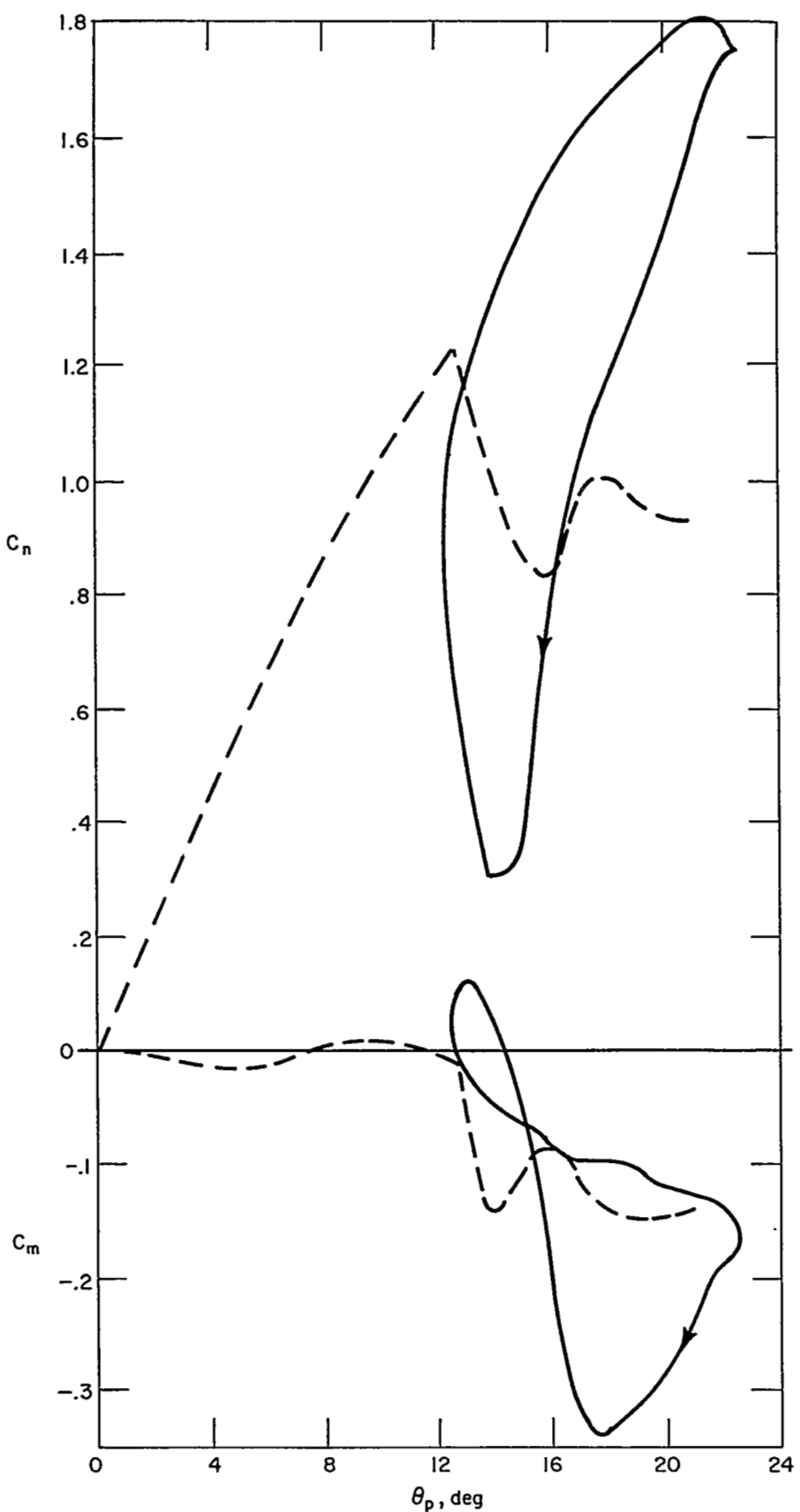


Figure 25 MEASURED LOADING ON SYMMETRIC SECTION WITH $k = .252$,
 $\theta_0 = 17.5^\circ$, $\Delta\theta = 5.12^\circ$ (from Ref. 19)

For the case computed with the highest pitch angle at $k = .26$ (Figure 19), it can be seen that the airfoil remained stalled throughout the cycle, while the measured results at the same frequency and comparable pitch angle (Figure 25) indicate the airfoil did unstall. It is interesting to compare Figure 19 with the measured load for a case where the airfoil did remain stalled. The result for such a case, also with $k = .26$, is plotted in Figure 26. Note in Figure 26 that the airfoil developed a substantial increase in load while pitching up, but the computed results show only a slight increase in C_n over that part of the cycle. This indicates that there is a significant variation of pressure in the viscous mixing region caused by unsteady effects which are not being taken into account in the analysis because a quasi-steady model of that region was used.

Cambered section. — It was found in Ref. 3 that the cambered section generally exhibited smaller excursions (less negative values) of C_m and reattachment started earlier in the cycle, compared to the results for the symmetric section. The load on the cambered section was computed to determine whether these effects could be detected. The results for reduced frequencies of .13 and .26 are plotted in Figures 27 and 28, respectively. Both cases have a mean pitch angle of 15.5 degrees and pitch amplitude of 4.5 degrees. Because the stall angle of attack of the cambered section is considerably larger than that of the symmetric section, Figures 27 and 28 are most closely comparable to Figures 15 and 18, respectively. The moment coefficients of the cambered section appear to be about the same magnitude as those of the symmetric section. However, reattachment for the cambered section does occur significantly earlier in the cycle, in agreement with the findings of Ref. 3. Note that substantial overshoot of C_n again occurs only at the higher frequency.

Wake-Induced Stall

The method was applied to the analysis of wake-induced dynamic stall of a rotor blade during a maneuver. Large high-frequency oscillations in differential pressure Δp , torsional moment TM , lift and aerodynamic moment on the retreating side, with blade azimuth angle ψ between 270 and 360 degrees, were detected in flight test data, as shown in plots of Figures 29 and 30, taken from Ref. 21. It was asserted in Ref. 21 that this response was the result of dynamic stall induced by previously formed tip vortices which, under the maneuver flight condition, pass under the blade at the azimuth positions indicated in Figures 29 and 30. To test this hypothesis, calculations were carried out of loading resulting from passage of a two-dimensional airfoil over a series of three equally spaced discrete vortices. The airfoil was free to respond in pitch about its quarter-chord point, with spring restraint and inertia chosen to give a reduced natural frequency $k_f = \omega_f b/U$ of .382, which corresponds to a pitch natural frequency of about 40 Hz for the parameters of the flight test. Pitch angle was computed from

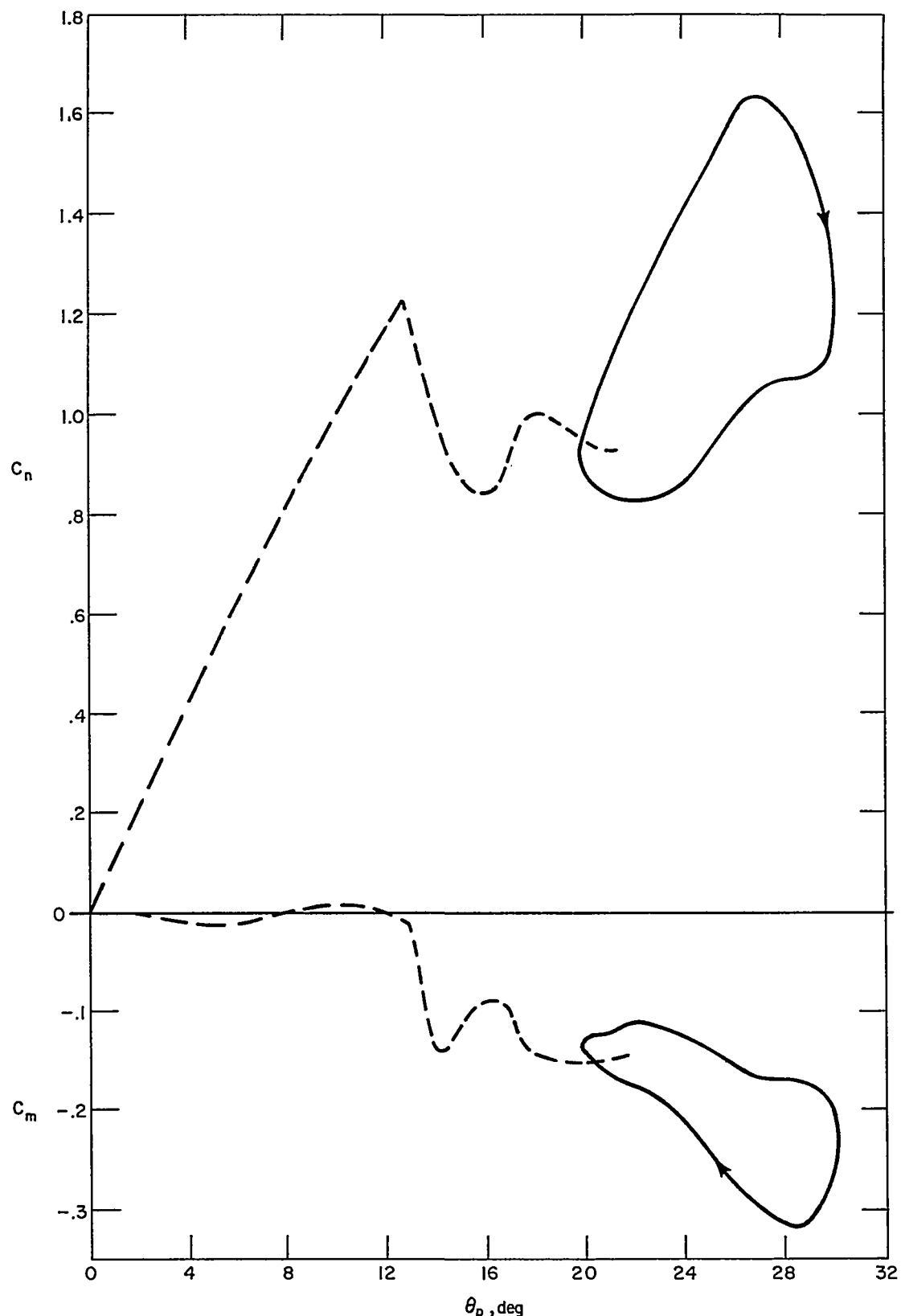


Figure 26 MEASURED LOADING ON SYMMETRIC SECTION WITH $k = .255$,
 $\theta_0 = 24.97^\circ$, $\Delta\theta = 5.15^\circ$ (from Ref. 18)

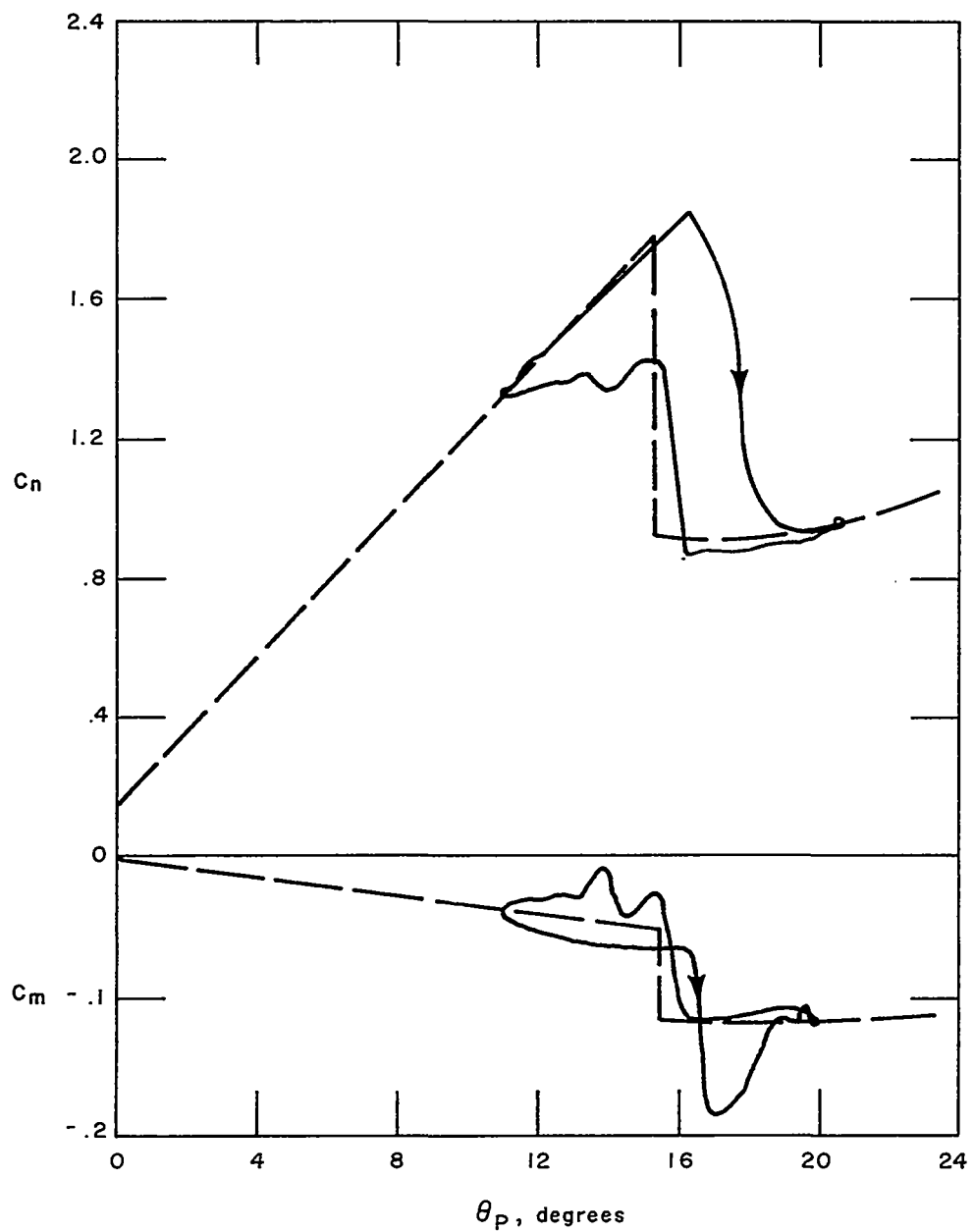


Figure 27 COMPUTED LOADING ON CAMBERED SECTION WITH $k = .3$ AND $\theta_0 = 15.5^\circ$

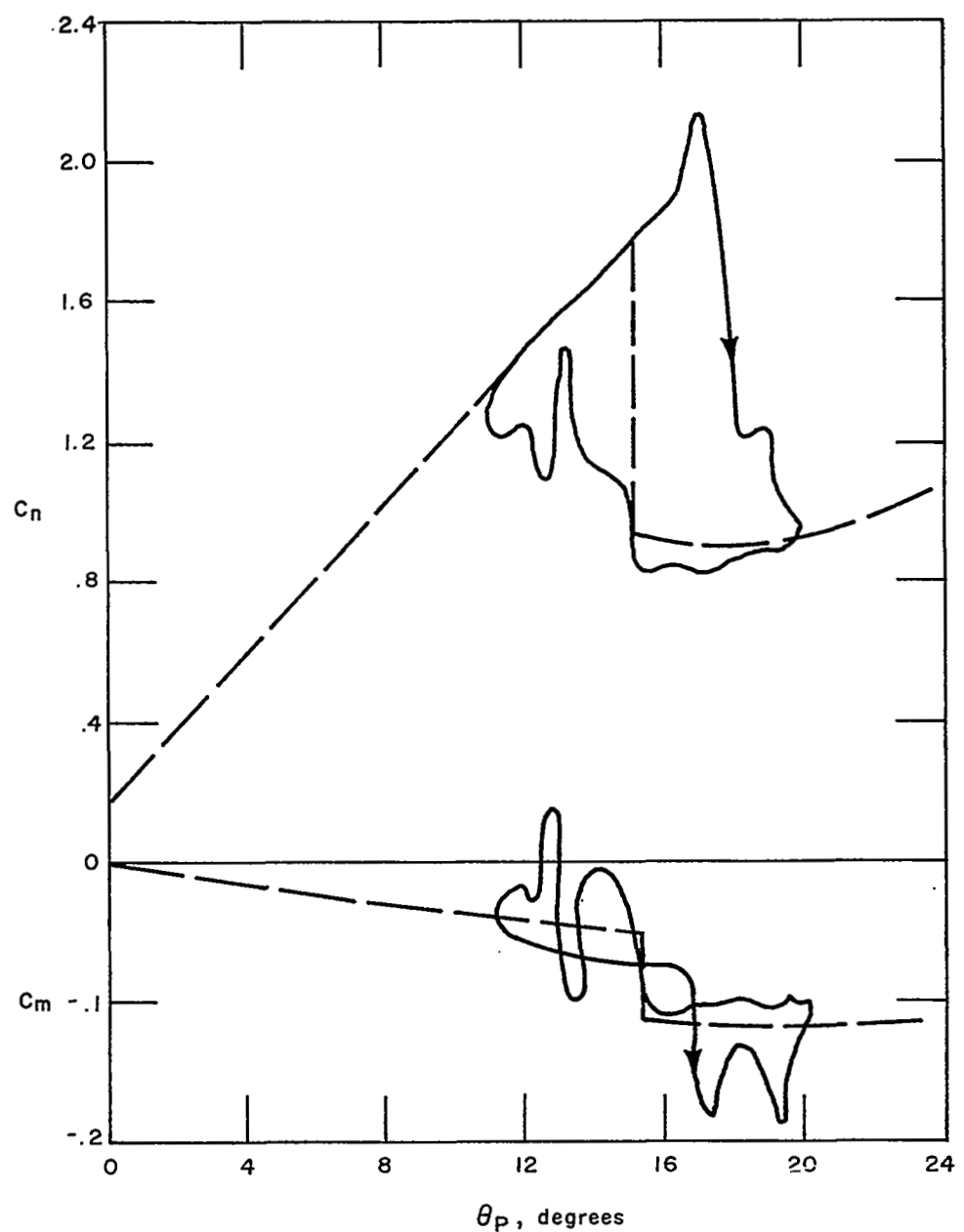


Figure 28 COMPUTED LOADING ON CAMBERED SECTION WITH $k = .26$ AND $\theta_0 = 15.5^\circ$

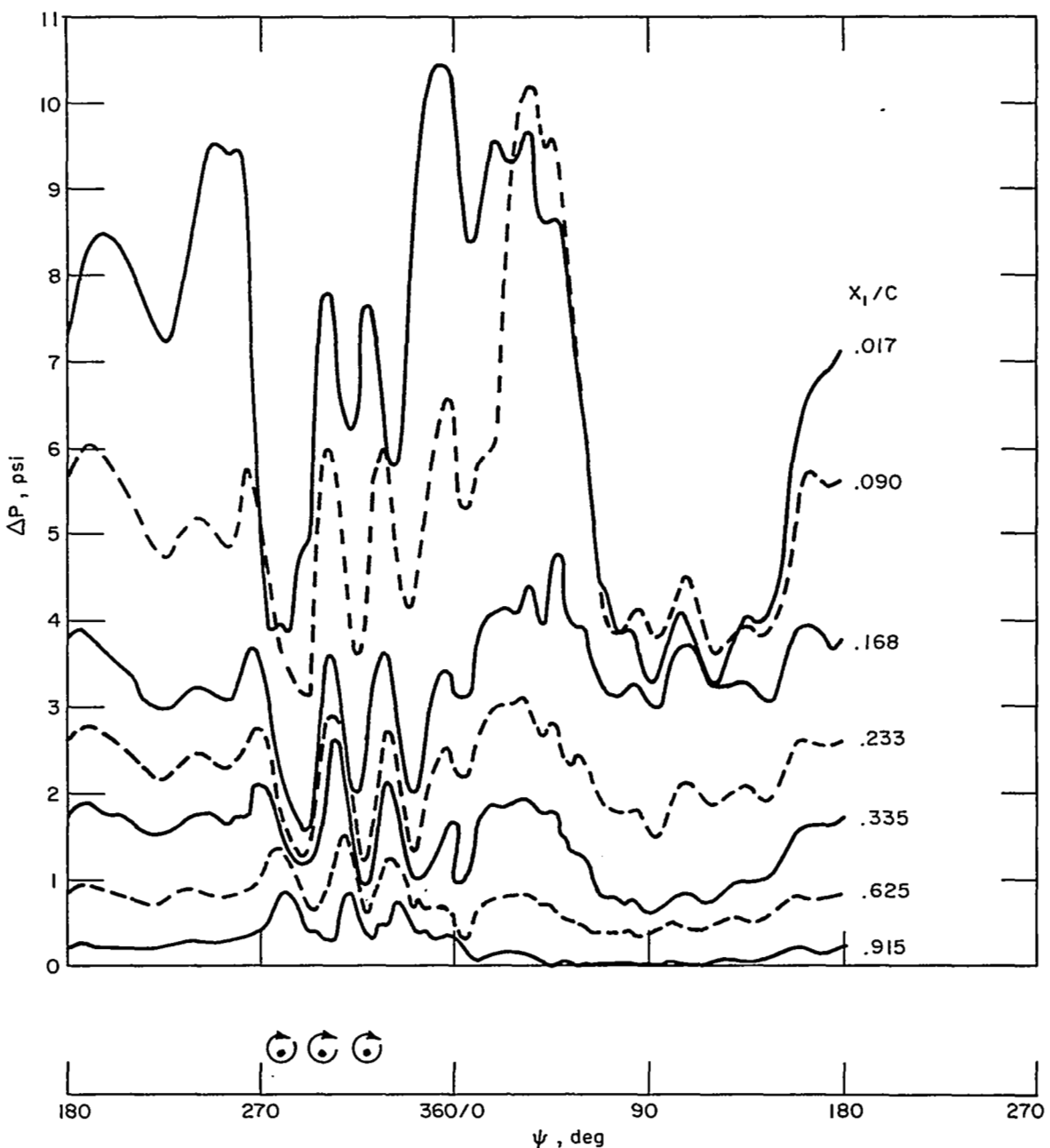


Figure 29 MEASURED DIFFERENTIAL PRESSURE TIME HISTORIES FOR THE 95% BLADE RADIUS IN A 1.5g PULLUP MANEUVER AT AN ADVANCE RATIO OF 0.22
(from Ref. 21)

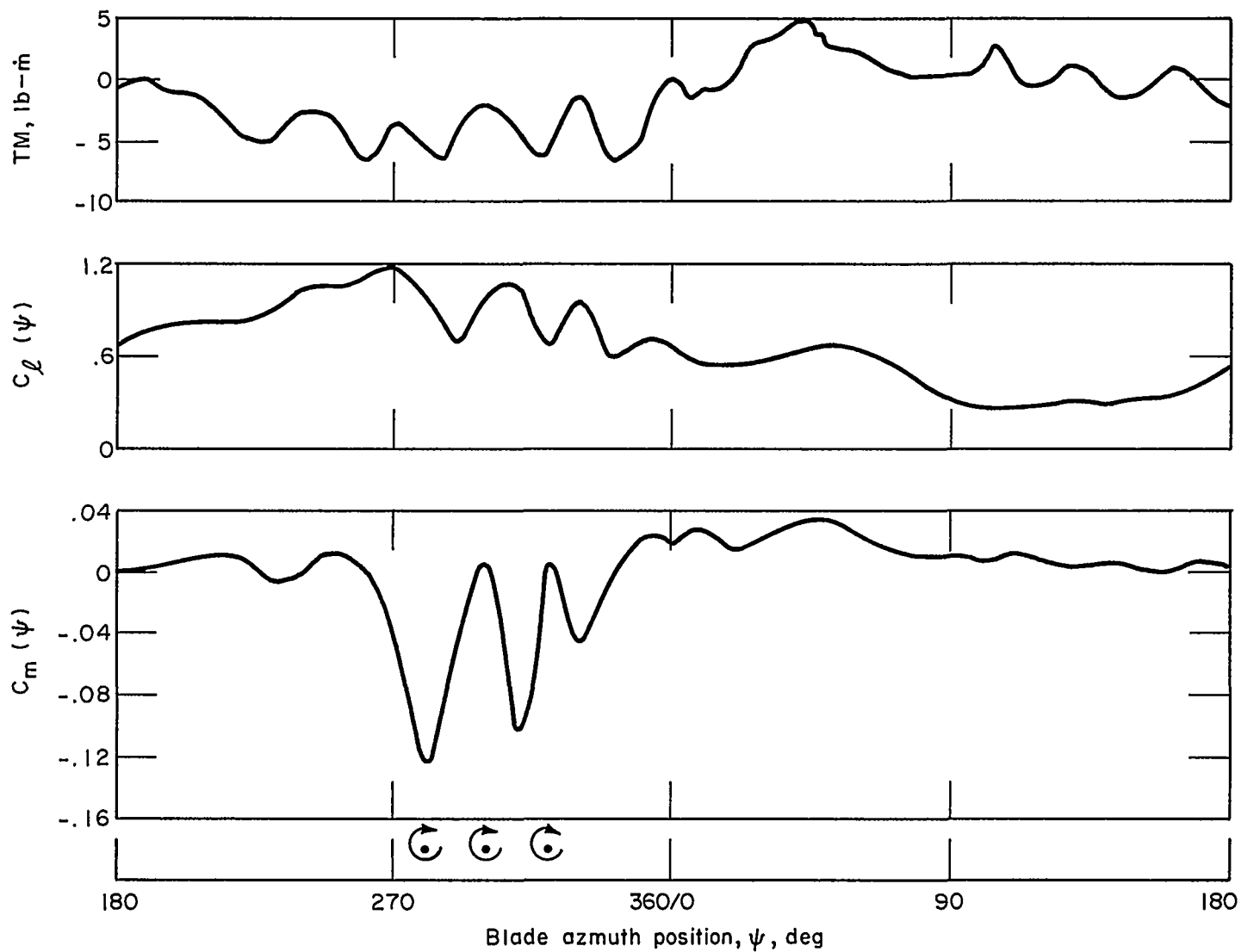


Figure 30 MEASURED TIME HISTORY OF SECTION LOADING AND MOMENT COEFFICIENT AND BLADE TORSIONAL RESPONSE FOR A 1.5g PULLUP (from Ref. 21)

$$\begin{aligned}
\theta_p(t) = & \theta_o + [\theta_p(t-\Delta t) - \theta_o] \cos(\omega_\theta \Delta t) + \frac{\dot{\theta}_p(t-\Delta t)}{\omega_\theta} \sin(\omega_\theta \Delta t) \\
& + \frac{2 m_I}{k_\theta^2} [2C_m(t-\Delta t) - C_m(t-2\Delta t)] [1 - \cos(\omega_\theta \Delta t)] \\
& + \frac{2 m_I}{k_\theta^3 U_o \Delta t} [C_m(t-2\Delta t) - C_m(t-\Delta t)] [\sin(\omega_\theta \Delta t) - \omega_\theta \Delta t \cos(\omega_\theta \Delta t)] \\
\dot{\theta}_p(t) = & \dot{\theta}_p(t-\Delta t) \cos(\omega_\theta \Delta t) - \omega_\theta [\theta_p(t-\Delta t) - \theta_o] \sin(\omega_\theta \Delta t) \\
& + \frac{2 m_I}{k_\theta^2} \left\{ \frac{1}{\Delta t} [C_m(t-\Delta t) - C_m(t-2\Delta t)] [1 - \cos(\omega_\theta \Delta t)] \right. \\
& \left. + \omega_\theta C_m(t-\Delta t) \sin(\omega_\theta \Delta t) \right\}
\end{aligned}$$

where θ_o is the angle of zero restoring moment, and $m_I = \rho b^4/I_\theta$, I_θ being pitch moment of inertia per unit span. A value of .03583 was used for m_I in the calculations. The above formulas were derived by integrating the pitch equation using a linear extrapolation for C_m . Dimensionless vortex strength $\bar{\Gamma} = \Gamma_t/U_b$ was assigned a value of .8636, which corresponds to the strength Γ_t of the tip vortex formed by a heavily loaded blade. The airfoil section of the rotor blades used in the flight test is a 0012 with a trailing-edge extension, so the symmetric section employed in the previous calculations was used for these as well.

A total of nine cases were run, parametrically varying streamwise and vertical spacing of the three vortices to determine whether one or more combinations produce load variations similar to those of Figures 29 and 30. The variations with time of pitch angle (comparable to torsional moment in Figure 30), lift coefficient and moment coefficient for those cases are shown plotted in Figures 31 through 39.

It should first be noted, for purposes of comparison, that the computed oscillations in pitch angle are at approximately the pitch natural frequency (18 semichords traveled per cycle) regardless of the vortex spacing, and the measured oscillations in torsional moment, which correspond directly to blade pitch response, are also at about the pitch natural frequency. It can be seen that, while the three cases with vertical spacing of four semichords (Figures 37, 38, and 39) exhibit considerably less loading variation than the measured results, the computed loading for the three cases with vertical spacing of one semichord (Figures 31, 32, and 33) as well as those with two-semi-chord vertical spacing (Figures 34, 35, and 36) are quite similar to the measured variation of C_l and C_m in the interval of interest. Lift coefficient varies from about .6 to 1.3 and C_m varies from near zero to about -.15 in both computed and measured results. The wave forms are also similar, particularly for the largest streamwise spacing of 16 semichords (Figures 33 and 36). The rapid variations in loading which occur during reattachment are absent from the measured loads, but it is doubtful that the instrumentation employed for the flight test would have detected oscillations of such high frequency (about six times the pitch frequency, or 240 Hz).

The computed differential pressure coefficients at selected chordwise stations for the runs with streamwise spacing of 16 semichords and vertical spacings of one and two semichords are plotted as a function of time in Figures 40 and 41, respectively. Comparing these figures with Figure 29, shows that the variations in computed chordwise loading are also similar to the measured pressure variations. In particular, the computed loading reproduces the phase lag, or time delay, of the loading at the aft chordwise stations with respect to the forward ones.

It can be concluded from the results obtained, then, that the wake-vortex mechanism hypothesized in Ref. 21 is causing the large high-frequency response of the blade. The results further explain why the oscillation is at the pitch natural frequency, rather than at the excitation frequency corresponding to the vortex spacing. The large nose-down moment exerted on the airfoil when it stalls causes the blade to rapidly pitch down and unstall. It was found in the computations that the blade only travels one or two semichords between stall onset and the beginning of flow reattachment. Thus, the blade is effectively excited by a series of discrete impulses, causing it to oscillate at its natural frequency.

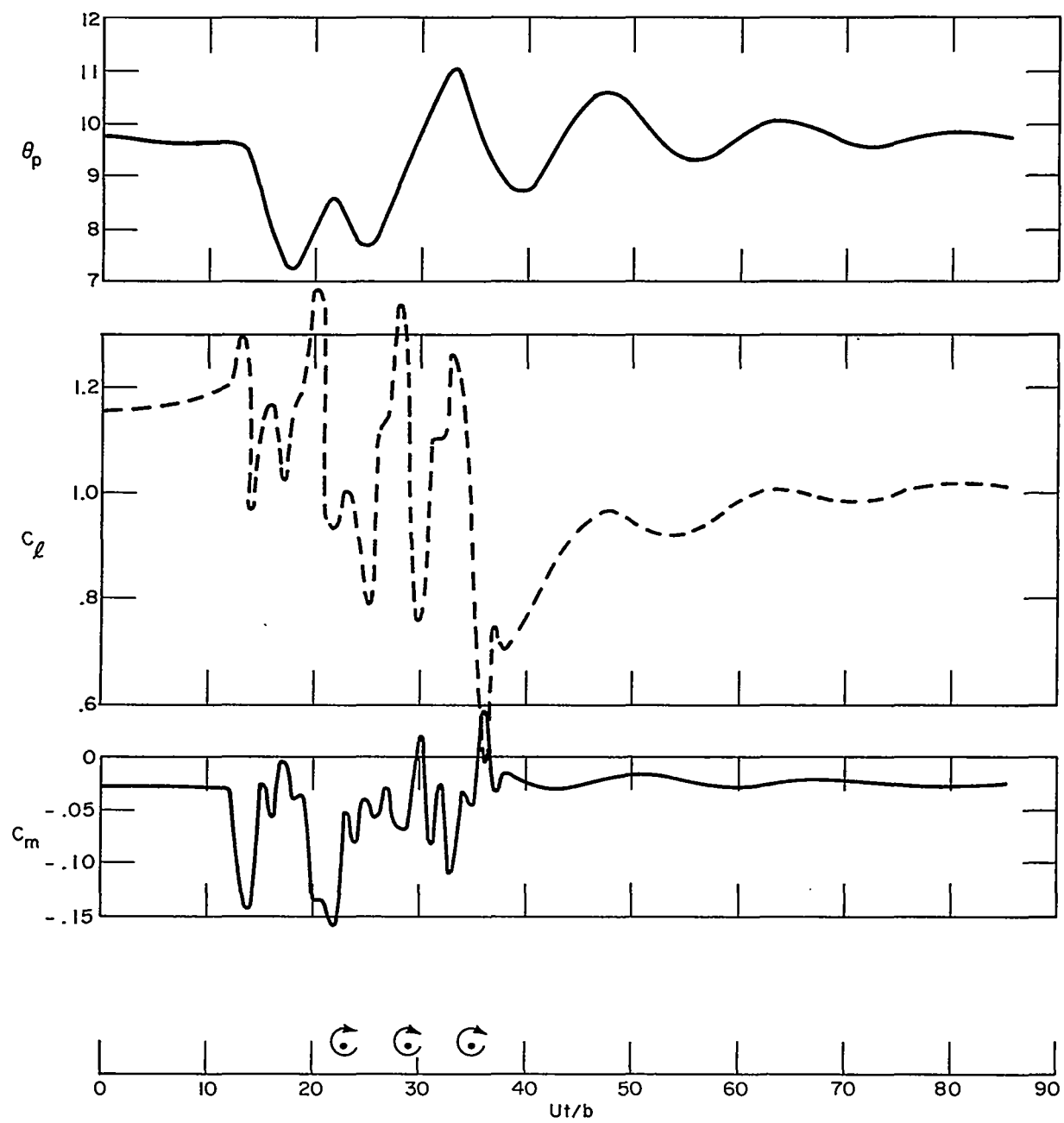


Figure 31 COMPUTED LOADING TIME HISTORY FOR $\bar{H} = 1, \bar{S} = 6$

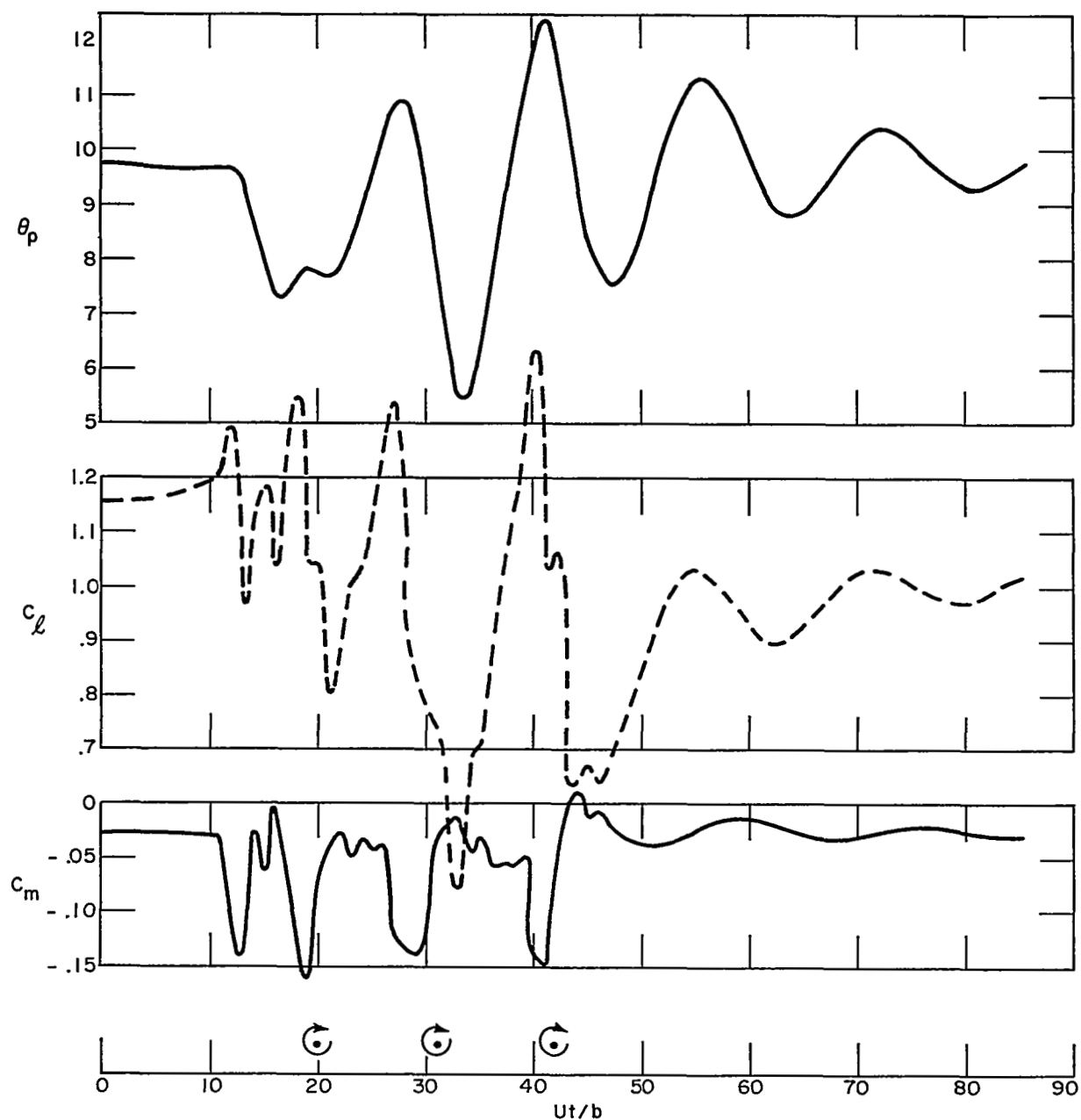


Figure 32 COMPUTED LOADING TIME HISTORY FOR $\bar{H} = 1, \bar{S} = 11$

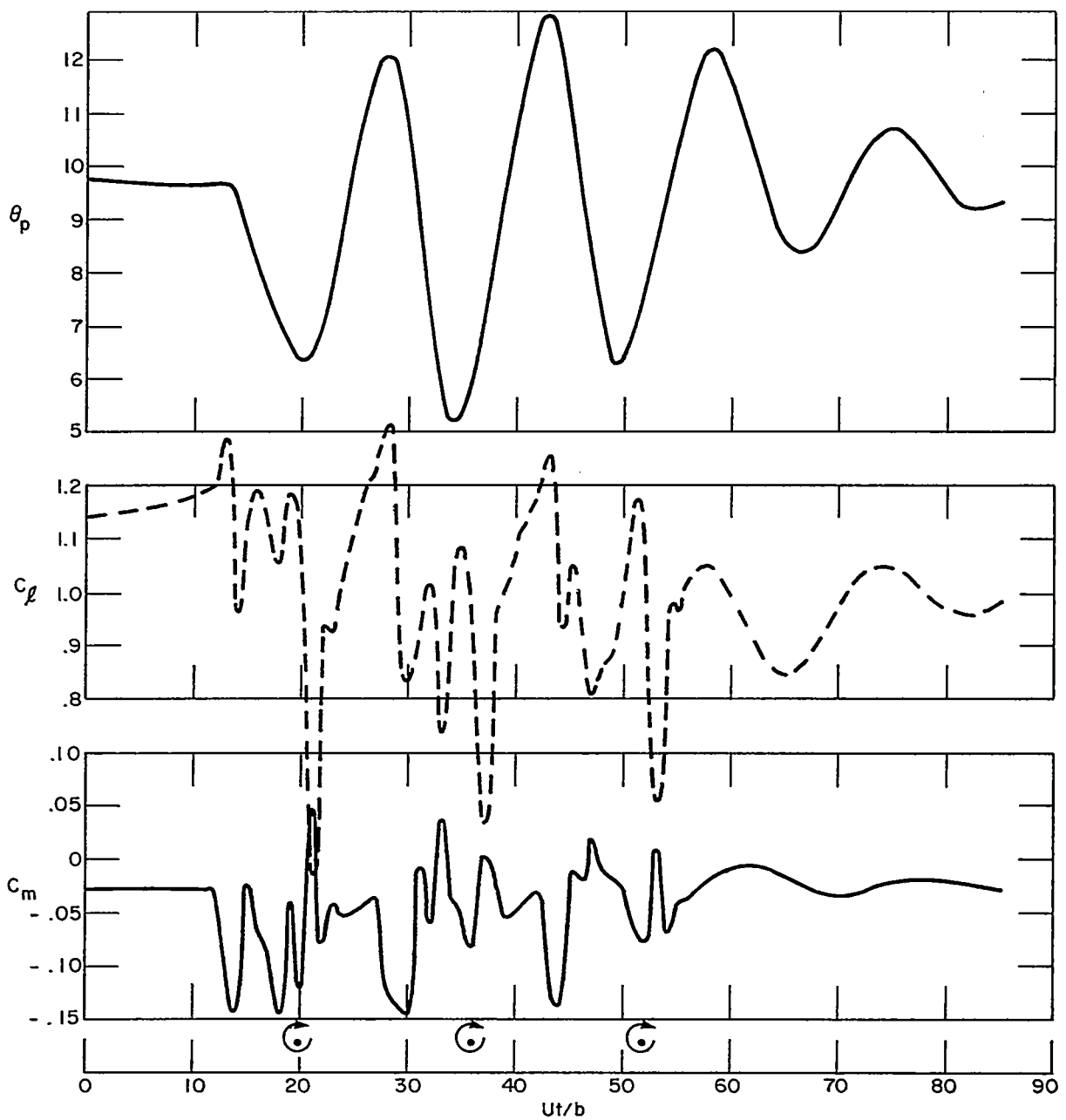


Figure 33 COMPUTED LOADING TIME HISTORY FOR $\bar{H} = 1, \bar{S} = 16$

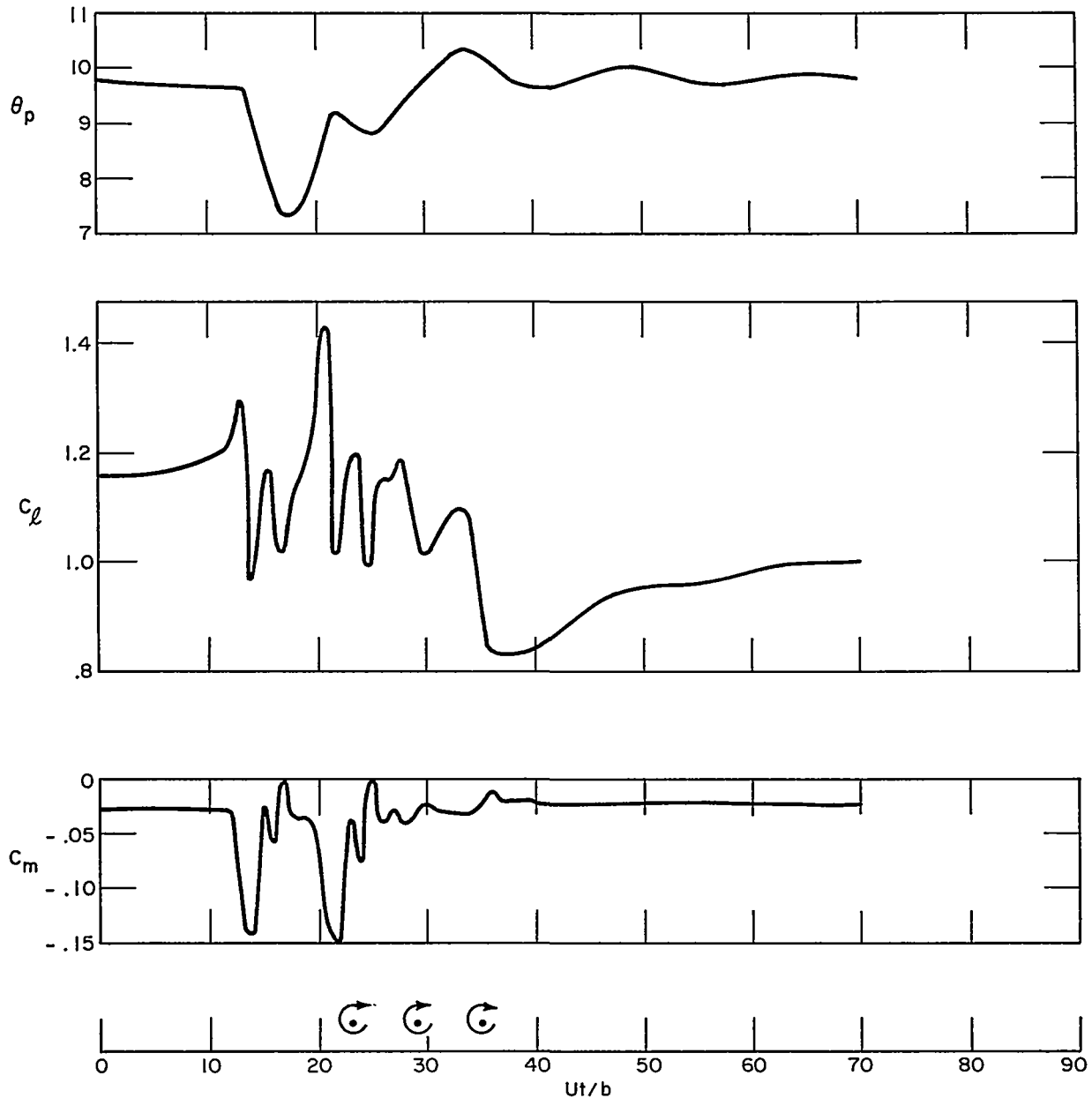


Figure 34 COMPUTED LOADING TIME HISTORY FOR $\bar{H} = 2, \bar{S} = 6$

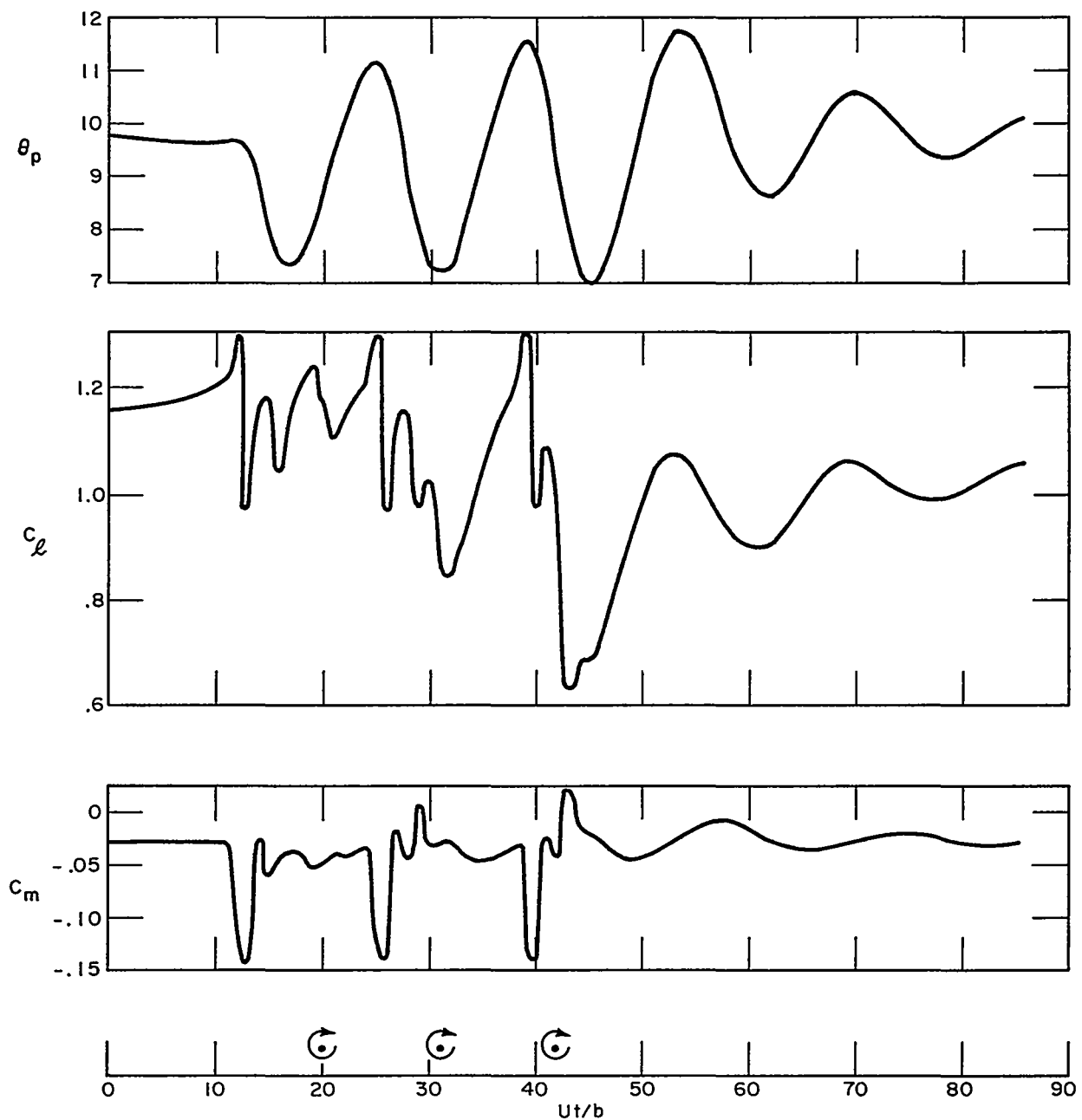


Figure 35 COMPUTED LOADING TIME HISTORY FOR $\bar{H} = 2, \bar{S} = 11$

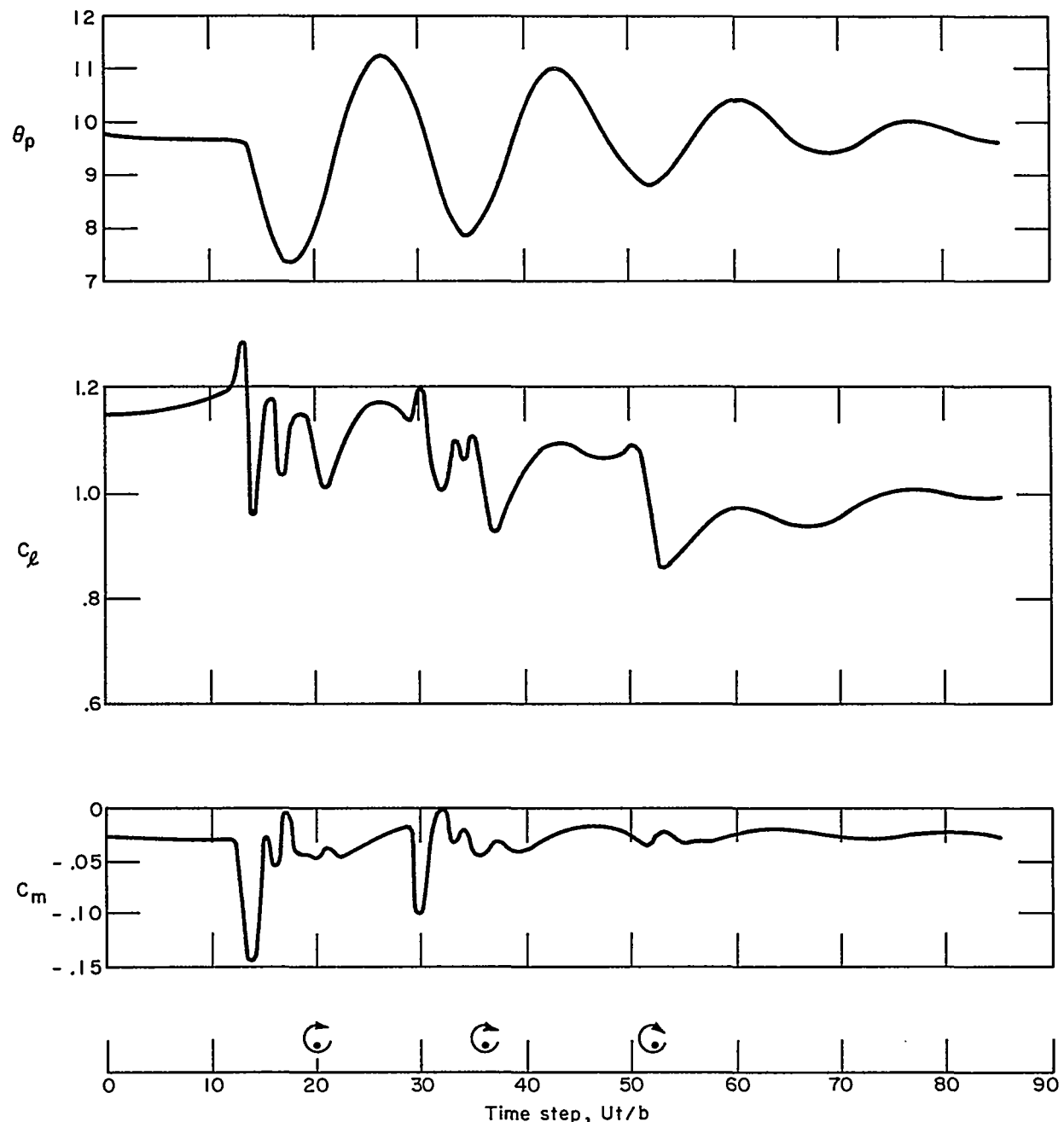


Figure 36 COMPUTED LOADING TIME HISTORY FOR $\bar{H} = 2, \bar{S} = 16$

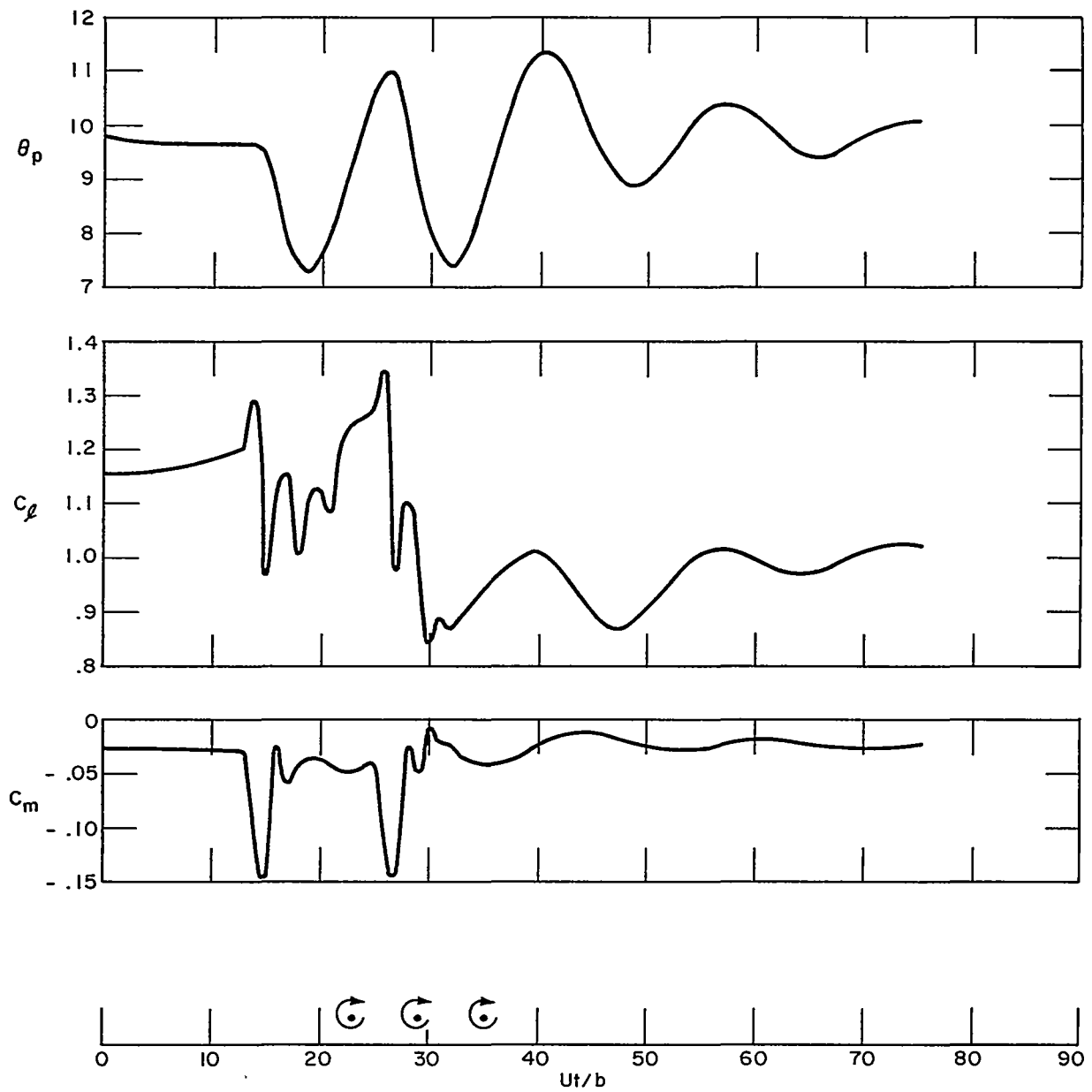


Figure 37 COMPUTED LOADING TIME HISTORY FOR $\bar{H} = 4, \bar{S} = 6$

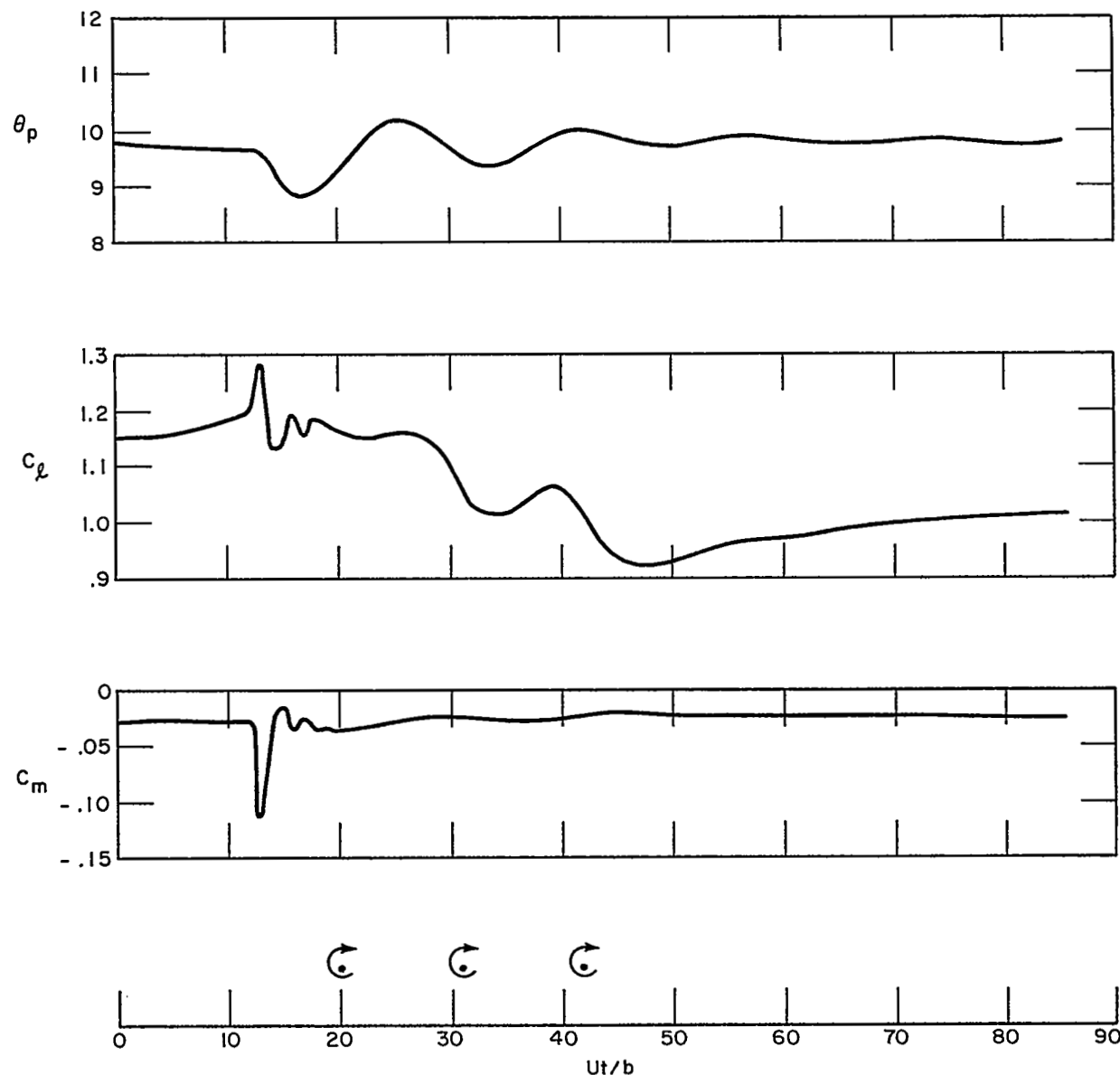


Figure 38 COMPUTED LOADING TIME HISTORY FOR $\bar{H} = 4, \bar{S} = 11$

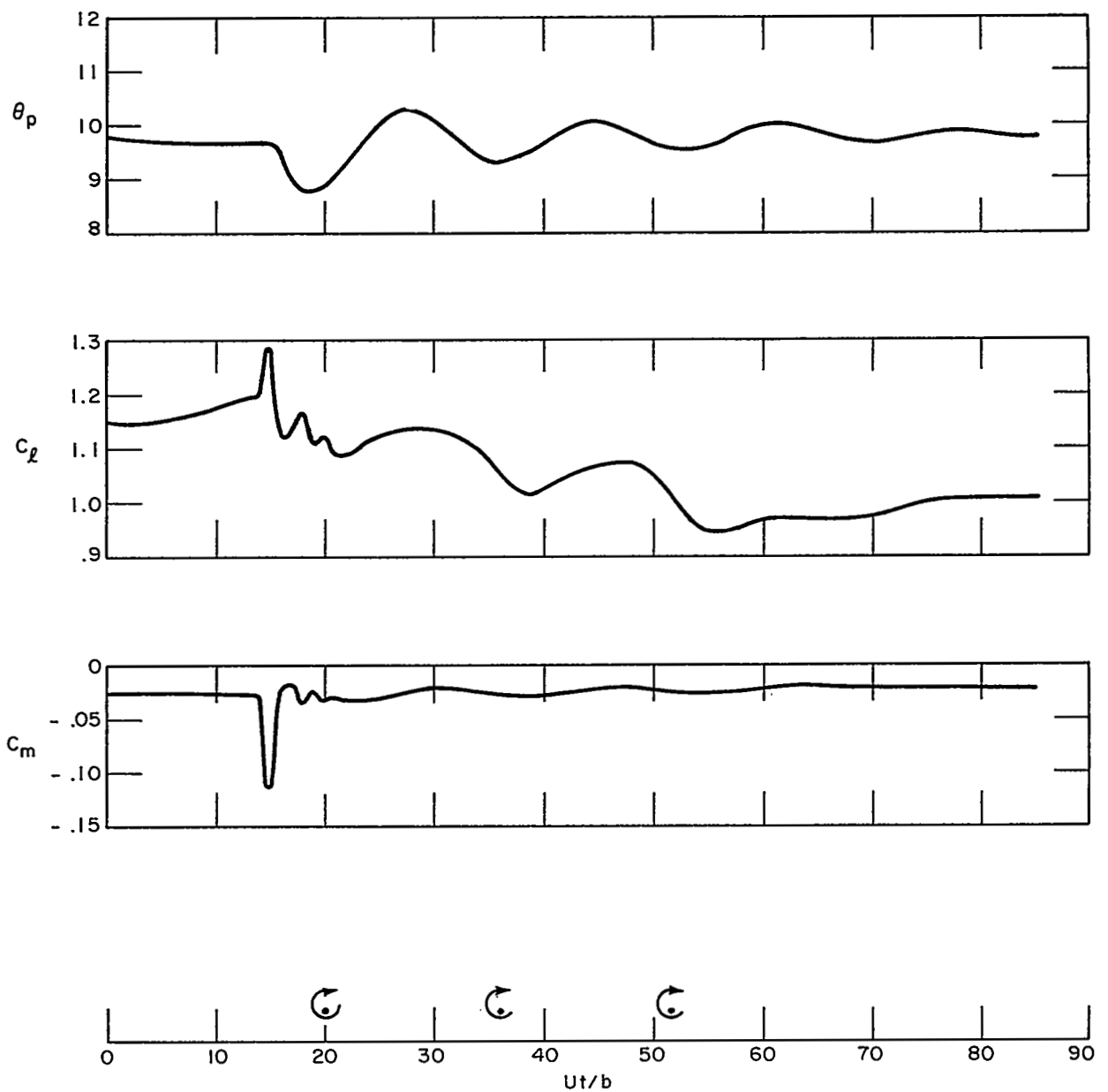


Figure 39 COMPUTED LOADING TIME HISTORY FOR $\bar{H} = 4, S = 16$

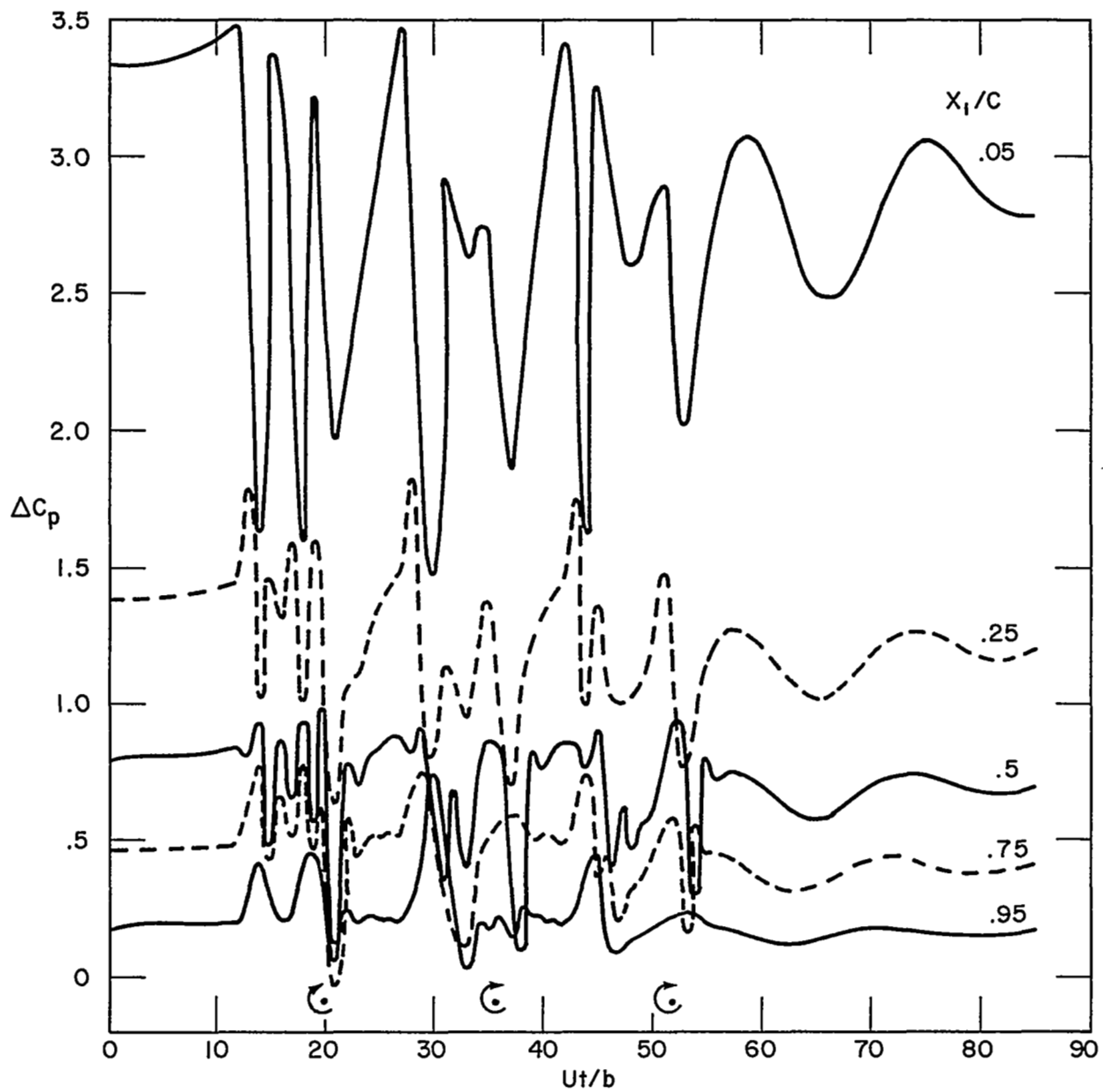


Figure 40 COMPUTED LOADING TIME HISTORY FOR $\bar{H} = 1, \bar{S} = 16$

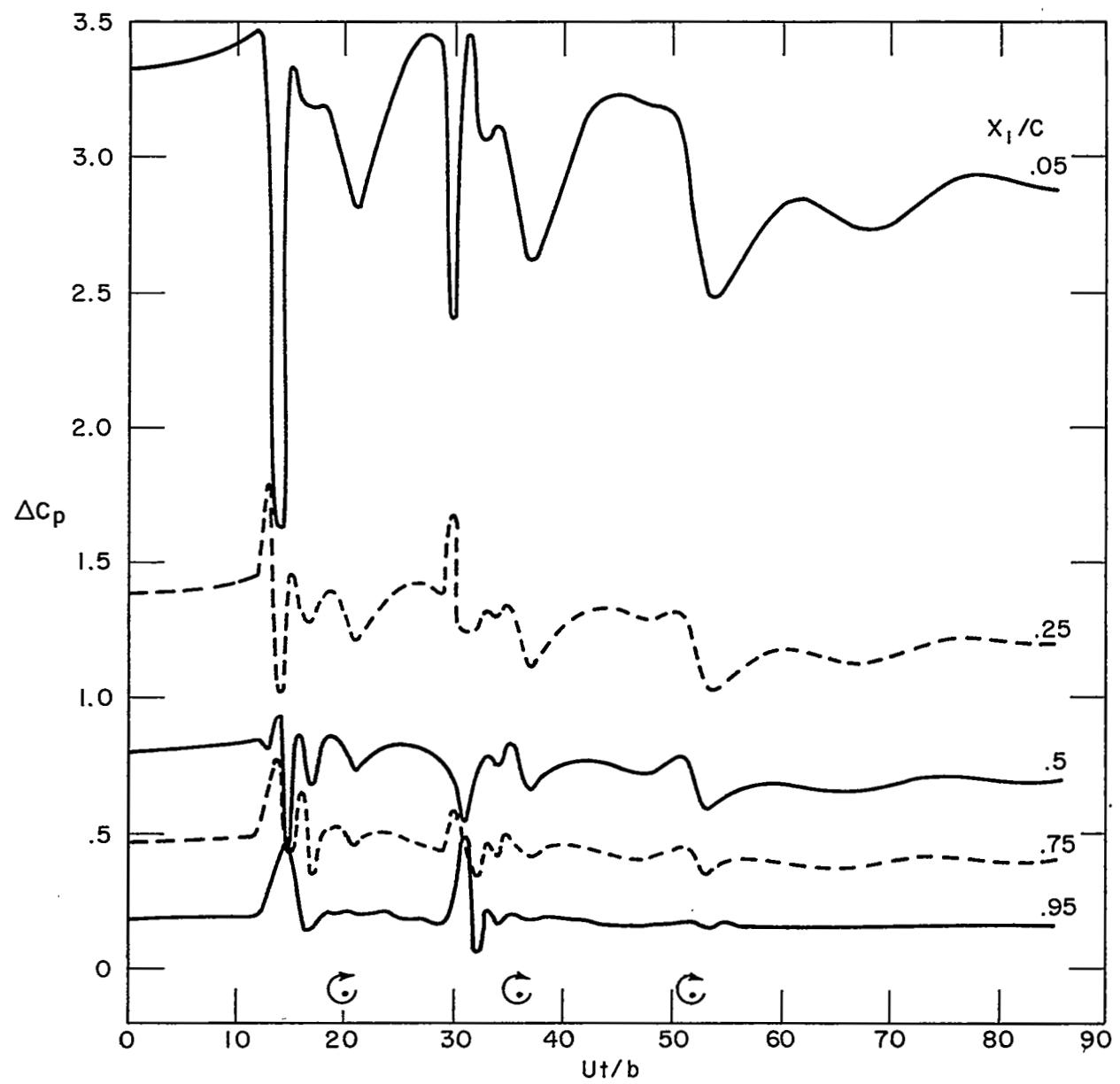


Figure 41 COMPUTED LOADING TIME HISTORY FOR $\bar{H} = 2$, $\bar{S} = 16$

CONCLUSIONS

The method developed is capable of reproducing the essential features of dynamic stall, as demonstrated by the good qualitative agreement obtained between computed and measured loads on a pitching airfoil. The results indicate that dynamic overshoot of the normal force is caused by a redistribution of pressure associated with the pitch rate as well as loading induced on the aft portion of the airfoil by the presence of a dead-air region on the forward portion. Quantitative differences between theory and experiment can be attributed partly to the use of a linearized representation of the potential flow. The assumption that rate of growth of the dead-air region at the onset of leading-edge stall is the free-stream speed and the use of a quasi-steady model for the viscous mixing region also cause quantitative differences between the computed and measured loading.

The large torsional response of helicopter blades during a maneuver which had been detected in flight tests can be attributed to dynamic stall induced by previously formed tip vortices, as hypothesized in Ref. 21. The response is primarily at the torsional natural frequency, rather than at the excitation frequency, because the severe nose-down moments in stall cause the blade to rapidly unstall, effectively loading the blade with a series of impulses.



APPENDIX A

SOLUTION FOR STALLED FLAT PLATE IN STEADY FLOW



APPENDIX A

SOLUTION FOR STALLED FLAT PLATE IN STEADY FLOW

First, consider the case with $x_R > b$. Equations (2) through (5) become, for steady flow with constant pressure p_d in the dead-air region:

$$\frac{1}{\pi} \int_{-b}^b \frac{\gamma(\xi) d\xi}{x - \xi} = 2U\alpha, \quad -b \leq x \leq x_s \quad (A-1)$$

$$\sigma(x) + \frac{1}{\pi} \int_{-b}^b \frac{\gamma(\xi) d\xi}{x - \xi} = 2U\alpha, \quad x_s \leq x \leq b \quad (A-2)$$

$$\gamma(x) + \frac{1}{\pi} \int_{x_s}^{x_R} \frac{\sigma(\xi) d\xi}{x - \xi} = \frac{2(p_\infty - p_d)}{\rho U} \quad x_s \leq x \leq b \quad (A-3)$$

$$\frac{1}{\pi} \int_{x_s}^{x_R} \frac{\sigma(\xi) d\xi}{x - \xi} = \frac{2(p_\infty - p_d)}{\rho U} \quad b \leq x \leq x_R \quad (A-4)$$

The first step is to reduce the number of equations by solving for γ on the interval $(-b, x_s)$ in Eq. (A-1) and solving for σ on the interval (b, x_R) from Eq. (A-4). Formally inverting those two singular integral equations (see Ref. 22), it is found that

$$\gamma(x) = \frac{1}{\pi \sqrt{(x_s - x)(x + b)}} \left\{ \int_{-b}^{x_s} \frac{\left[2U\alpha - \frac{1}{\pi} \int_{x_s}^b \frac{\gamma(\eta) d\eta}{\xi - \eta} \right] \sqrt{(x_s - \xi)(\xi + b)}}{\xi - x} d\xi + A \right\}$$

$$= \frac{1}{\pi \sqrt{(x_s - x)(x + b)}} \left\{ A' - 2\pi U\alpha x - \int_{x_s}^b \frac{\sqrt{(\eta + b)(\eta - x_s)}}{\eta - x} \gamma(\eta) d\eta \right\} \quad (A-5)$$

$$\sigma(x) = \frac{1}{\pi \sqrt{(x_R - x)(x - b)}} \left\{ \int_b^{x_R} \left[\frac{2(p_\infty - p_d)}{\rho U} - \frac{1}{\pi} \int_{x_s}^b \frac{\sigma(\eta) d\eta}{\xi - \eta} \right] \frac{\sqrt{(x_R - \xi)(\xi - b)}}{\xi - x} d\xi + B \right\}$$

$$= \frac{1}{\pi \sqrt{(x_R - x)(x - b)}} \left\{ B' - \frac{2\pi(p_\infty - p_d)x}{\rho U} - \int_{x_s}^b \frac{\sqrt{(x_R - \eta)(b - \eta)} \sigma(\eta) d\eta}{x - \eta} \right\} \quad (A-6)$$

where A' and B' are as yet undetermined constants. If Eqs. (A-5) and (A-6) are substituted in Eqs. (A-2) and (A-3), respectively, and certain of the resulting integrals are evaluated, the following pair of integral equations is obtained:

$$\sigma(x) + \frac{1}{\pi} \int_{x_s}^b \left[\frac{(\eta + b)(\eta - x_s)}{(x + b)(x - x_s)} \right]^{1/2} \frac{\gamma(\eta) d\eta}{x - \eta} = \frac{2U\alpha x - A'/\pi}{\sqrt{(x - x_s)(x + b)}} \quad (A-7)$$

$$\gamma(x) + \frac{1}{\pi} \int_{x_s}^b \left[\frac{(b - \eta)(x_R - \eta)}{(b - x)(x_R - x)} \right]^{1/2} \frac{\sigma(\eta) d\eta}{x - \eta} = \frac{B'/\pi - \left(\frac{2(p_\infty - p_d)}{\rho U} \right) x}{\sqrt{(x_R - x)(b - x)}} \quad (A-8)$$

It is required that σ be well behaved at $x = x_s$, which, from Eq. (A-7), allows the value of A' to be assigned:

$$\frac{A'}{\pi} = 2U\alpha x_s + \frac{1}{\pi} \int_{x_s}^b \sqrt{\frac{\eta+b}{\eta-x_s}} \gamma(\eta) d\eta$$

Equations (A-7) and (A-8) can be combined by formally solving Eq. (A-8) for σ :

$$\begin{aligned} \sqrt{(b-x)(x_R-x)} \sigma(x) &= \frac{1}{\pi \sqrt{(b-x)(x-x_s)}} \left\{ \int_{x_s}^b \left[\frac{B'}{\pi} - \frac{2(p_\infty - p_d)}{\rho U} \xi \right. \right. \\ &\quad \left. \left. - \gamma(\xi) \sqrt{(x_R-\xi)(b-\xi)} \right] \frac{\sqrt{(b-\xi)(\xi-x_s)}}{\xi-x} d\xi + C \right\} \\ &= \frac{1}{\pi \sqrt{(b-x)(x-x_s)}} \left\{ C - \int_{x_s}^b \gamma(\xi) (b-\xi) \frac{\sqrt{(\xi-x_s)(x_R-\xi)}}{\xi-x} d\xi \right. \\ &\quad \left. + \pi \left[\frac{B'}{\pi} - \frac{2(p_\infty - p_d)}{\rho U} \right] x \left[\left(\frac{b+x_s}{2} \right) - x \right] - \frac{2\pi(p_\infty - p_d)}{\rho U} \frac{(b-x_s)^2}{8} \right\} \end{aligned}$$

If σ is to be at least integrable at $x=b$, the quantity in brackets must vanish as $x \rightarrow b$. This provides a relation between the undetermined constants C and B' . The continuity of σ at $x=x_s$ provides the other relation needed to solve for those constants, with the result that

$$\sigma(x) = \sqrt{\frac{x-x_s}{x_R-x}} \left\{ \frac{1}{\pi} \int_{x_s}^b \frac{\gamma(\xi)}{(x-\xi)} \sqrt{\frac{x_R-\xi}{\xi-x_s}} d\xi - \frac{2(p_\infty - p_d)}{\rho U} \right\} \quad (A-9)$$

Substituting Eq. (A-9) and the relation for A' in Eq. (A-7), it is found that

$$\frac{1}{\pi} \int_{x_s}^b \frac{\gamma(\xi)}{x-\xi} \sqrt{\frac{x_R-\xi}{\xi-x_s}} \left\{ \sqrt{\frac{x+b}{x_R-x}} + \sqrt{\frac{\xi+b}{x_R-\xi}} \right\} d\xi = 2U\alpha + \frac{2(p_\infty - p_d)}{\rho U} \sqrt{\frac{x+b}{x_R-x}} \quad (A-10)$$

Now, let

$$g(x) = (x_R - x) \sqrt{\frac{x+b}{x-x_s}} \quad \gamma(x)$$

$$z(x) = \sqrt{\frac{x+b}{x_R - x}}$$

With some manipulation of the integrand of Eq. (A-10), that relation can be written in the form

$$\frac{1}{\pi} \int_{x_s}^b \frac{g(\xi) [dz(\xi)/d\xi]}{z(x) - z(\xi)} d\xi = \frac{x_R + b}{1 + z^2(x)} \left[U\alpha + \frac{1}{\pi} \frac{(p_\infty - p_d)}{\rho U} z(x) \right] \quad (A-11)$$

This equation can be solved for g . Letting $z_s = z(x_s)$ and $z_b = z(b)$, Eq. (A-11) gives

$$g(z) = \frac{1}{\pi} \sqrt{\frac{z_b - z}{z - z_s}} \int_{z_s}^{z_b} \sqrt{\frac{\xi - z_s}{z_b - \xi}} \left(\frac{x_R + b}{\xi^2 + 1} \right) [k_a + k_p \xi] \frac{d\xi}{\xi - z} \quad (A-12)$$

where the undetermined constant was assigned to make g well behaved at z_b and $k_a = U\alpha$, $k_p = (p_\infty - p_d)/\rho U$. If the integrand of Eq. (A-12) is expanded in partial fractions, the resulting integrals can be evaluated by standard methods. By substituting the result in previous relations, expressions for γ and σ over the whole interval for which they are defined can be obtained. The complete solution for $x_R > b$ is:

$$\gamma(x) = \frac{1}{z} \sqrt{\frac{z_s^2 - z^2}{1 + z_s^2}} \left[(C_0 + C_1 z) \sqrt{\frac{z_b - z}{z_s - z}} + (C_0 - C_1 z) \sqrt{\frac{z_b + z}{z_s + z}} \right],$$

$$-b < x \leq x_s;$$

$$\gamma(x) = \frac{1}{z} \sqrt{\frac{(z_b - z)(z + z_s)}{1 + z_s^2}} (C_0 + C_1 z), \quad x_s \leq x \leq b;$$

$$\sigma(x) = \frac{1}{z} (C_0 - C_1 z) \sqrt{\frac{(z - z_s)(z + z_b)}{1 + z_s^2}}, \quad x_s \leq x \leq b;$$

$$\sigma(x) = \frac{1}{z} \sqrt{\frac{z^2 - z_s^2}{1 + z_s^2}} \left[(C_0 - C_1 z) \sqrt{\frac{z + z_b}{z + z_s}} - (C_0 + C_1 z) \sqrt{\frac{z - z_b}{z - z_s}} \right],$$

$b \leq x < x_R.$

where

$$C_0 = (k_a - k_p z_s) \mathfrak{J}_0 + (k_p + k_a z_s) \mathfrak{J}_1$$

$$C_1 = (k_a z_s + k_p) \mathfrak{J}_0 - (k_a - k_p z_s) \mathfrak{J}_1$$

$$\mathfrak{J}_n = \left\{ \frac{\sqrt{(1 - z_s z_b)^2 + (z_s + z_b)^2} + (-1)^n (1 - z_s z_b)}{2(1 + z_s^2)(1 + z_b^2)} \right\}^{1/2}, \quad n = 0, 1.$$

The solution for $x_R < b$ is obtained by an analogous procedure, there again being four coupled singular integral equations in σ and γ . An equation for γ on the interval (x_s, x_R) is obtained which is of exactly the same form as Eq. (A-12). Omitting the details, the solution for $x_R < b$ is:

$$\gamma(x) = \left[\left(\frac{r_R^2 + 1}{r_s^2 + 1} \right) \left(\frac{r_s^2 - r^2}{r_R^2 - r^2} \right) \right]^{1/2} \left\{ \left(\frac{\hat{C}_0}{r} + \hat{C}_1 \right) \sqrt{\frac{r_R - r}{r_s - r}} + \left(\frac{\hat{C}_0}{r} - \hat{C}_1 \right) \sqrt{\frac{r_R + r}{r_s + r}} \right\},$$

$-b < x \leq x_s;$

$$\gamma(x) = \left[\left(\frac{r_R^2 + 1}{r_s^2 + 1} \right) \left(\frac{r + r_s}{r + r_R} \right) \right]^{1/2} \left(\frac{\hat{C}_0}{r} + \hat{C}_1 \right), \quad x_s \leq x \leq x_R;$$

$$\gamma(x) = \left[\left(\frac{r_R^2 + 1}{r_s^2 + 1} \right) \left(\frac{r^2 - r_s^2}{r^2 - r_R^2} \right) \right]^{1/2} \left\{ \left(\frac{\hat{C}_o}{r} + \hat{C}_1 \right) \sqrt{\frac{r - r_R}{r - r_s}} + \left(\frac{\hat{C}_o}{r} - \hat{C}_1 \right) \sqrt{\frac{r + r_R}{r + r_s}} \right\},$$

$$x_R < x \leq b;$$

$$\sigma(x) = \left[\left(\frac{r_R^2 + 1}{r_s^2 + 1} \right) \left(\frac{r - r_s}{r_R - r} \right) \right]^{1/2} \left(\frac{\hat{C}_o}{r} - \hat{C}_1 \right) \quad x_s \leq x < x_R$$

where

$$r(x) = \sqrt{\frac{b+x}{b-x}}$$

$$r_R = r(x_R)$$

$$r_s = r(x_s)$$

while \hat{C}_o and \hat{C}_1 have the same definitions as C_o and C_1 , respectively, but with z_s replaced by r_s and z_b replaced by r_R .

APPENDIX B
POTENTIAL FLOW FORMULATIONS



APPENDIX B

POTENTIAL FLOW FORMULATIONS

The coefficients and inhomogeneous terms of Eqs. (8a) and (8b) are given by the following expressions. For simplicity all lengths in this appendix have been made dimensionless using semichord as reference length. It is understood that any complex term is omitted.

$$a_{mo} = 1 + 2 \lambda_m$$

$$a_{m1} = \cos \theta_m + \lambda_m$$

$$a_{mn} = \cos n \theta_m, \quad n = 2, 3, \dots, N_y$$

where

$$\begin{aligned} \lambda_m &= \frac{3}{4\Delta\xi_o} \left\{ \frac{3}{2} - x_{\gamma_m} + \frac{1}{4} \left(1 + x_{\gamma_m} \right) \left(1 - 3x_{\gamma_m} \right) \ln \left(\frac{1 + x_{\gamma_m}}{1 - x_{\gamma_m}} \right) \right. \\ &\quad \left. + \left[1 + \left(\frac{1 - x_{\gamma_m}}{\Delta\xi_1} \right) \right] \ln \left(\frac{1 + \Delta\xi_1 - x_{\gamma_m}}{1 - x_{\gamma_m}} \right) \right\} \end{aligned}$$

$$\Delta\xi_o = U_o \Delta t$$

$$\Delta\xi_j = x_{wj+1} - x_{wj}, \quad j = 1, 2, \dots, N_w - 1$$

$$\cos \theta_m = x_{\gamma_m}$$

$$b_{mo} = \sqrt{\frac{x_{\gamma_m} - x_s}{x_R - x_{\gamma_m}}} + \left(1 - x_R \right)^{-3/2} \sqrt{x_R - x_S} \left[2(1 - x_R) + \left(\sqrt{\frac{1 - x_{\gamma_m}}{x_R - x_{\gamma_m}}} - 1 \right) \times \left(4x_{\gamma_m} - 1 - 3x_R \right) \right]$$

$$\begin{aligned}
b_{mn} &= \frac{x_{\gamma_m} - x_{\sigma_n-1}}{x_{\sigma_n} - x_{\sigma_{n-1}}}, \quad x_{\sigma_{n-1}} \leq x_{\gamma_m} \leq x_{\sigma_n} \\
&= \frac{x_{\sigma_{n+1}} - x_{\gamma_m}}{x_{\sigma_{n+1}} - x_{\sigma_n}}, \quad x_{\sigma_n} \leq x_{\gamma_m} \leq x_{\sigma_{n+1}} \\
&= 0 \quad , \quad x_{\gamma_m} < x_{\sigma_{n-1}} \text{ or } x_{\gamma_m} > x_{\sigma_{n+1}} \\
n &= 2, 3, \dots, N_\sigma.
\end{aligned}$$

$$\begin{aligned}
r_m &= 2w/U_0 + \frac{4}{3} \lambda_m \left\{ 2 \left[A_0(t-\Delta t) + \frac{1}{2} A_1(t-\Delta t) \right] \right. \\
&\quad \left. - \frac{1}{2} \left[A_0(t-2\Delta t) + \frac{1}{2} A_1(t-2\Delta t) \right] \right\} - \frac{\gamma_{w2}}{\pi} \left(\frac{1-x_{\gamma_m}}{\Delta\xi_1} \right) \ell_n \left(\frac{1+\Delta\xi_1-x_{\gamma_m}}{1-x_{\gamma_m}} \right) \\
&\quad + \frac{1}{\pi} \sum_{j=2}^{N_w-1} \left[\gamma_{wj} + \left(\gamma_{wj+1} - \gamma_{wj} \right) \left(\frac{x_{\gamma_m} - x_{wj}}{\Delta\xi_j} \right) \right] \ell_n \left(\frac{x_{wj+1} - x_{\gamma_m}}{x_{wj} - x_m} \right)
\end{aligned}$$

$$\begin{aligned}
\hat{a}_{ko} &= 0, \quad \bar{x}_{\sigma_k} > 1, \\
&= \frac{1 - \cos \theta_k}{\sin \theta_k} + \left(1 + \bar{x}_{\sigma_k} \right) \left(1 - 3 \bar{x}_{\sigma_k} \right) \left(\frac{3\pi}{8\Delta\xi_o} \right) \frac{U_o}{U} \\
&\quad + \frac{U_o}{U} \left(\frac{3}{2\Delta\xi_o} \right) \left[\pi - \theta_k + \sin \theta_k + \frac{3\pi}{8\Delta\xi_o} \left(1 + \bar{x}_{\sigma_k} \right) \left(1 - \bar{x}_{\sigma_k}^2 \right) \right], \quad \bar{x}_{\sigma_k} \leq 1;
\end{aligned}$$

$$\begin{aligned}
\hat{a}_{kl} &= 0, \quad x_k > 1, \\
&= \frac{1}{2} \hat{a}_{ko} + \sin \theta_k - \frac{1}{2} \left(\frac{1 - \cos \theta_k}{\sin \theta_k} \right), \quad x_{\sigma_k} \leq 1;
\end{aligned}$$

$$\hat{a}_{kn} = 0, \quad x_{\sigma_k} > 1$$

$$= \sin n \theta_k + \frac{U_0}{U} \left(\frac{3}{4\Delta\xi_0} \right) \left[\frac{\sin(n+1)\theta_k}{n+1} - \frac{\sin(n-1)\theta_k}{n-1} \right],$$

$$\bar{x}_{\sigma_k} \leq 1,$$

$$n = 2, 3, \dots, N_\gamma.$$

where

$$\cos \theta_k = \bar{x}_{\sigma_k} \quad \text{for } \bar{x}_{\sigma_k} \leq 1.$$

$$\hat{b}_{ko} = -1 + \frac{U_0}{U} \left(\frac{3}{2\Delta\xi_0} \right) I_{Bo} \left(\bar{x}_{\sigma_k} \right)$$

$$\hat{b}_{kn} = f_{Bn} + \frac{U_0}{U} \left(\frac{3}{2\Delta\xi_0} \right) g_{Bn} \left(\bar{x}_{\sigma_k} \right), \quad n = 2, 3, \dots, N_\sigma;$$

where, if $C_I(x) = \sqrt{(x_R + 1)(x_S + 1)} - 1 - x$, then, for $x < x_S$,

$$I_{Bo}(x) = C_I(x) + (x_R - x_S) \ell_n \left[\frac{\sqrt{x_S - x} + \sqrt{x_R - x}}{\sqrt{x_R + 1} + \sqrt{x_S + 1}} - \sqrt{(x_S - x)(x_R - x)} \right],$$

while for $x_S \leq x \leq x_R$,

$$I_{Bo}(x) = C_I(x) + (x_R - x_S) \ell_n \left[\frac{\sqrt{x_R - x_S}}{\sqrt{1+x_R} + \sqrt{1+x_S}} \right]$$

and for $x > x_R$,

$$I_{Bo}(x) = C_I(x) + (x_R - x_S) \ell_n \left[\frac{\sqrt{(x - x_R)} + \sqrt{x - x_S}}{\sqrt{1+x_R} + \sqrt{1+x_S}} \right] + \sqrt{(x - x_S)(x - x_R)}$$

$$f_{B_n}(x) = \frac{1}{\pi} \left\{ \frac{(x - x_{\sigma_{n-1}})}{(x_{\sigma_n} - x_{\sigma_{n-1}})} \ell_n \left| \begin{array}{c} x_{\sigma_{n-1}} - x \\ x_{\sigma_n} - x \end{array} \right| \right. \\ \left. + \frac{(x_{\sigma_{n+1}} - x)}{(x_{\sigma_{n+1}} - x_{\sigma_n})} \ell_n \left| \begin{array}{c} x_{\sigma_{n-1}} - x \\ x_{\sigma_{n+1}} - x \end{array} \right| \right\}$$

$$g_{B_n}(x) = \frac{1}{\pi} \left[I_g(x_{\sigma_{n-1}}, x_{\sigma_n}; x) \right.$$

$$\left. - I_g(x_{\sigma_{n+1}}, x_{\sigma_n}; x) \right]$$

where

$$(b-a) I_g(a, b; x) = \frac{(x-a)^2}{2} \left[\ell_n |x-a| - \frac{1}{2} \right] \\ - \frac{(1+a)^2}{2} \left[\ell_n |1+a| - \frac{1}{2} \right] \\ - \frac{(x-b)^2}{2} \left[\ell_n |x-b| - \frac{1}{2} \right] + \frac{(1+b)^2}{2} \left[\ell_n |1+b| - \frac{1}{2} \right] \\ - (b-a) \left\{ (x-b) \left[\ell_n |x-b| - 1 \right] + (1+b) \left[\ell_n |1+b| - 1 \right] \right\}$$

$$\hat{t}_k = \hat{f}_p(\bar{x}_{\sigma_k}) \\ + \frac{\pi}{4\Delta\xi_o} \frac{U_o}{U} (1 + \bar{x}_{\sigma_k}) \left\{ \left[1 - 3\bar{x}_{\sigma_k} + \frac{3(1-\bar{x}_{\sigma_k}^2)}{2\Delta\xi_o} \right] \right\} 2 \left[A_o(t-\Delta t) + \frac{1}{2} A_1(t-\Delta t) \right] \\ - \frac{1}{2} \left[A_o(t-2\Delta t) + \frac{1}{2} A_1(t-2\Delta t) \right] \left\{ \right. \\ \left. + \frac{U_o}{U\Delta\xi_o} \left[2 I_\gamma(\bar{x}_{\sigma_k}, t-\Delta t) + 2 I_\sigma(\bar{x}_{\sigma_k}, t-\Delta t) \right. \right. \\ \left. \left. - \frac{1}{2} I_\gamma(\bar{x}_{\sigma_k}, t-2\Delta t) - \frac{1}{2} I_\sigma(\bar{x}_{\sigma_k}, t-2\Delta t) \right] \right\} \\ \text{for } \bar{x}_{\sigma_k} < 1.$$

the terms involving A_0 and A_1 and the I_γ 's being dropped for $\bar{x}_{\sigma_k} > 1$, with

$$I_\sigma(x, t) = B_o(t) I_{B_o}(x, t) + \sum_{i=2}^{N_\sigma} g_{B_i}(x, t) B_i(t)$$

$$\begin{aligned} I_\gamma(x, t - \nu \Delta t) &= (\pi - \theta + \sin \theta) \left[A_0(t - \nu \Delta t) + \frac{1}{2} A_1(t - \nu \Delta t) \right] \\ &+ \frac{1}{2} \sum_{n=2}^{N_\gamma} \left[\frac{\sin(n+1)\theta}{n+1} - \frac{\sin(n-1)\theta}{n-1} \right] A_n(t - \nu \Delta t) \\ &+ 2(1-x_R)^{-3/2} \left[(x_R - x_s)(1-x)(x-x_R) \right]^{1/2} B_o(t - \nu \Delta t) \\ &- \frac{1}{4} \gamma_{w1+\nu}(t) (1+x) (1-x^2), \quad \nu = 0, 1, 2; \end{aligned}$$

with $x = \cos \theta$.

For $-1 \leq x \leq 1$, with $x = \cos \theta$,

$$\begin{aligned} \hat{f}_p(x) &= \frac{2(p_\infty - p_d)}{\rho U U_o} - \frac{2U}{U U_o} T_{max} \left[\frac{t_1}{2} + (1 - \cos \theta) \sum_{n=1}^{N_f} t_n \cos n \theta \right] \\ &- \frac{2U T_{max}}{U_o} \sum_{n=1}^{N_f} \left[\frac{n \sin n \theta (1 - \cos \theta)}{\sin \theta} - \cos n \theta \right] t_n \end{aligned}$$

while for $x > 1$,

$$\hat{f}_P(x) = \frac{2(p_\infty - p_d)}{\rho U U_o} - \frac{2\dot{U} T_{max}}{U U_o} \left[\frac{t_1}{2} + (x-1) \sum_{n=1}^{N_f} (x I_{P_n} - I_{P_{n-1}}) t_n \right]$$

$$- \frac{2 U T_{max}}{U_o} \sum_{n=1}^{N_f} \left\{ \left[x(n+1) - n \right] I_{P_n} - I'_{P_{n-1}} t_n \right\}$$

where $I_{P_n} = \frac{(x - \sqrt{x^2 - 1})^n}{\sqrt{x^2 - 1}}$

The flow at the surface and the pressure coefficient are given by the following expressions (again letting $x = \cos \theta$):

$$\frac{q_e(x, 0^\pm, t)}{U_o} = \frac{\pm 1}{\sqrt{1+x+r_o/2}} \left[\frac{U}{U_o} \sqrt{1+x} + f_q(x, 0^\pm, t) \right]$$

where

$$\sqrt{2} f_q(x, 0^\pm, t) = 2 T_{max} \frac{U}{U_o} \cos \theta / 2 \sum_{n=1}^{N_f} \left[\frac{n \sin n \theta}{\sin \theta} (1 - \cos \theta) - \cos n \theta \right] t_n$$

$$\pm A_o(t) \sin \theta / 2 \pm \cos \theta / 2 \left\{ \sum_{n=1}^{N_\gamma} A_n \sin n \theta \right.$$

$$+ \frac{1}{4} (1+x)(3x-1) \gamma_{w1}(t) + (1-x_R) \left[\frac{(x_R-x_s)(1-x)}{x-x_R} \right]^{1/2} (1+3x_R-4x) B_o(t) \left. \right\}$$

$$- \cos \theta / 2 \left(1 - \sqrt{\frac{x_s - x}{1-x_R-x}} \right) B_o(t) + \cos \theta / 2 \sum_{n=2}^{N_\sigma} f_{B_n}(x, t) B_n(t)$$

$$\begin{aligned}
- C_p(x, O_r^\pm, t) = & 2 \left[\pm \frac{q_e(x, O^\pm, t)}{U} - 1 \right] \\
& \pm \frac{U_o^2}{U^2 \Delta \xi_o} \left\{ \frac{3}{2} I_\gamma(x, t) - 2 I_\gamma(x, t - \Delta t) + \frac{1}{2} I_\gamma(x, t - 2 \Delta t) \right\} \\
& + \frac{U_o^2}{U^2 \Delta \xi_o} \left\{ \frac{3}{2} I_\sigma(t) - 2 I_\sigma(t - \Delta t) + \frac{1}{2} I_\sigma(t - 2 \Delta t) \right\} \\
& + \frac{\overset{\circ}{U}}{U^2} \left[t_1 + 2(1 - \cos \theta) \sum_{n=1}^{N_f} t_n \cos n \theta \right]
\end{aligned}$$



APPENDIX C
BOUNDARY LAYER FINITE DIFFERENCE RELATIONS



APPENDIX C

BOUNDARY LAYER FINITE DIFFERENCE RELATIONS

$$\begin{aligned} \left(\frac{\partial q_s}{\partial t} \right)_{m+1, n} &= \left(\frac{b}{2 U_o \Delta t} \right) [3 q_{s_{m+1, n}}(t) - 4 q_{s_{m+1, n}}(t - \Delta t) + q_{s_{m+1, n}}(t - 2 \Delta t)] \\ \left(\frac{\partial q_s}{\partial s} \right)_{m+1, n} &= a_m q_{s_{m+1, n}} - b_m q_{s_{mn}} + c_m q_{s_{m-1, n}} \end{aligned}$$

$$a_m = \frac{1}{(s_{m+1} - s_m)} + \frac{1}{(s_{m+1} - s_{m-1})}$$

$$b_m = \frac{s_{m+1} - s_{m-1}}{(s_{m+1} - s_m)(s_m - s_{m-1})}$$

$$c_m = \frac{s_{m+1} - s_m}{(s_{m+1} - s_{m-1})(s_m - s_{m-1})}$$

$$\left(\frac{\partial q_s}{\partial \eta} \right)_{m+1, n} = d_n q_{s_{m+1, n+1}} + e_n q_{s_{m+1, n}} - f_n q_{s_{m+1, n-1}}$$

$$d_n = \frac{\eta_n - \eta_{n-1}}{(\eta_{n+1} - \eta_{n-1})(\eta_{n+1} - \eta_n)}$$

$$e_n = \frac{1}{(\eta_n - \eta_{n-1})} - \frac{1}{(\eta_{n+1} - \eta_n)}$$

$$f_n = \frac{\eta_{n+1} - \eta_n}{(\eta_n - \eta_{n-1})(\eta_{n+1} - \eta_{n-1})}$$

$$\left(\frac{\partial^2 q_s}{\partial \eta^2} \right)_{m+1, n} = a_n q_{s_{m+1, n+2}} + \beta_n q_{s_{m+1, n+1}} + \gamma_n q_{s_{m+1, n}} + \delta_n q_{s_{m+1, n-1}}$$

$$a_n = 2 \left[\frac{2 \eta_n - \eta_{n+1} - \eta_{n-1}}{(\eta_{n+2} - \eta_{n-1})(\eta_{n+2} - \eta_{n+1})(\eta_{n+2} - \eta_n)} \right]$$

$$\delta_n = 2 \left[\frac{\eta_{n+2} + \eta_{n+1} - 2\eta_n}{(\eta_{n+2} - \eta_{n-1})(\eta_{n+1} - \eta_{n-1})(\eta_n - \eta_{n-1})} \right]$$

$$\beta_n = \frac{1}{(\eta_{n+1} - \eta_n)^3} (\eta_n - \eta_{n-1})^3 \delta_n - (\eta_{n+2} - \eta_n)^3 \alpha_n$$

$$\gamma_n = -(\alpha_n + \beta_n + \delta_n)$$

$$-\left(\frac{\partial \bar{P}}{\partial s} \right)_{m+1} = \left(\frac{b}{2U_o^2 \Delta t} \right) \left[3 q_{e_{m+1}}(t) - 4 q_{e_{m+1}}(t - \Delta t) + q_{e_{m+1}}(t - 2\Delta t) \right]$$

$$+ \frac{q_{e_{m+1}}}{U_o^2} \left[\xi_m q_{e_{m+2}}(t) + \mu_m q_{e_{m+1}}(t) - \nu_m q_{e_m}(t) \right]$$

$$\xi_m = \frac{s_{m+1} - s_m}{(s_{m+2} - s_m)(s_{m+1} - s_m)}$$

$$\mu_m = \frac{1}{(s_{m+1} - s_m)} - \frac{1}{(s_{m+2} - s_{m+1})}$$

$$\nu_m = \frac{s_{m+2} - s_{m+1}}{(s_{m+1} - s_m)(s_{m+2} - s_m)}$$

The gradient at the wall, needed to evaluate the shear, is given by

$$\left(\frac{\partial q_s}{\partial \eta} \right)_{m+1,1} = k_2 q_{s_{m+1},2} - k_3 q_{s_{m+1},3} + k_4 q_{s_{m+1},4}$$

$$k_2 = \frac{\eta_3 \eta_4}{\eta_2(\eta_3 - \eta_2)(\eta_4 - \eta_2)}$$

$$k_3 = \frac{\eta_2 \eta_4}{\eta_3(\eta_4 - \eta_3)(\eta_3 - \eta_2)}$$

$$k_4 = \frac{\eta_2 \eta_3}{\eta_4(\eta_4 - \eta_3)(\eta_4 - \eta_2)}$$

REFERENCES

1. Harris, F. D.; Tarzanin, F. J.; and Fisher, R. K.: Rotor High Speed Performance, Theory vs. Test. *J. Am. Helicopter Soc.*, vol. 15, no. 3, July 1970, pp. 35-44.
2. Ham, N. D.; and Young, M. I.: Torsional Oscillation of Helicopter Blades Due to Stall. *J. Aircraft*, vol. 3, no. 3, May-June 1966, pp. 218-224.
3. Liiva, J.; Davenport, F. J.; Gray, L.; and Walton, I. C.: Two-Dimensional Tests of Airfoils Oscillating Near Stall--Volume I, Summary and Evaluation of Results. *USAAVLABS Technical Report 68-13A*, April 1968.
4. Ham, N. D.: Aerodynamic Loading on a Two-Dimensional Airfoil During Dynamic Stall. *AIAA J.*, vol. 6, no. 10, October 1968, pp. 1927-1934.
5. Liiva, J.; and Davenport, F. J.: Dynamic Stall of Airfoil Sections for High-Speed Rotors. *J. Am. Helicopter Soc.*, vol. 14, no. 2, April 1969, pp. 26-33.
6. Ericsson, L. E.; and Reding, J. F.: Unsteady Airfoil Stall. *NASA CR 66787*, July 1969.
7. McCullough, G. B.; and Gault, D. E.: Examples of Three Representative Types of Airfoil-Section Stall at Low Speed. *NACA TN 2502*, September 1951.
8. Ward, J. W.: The Behavior and Effects of Laminar Separation Bubbles on Aerofoils in Incompressible Flow. *J. Roy. Aero. Soc.*, vol. 67, December 1963, pp. 783-790.
9. Von Karman, T.; and Sears, W. R.: Airfoil Theory for Non-Uniform Motion. *J. Aero. Sci.*, vol. 5, no. 10, August 1938, pp. 379-389.
10. Lighthill, M. J.: A New Approach to Thin Airfoil Theory. *Aeron. Quart.*, vol. 3, November 1951, pp. 193-210.
11. Smith, A. M. O.; and Cebeci, T.: Numerical Solution of the Turbulent-Boundary-Layer Equations. *McDonnell Douglas Rept. No. DAC 33735*, May 1967.
12. Schlichting, H.: Boundary Layer Theory. Fourth ed., McGraw-Hill Book Co., Inc., 1960.
13. Meller, G. L.; and Gibson, D. M.: Equilibrium Turbulent Boundary Layers. *J. Fluid Mech.*, vol. 24, no. 2, 1966, pp. 225-253.
14. van Driest, E. R.; and Blumer, C. B.: Boundary Layer Transition: Free-stream Turbulence and Pressure Gradient Effects. *AIAA J.*, vol. 1, no. 6, June 1963, pp. 1303-1306.

15. Todisco, A.; and Reeves, B. L.: Turbulent Boundary Layer Separation and Reattachment at Supersonic and Hypersonic Speeds. Proceedings of Conference on Viscous Interaction Phenomena in Supersonic and Hypersonic Flow, USAF ARL, Wright-Patterson Air Force Base, Ohio, May 1969.
16. Hunter, L. G.; and Reeves, B. L.: Results of a Strong-Interaction, Wake-Like Model of Supersonic Separated and Reattaching Turbulent Flows. Preprint no. 71-128, AIAA 9th Aerospace Sciences Meeting, January 1971.
17. Reeves, B. L.; and Lees, L.: Theory of Laminar Near Wake of Blunt Bodies in Hypersonic Flow. AIAA J., vol. 3, no. 11, November 1965, pp. 2061-2074.
18. Gault, D. E.: An Experimental Investigation of Separated Laminar Flow. NACA TN 3505, September 1955.
19. Gray, L.; and Liiva, J.: Two-Dimensional Tests of Airfoils Oscillating Near Stall--Volume II, Data Report. USAAVLABS Tech Rept. no. 68-1313, April 1968.
20. Carta, F. O.: A Theoretical Study of the Effect of Unsteady Pressure Gradient Reduction on Dynamic Stall Delay. Accepted for publication in Journal of Aircraft.
21. Ward, J. F.: Helicopter Rotor Differential Pressures and Structural Response Measured in Transient and Steady-State Maneuvers. J. Am. Helicopter Soc., vol. 16, no. 1, January 1971, pp. 16-25.
22. Muskhelishvili, N. I.: Singular Integral Equations. P. Noordhoff N.V. (Groningen), 1953.